

# **Novel Methods of Microwave-assisted and Albumen-mediated Synthesis of Nano-apatites from Eggshell and Egg White for Tissue Engineering**

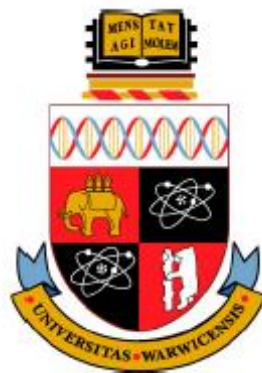
An investigation of novel synthesis methods

**Nathan Robert Parsons**

Student ID: 1004628

Supervisor: Dr Kajal K Mallick

**An ES327 project report submitted in partial fulfilment  
for the degree of  
MEng Mechanical Engineering**



**School of Engineering  
University of Warwick**

**23<sup>rd</sup> April 2013**

# Acknowledgements

Firstly, I would like to thank my supervisor, Dr Kajal Mallick, for his help and guidance throughout the project, as well as his expertise in the fields of biomedical engineering and ceramics processing; without his help, this project could not have achieved the level of success that it did. Thanks are also owed to John Pillier for his assistance with experimental procedures, as well as Claire Caple who conducted some aspects of the preliminary work carried out prior this investigation. I would also like to thank all of the people who helped me to run the various characterisations necessary for this project: James Winnet for his help with conducting SEM and XRD, Dr Ben Douglas for his assistance in running DTA-TGA and Sophie Cox for her help with FTIR. In addition, I would like to thank both Martin Davis and Dr Darren Hughes, who provided advice relating to running XRD and analysing the results.

# Declaration

I declare that, unless otherwise acknowledged in the text, all of the work involved in this report was completed by myself, and it has not previously been submitted for any academic degree. All sources of quoted information are acknowledged in the text using references.

Nathan R Parsons

23 April 2013

# Summary

This report presents an in-depth literature review, along with the results of experiments utilising two separate synthesis methodologies for the production of hydroxyapatite from eggshell-derived precursors. Microwave-assisted synthesis was used, along with a novel albumen-mediated synthesis route developed by the author. The products were characterised using SEM, XRD, DTA-TGA and FTIR.

Microwave-assisted synthesis was shown to produce nanocrystalline hydroxyapatite (HAp) with crystallite sizes less than 20 nm. HAp was synthesised from eggshell-derived  $\text{Ca(OH)}_2$  and  $\text{H}_3\text{PO}_4$ , as well as from  $\text{Ca(OH)}_2$  and  $(\text{NH}_4)_2\text{HPO}_4$ , using pulsed power at 440W in a domestic microwave, ensuring that the reaction temperature did not exceed 60 °C. Crystallite sizes were seen to be stable for temperatures up to 600 °C with an increase to 30 nm when heated to 800 °C. The thermal stabilities of the produced samples were found to be greatly different, with the HAp produced from the  $\text{H}_3\text{PO}_4$  precursor being shown to be stable up to 1169 °C, whilst the HAp produced from  $(\text{NH}_4)_2\text{HPO}_4$  was found to partially decompose to 29%  $\beta$ -TCP and 71% HAp at 600-800 °C.

The synthesis of HAp was shown to be possible from gelled albumen containing evenly dispersed  $\text{Ca(OH)}_2$  by burning it in the presence of  $\text{H}_3\text{PO}_4$ . Mixed morphologies were produced, composed of spheres with diameters less than 2.5  $\mu\text{m}$  and rods with diameters less than 2  $\mu\text{m}$  and lengths less than 6  $\mu\text{m}$ . Thermal stability of the apatite was demonstrated up to 1094 °C, with a biphasic mixture of 88% HAp and 12% Mg-Whitlockite present after sintering at 1200 °C.

HAp nano rods with diameters of 100-300 nm and lengths less than 2  $\mu\text{m}$  were synthesised by the rapid addition of  $\text{Ca(OH)}_2$  and  $\text{H}_3\text{PO}_4$  to freshly extracted egg albumen. A crystallite size of 25 nm was indicated for the as-dried HAp with an increase to 100, 130 and 185 nm corresponding to sintering temperatures of 800, 1000 and 1200 °C, respectively. Thermal stability up to 1000 °C was demonstrated, with a proposed decomposition temperature of 1029 °C; sintering at 1200 °C lead to a conversion to 2.5% Mg-Whitlockite.

Highly amorphous HAp with an estimated crystallite size of 8 nm was synthesised by the rapid addition of  $(\text{NH}_4)_2\text{H}_2\text{PO}_4$  and eggshell-derived  $\text{Ca(CH}_3\text{COO)}_2$  to albumen. The produced HAp was shown to be thermal unstable and decomposed to 90% Mg-Whitlockite and 10% after sintering at 800 °C and further decomposed to 2.5% HAp and 97.5% Mg-Whitlockite upon sintering at 1200 °C. Crystallite size was calculated to be constant at less than 90 nm for sintering temperatures of 800-1200 °C. A near-spherical morphology was produced with typical diameters of 100-250 nm, which were found to have fused into nanoporous structures at a sintering temperature of 800 °C.

# Publication Abstracts

- 1) **Utilisation of biowaste to bioceramic hydroxyapatite for bone tissue engineering.** NR Parsons and KK Mallick (2013), British Conference of Undergraduate Research [15<sup>th</sup>-16<sup>th</sup> April 2013, University of Plymouth]

**Abstract:**

*Avian eggshell is a significant form of biowaste, with millions of tonnes a year generated worldwide. Sometimes eggshell biowaste is used as fertiliser, but a significant amount is wasted. Eggshells contain high calcium carbonate and can be converted into synthetic hydroxyapatite – a key natural mineral in native tissues such as bone. The natural calcium and magnesium content of eggshell is similar to that of the apatite mineral of human bone, and increases the bioactivity of the synthesised hydroxyapatite. Conversion of eggshell biowaste into synthetic hydroxyapatite can be achieved via an inexpensive and energy efficient household microwave irradiation method. This simple technique is quick and processing parameters can be easily controlled to significantly increase the synthesis reaction rate and achieve rapid production. The hydroxyapatite bioceramics produced by this technique can be used for wide ranging orthopaedic tissue engineering applications such as void fillers, bioscaffolds, synthetic biocomposite bone screws and apatite coatings for hip and knee implants.*

- 2) **Rapid synthesis of nanocrystalline hydroxyapatite from biowaste eggshell via microwave irradiation for tissue engineering applications.** NR Parsons and KK Mallick (2013), International Conference of Undergraduate Research [10<sup>th</sup> May 2013, University of Warwick]

**Abstract:**

*Millions of tonnes of eggshell are generated worldwide each year. Some is used as fertiliser but a significant proportion is wasted. Due to the high calcium carbonate content of eggshell, combined with the presence of magnesium, synthetic hydroxyapatite can be produced with properties and composition similar to the natural mineral component of bone. The presence of magnesium increases the bioactivity of the synthesised nanocrystalline hydroxyapatite and is beneficial for in vivo bone remodelling.*

*Microwave irradiation using a typical household microwave oven was utilised to produce nanocrystalline hydroxyapatite from avian eggshell biowaste. Microwave irradiation increases the reaction rate of synthesis and allows rapid production of apatites with optimised processing variables. Pulsed control of irradiation was used to maintain the temperature below 60 °C and the pH was maintained above 12.*

*Nanohydroxyapatite produced by this methodology offers a wide range of tissue engineering applications, including as void fillers, bioscaffolds, synthetic biocomposite bone screws, apatite coatings for orthopaedic implants and bioresorbable drug delivery devices.*

### 3) Rapid synthesis of eggshell derived hydroxyapatite using microwave irradiation. NR

Parsons and KK Mallick (2013), UK Society for Biomaterials Annual Conference

[24<sup>th</sup>-25<sup>th</sup> June 2013, University of Birmingham]

#### **Abstract:**

##### **INTRODUCTION**

Hydroxyapatite is compositionally similar to the mineral component of bone and is bioactive, biocompatible and bioresorbable. Eggshell is predominantly composed of calcium carbonate, with some substitutional ions such as magnesium and iron. Magnesium increases bioactivity and promotes cell adhesion<sup>1</sup>, thus making eggshell a very desirable precursor for the production of calcium phosphates for bone tissue engineering applications.

##### **EXPERIMENTAL METHODS**

Calcium hydroxide was formed by the addition of calcined eggshell-derived calcium oxide to deionised water. Dolapix 64 was added followed by the slow dropwise addition of phosphoric acid. Small quantities of ammonium hydroxide were added to maintain a pH of 12.

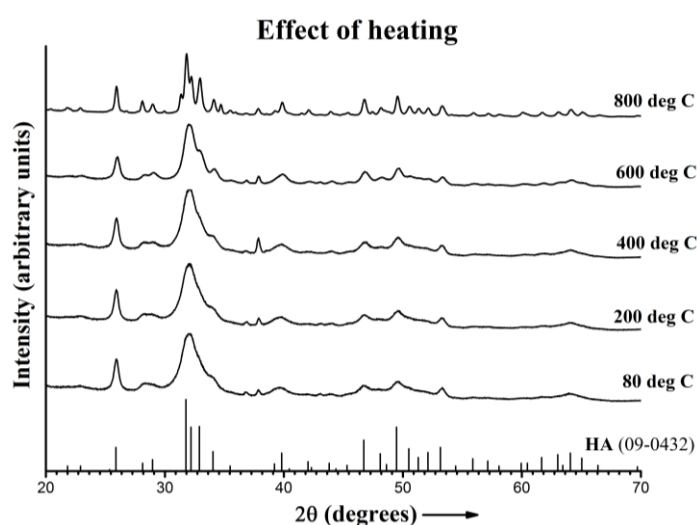
The solution was irradiated in 10 second pulses at a power of 440 W and cooled in an ice bath between each pulse to ensure that the temperature did not exceed 60 °C. This process was repeated for a total irradiation time of 10 minutes. The product was filtered and dried at 80 °C.

Samples were heated sequentially to 200, 400, 600 and 800 °C.

##### **RESULTS AND DISCUSSION**

As can be seen in Figure 1, the XRD data for the synthesised samples match the standard peaks for synthetic hydroxyapatite. Figure 1 also demonstrates the thermal stability of the products at temperatures up to 800 °C.

The broadening of the peaks seen in Figure 1 is indicative of the nanocrystalline nature of the products. Some change in crystallite size was observed for heating at moderate temperatures up to 800 °C. Crystallite sizes were estimated using the Scherrer equation and determined to be 20 nm for the sample dried at 80 °C with no further heating, and 30 nm for the sample heated to 800 °C.



“Figure 1 shows XRD plots for samples heated to various temperatures.”

##### **CONCLUSION**

Nanocrystalline hydroxyapatite was successfully synthesised from avian eggshell biowaste.

##### **REFERENCES**

1. Tucker KL. et al., AJCN (1999),69:727-736

- 4) **Sonochemical synthesis and characterisation of hydroxyapatite nanopowders.** NR Parsons, KK Mallick and MN Keary (2013), Royal Society of Chemistry 11<sup>th</sup> International Conference on Materials Chemistry (MC11) [8<sup>th</sup>-11<sup>th</sup> July 2013, University of Warwick]

**Abstract:**

*During the past few decades much effort has been devoted towards various routes to form nanoscale hydroxyapatite (HAp) powders<sup>1</sup> for biomedical applications due to its excellent osteoconductive and osteoinductive properties<sup>2</sup>. In the present work, ultrasound sonochemistry assisted processing was employed to synthesise nanocrystalline HAp powder from an aqueous mixture of nitrate or hydroxide of calcium and ammonium dihydrogen phosphate precursors. The influence of ultrasonic irradiation on the crystallinity, morphology and specific surface area were investigated by XRD, SEM, TEM, DTA-TG and FTIR. The reaction conditions such as pH and temperature were closely controlled to yield monophasic HAp nanoparticles and the level of ultrasonic irradiation was found to play an important role in the progress of the heterogeneous reaction leading to formation of HAp fine powder.*

**Experimental**

*Aqueous stock solutions of calcium hydroxide or nitrate were prepared for stoichiometric HAp with Ca/P molar ratio of 1.67 and pH was adjusted to a maximum of 12 by slow addition of ammonium phosphate. A commercial ultrasonic homogeniser was used to irradiate the solution at 40-60°C for a period of 5-120 min. The protocol was repeated for identical samples but without irradiation. The centrifuged suspension was dried and subsequently heated to a maximum sintering temperature of 1200°C.*

**Results**

*An equilibrium pH of 10 and a reaction temperature of 60°C were found to be critical in the formation of phase pure HAp as confirmed by XRD. An optimum of 80% irradiation power for 5-10 minutes produced nanopowders of an average crystallite size of 25 nm, determined by the Scherrer equation of line broadening of (002) reflection, accompanied by increasing level of crystallinity with time. The FTIR spectra corresponded well with the characteristic O-P-O vibrational mode  $PO_4^{3-}$ . SEM and TEM studies showed the crystallite sizes of 10 nm diameter and 30 nm in length. The degree of agglomeration varied with the duration of irradiation.*

**Conclusions**

*The phase pure stoichiometric HAp can be synthesised at ambient pressure by sonochemical methodology. The results show that the sonochemistry significantly increased the synthesis efficiency when compared to other conventional precipitation routes. The technique is reliable in terms of monitoring and controlling the progress of the reaction kinetics with respect to pH, temperature and duration of irradiation treatment.*

<sup>1</sup>Nayak, K., *International Journal of ChemTech Research*, 2010, 2(2):p. 903-907

<sup>2</sup>LeGeros, R.Z, *Chemical Reviews*, 2008, 108:p.4742-4753

- 5) **Novel albumen-mediated synthesis of apatites from eggshell-derived precursors.** KK Mallick and NR Parsons (In preparation for Materials Letters)
- 6) **Microwave-assisted formation of nanocrystalline Mg-substituted hydroxyapatite from precursor eggshell.** KK Mallick and NR Parsons (In preparation for Materials Letters)

# UTILISATION OF BIOWASTE TO BIOCERAMIC HYDROXYAPATITE FOR BONE TISSUE ENGINEERING

Nathan R Parsons and Dr Kajal K Mallick  
School of Engineering, University of Warwick, UK

## Introduction

Millions of tonnes of waste eggshell are produced worldwide each year, some of which is used as fertiliser but a significant amount is wasted. Eggshell is composed of around 94% calcium carbonate and 1% magnesium carbonate and can readily be converted into calcium phosphates such as hydroxyapatite. Hydroxyapatite is biocompatible, bioresorbable and is compositionally similar to the calcium-deficient carbonated apatite which forms the mineral component of natural bone. Magnesium acts to increase bioactivity and cell adhesion, so its inclusion in synthesised hydroxyapatite is beneficial, making eggshell a desirable precursor for tissue engineering applications.

Smaller crystal sizes provide a greater surface area for cell attachment and promote more rapid cell growth, making nanocrystalline apatites preferable for use in bone tissue augmentation. Microwave irradiation results in rapid crystal nucleation which in turn leads to the production of smaller crystals in the nano regime, due to the high energy and short pulse times. This potentially allows the cost effective production of nanocrystalline hydroxyapatite.

The aim of this project was to investigate the production of nanocrystalline hydroxyapatite from biowaste eggshell by microwave-assisted synthesis and to assess the suitability of the synthesised hydroxyapatite for application in bone tissue engineering.

## Eggshell Structure

Eggshell consists of four main layers: a porous cuticle, a layer of calcium carbonate, a thick outer membrane, and a thin inner membrane.

The cuticle is a porous layer of organic material on the outer surface of the eggshell and protects against microbial infection.

Figure 1 shows the mineral layer viewed from the edge and the columnar structure of the mineral can be seen. The mineral layer is predominantly calcium carbonate with some magnesium carbonate, iron and other minerals.

The outer eggshell membrane is shown in Figures 2 and 3, and consists of a collagen matrix approximately 50  $\mu\text{m}$  thick. This membrane is highly porous but inhibits the inwards growth of calcite crystals.

The inner eggshell membrane, along with a thinner layer sometimes distinguished as the limiting membrane, contains the albumen and protects the egg from penetration by microorganisms. This layer is around 20  $\mu\text{m}$  thick and is more dense than the outer eggshell membrane, with smaller pore sizes.

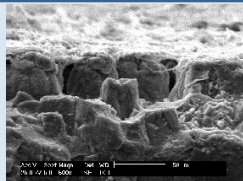


Figure 1: SEM of the edge of an eggshell



Figure 2: SEM of outer eggshell membrane



Figure 3: SEM of outer eggshell membrane

## Materials and Methods

Eggshell was converted to calcium oxide by first removing the membrane, then calcining the mineral at 950  $^{\circ}\text{C}$ . The resultant calcium oxide was added to distilled water to form calcium hydroxide and Dolapix 64 was added as a dispersant. Phosphoric acid was added dropwise whilst the mixture was stirred and the pH was maintained at 12 by addition of small quantities of ammonium hydroxide.

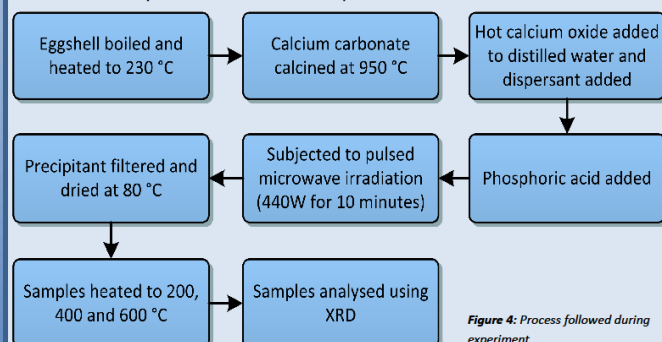


Figure 4: Process followed during experiment

The mixture was irradiated in 10 second pulses for a total of 10 minutes in a 800 W microwave at 55% power. Between each pulse, the mixture was cooled in an ice bath to ensure that the temperature did not exceed 60  $^{\circ}\text{C}$ . The mixture was filtered and dried at 80  $^{\circ}\text{C}$ .

The samples were then heated to 200, 400, 600 and 800  $^{\circ}\text{C}$ .

## Results and Discussion

The XRD results shown in Figure 5 demonstrate the presence of hydroxyapatite and indicate the thermal stability of the samples at temperatures up to 800  $^{\circ}\text{C}$ .

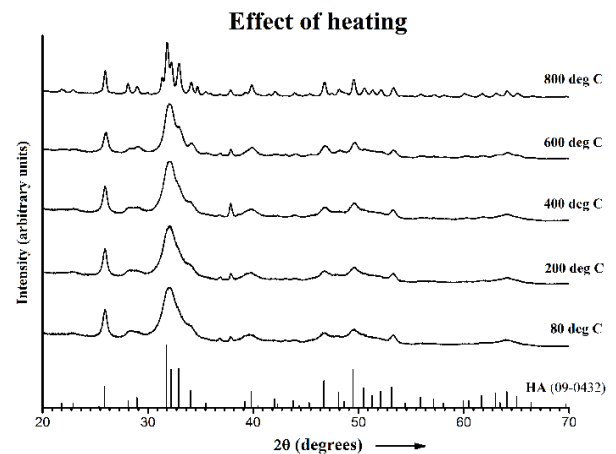


Figure 5: XRD plots showing the effect of temperature on the synthesised hydroxyapatite

Wide peaks in XRD result from small crystal sizes, therefore the peak broadening in Figure 5 demonstrates the nanocrystalline nature of the hydroxyapatite. It can also be seen that very little narrowing of the peaks occurred for temperatures up to 600  $^{\circ}\text{C}$ , suggesting that crystallite sizes did not increase significantly within this temperature range. For the sample heated to 800  $^{\circ}\text{C}$ , the peaks are discernably narrower, indicating increased crystallite sizes.

$$L = \frac{K\lambda}{B \cos \theta} \quad \text{Equation 1: Scherrer equation, where } L = \text{crystallite size, } K = \text{Scherrer constant } (=0.9), \lambda = \text{x-ray wavelength } (=1.54056 \text{ \AA}), B = \text{peak width at half maximum (in radians), and } \theta = \text{Bragg angle}$$

Crystallite sizes can be estimated using the Scherrer equation given in Equation 1. Using this, the crystallite size was estimated to be 17 nm for the as produced hydroxyapatite dried at 80  $^{\circ}\text{C}$ . For the sample heated to 800  $^{\circ}\text{C}$ , the crystallite size was estimated to have increased to 27 nm. This represents a significant increase in crystallite size but is still similar to the crystallite sizes found in natural bone and so remains within the suitable range for tissue engineering applications.

## Conclusions

Eggshell biowaste can be easily converted to nanocrystalline hydroxyapatite by microwave irradiation for use in advanced tissue engineering.

Calcination of eggshell-derived calcium carbonate to calcium oxide and subsequently calcium hydroxide can be used as a precursor for the synthesis of nanohydroxyapatite.

A cheap domestic microwave can be used economically to synthesise such an important constituent for bone tissue augmentation.

# Author's Assessment

## **What is the engineering contribution of this project?**

Biomedical engineering is a field requiring an understanding of both materials science and biological systems, and biological systems present a further set of constraints to the choice of materials. It is therefore important to improve upon the methodologies currently utilised to produce biomaterials, with the synthesis of materials which are compositionally similar to natural materials found in biological systems being one of the main aims. This project builds upon previous research and extends it to develop a promising new methodology.

## **Why should this contribution be considered either relevant or important to engineering?**

A promising new albumen-mediated synthesis methodology has been developed which allows for nanocrystalline Mg-substituted hydroxyapatite to be made at low temperatures. Further development of this method could allow for the synthesis of apatites with highly desirable properties. Controlled properties are essential to biomedical applications in order to ensure that the patient responds in a predictable way, with a good outcome.

## **How can others make use of the work in this project?**

The body of work presented here can be built on by others in order to produce apatites with more desirable properties. The albumen-mediated synthesis route developed during this project presents a large area for further study, as very little is known about the use of albumen in synthesis reactions. Investigation into the effects of different parameters of the synthesis reaction is the likely starting point for further research seeking to build upon the newly developed albumen-mediated synthesis methodology.

## **Why should this project be considered an achievement?**

This project advances the field of apatite synthesis through the investigation of a current methodology and the development of a novel methodology. The novel methodology was shown for the first time to be a suitable route for the synthesis of highly amorphous Mg-substituted apatites, which are very desirable materials for biomedical engineering applications, from hard tissue engineering to drug delivery systems.

## **What are the weaknesses of this project?**

The main weakness of this project is that it lacks a more full exploration of the factors affecting the produced apatites. Some conclusions can be drawn about how synthesis parameters affect the reaction, but many questions remain unanswered and so are highlighted as area for further work. There was simply insufficient time available for enough synthesis experiments to be conducted to draw any solid conclusions about key variables, but this does not reduce the valuable contribution that this project makes to the field of research.

# Abbreviations

<b>ACP</b>	Amorphous calcium phosphate
<b>BCP</b>	Biphasic calcium phosphate
<b>CDHAp</b>	Calcium-deficient hydroxyapatite
<b>CHAp</b>	Carbonated hydroxyapatite
<b>DCPA</b>	Dicalcium phosphate anhydrous
<b>DCPD</b>	Dicalcium phosphate dihydrate
<b>DTA</b>	Differential thermal analysis
<b>DTA-TGA</b>	Combined differential thermal analysis and thermogravimetric analysis
<b>e.m.f.</b>	Electromotive force (potential difference)
<b>ESM</b>	Eggshell membrane
<b>FTIR</b>	Fourier-transform infrared spectrometry
<b>FWHM</b>	Full width at half maximum
<b>HAp</b>	Hydroxyapatite
<b>MCPA</b>	Monocalcium phosphate anhydrous
<b>OCP</b>	Octacalcium phosphate
<b>OxHAp</b>	Oxyapatite
<b>SEM</b>	Scanning electron microscopy
<b><math>\alpha</math>-TCP</b>	$\alpha$ -tricalcium phosphate
<b><math>\beta</math>-TCP</b>	$\beta$ -tricalcium phosphate
<b>TEM</b>	Transmission electron microscopy
<b>TGA</b>	Thermogravimetric analysis
<b>TTCP</b>	Tetracalcium phosphate
<b>wt</b>	Weight
<b>XRD</b>	X-ray diffractometry
<b>YSP</b>	Yolk water-soluble protein

# List of Figures

Figure 1: Structural organisation of a typical bone .....	4
Figure 2: Unit cell of the hydroxyapatite crystal structure .....	7
Figure 3: Structure of an avian egg.....	9
Figure 4: Effect of temperature and pH on the produced morphology of HAp crystals, with experimental data corresponding to two-dimensional and three-dimensional shapes are marked as ▼ and ●, respectively .....	12
Figure 5: Schematic showing the variation of HAp morphology with OH <sup>-</sup> concentration at 180 °C (450 K).....	13
Figure 6: Main types of thermogravimetric curves .....	21
Figure 7: Diagram showing the geometry for the diffraction of X-rays, with the derivation of Bragg's Law .....	23
Figure 8: Schematic diagram of an X-ray diffractometer. T = X-ray source, S = specimen, C = detector, O = axis of rotation for specimen and detector .....	23
Figure 9: Schematic of a Michelson interferometer .....	25
Figure 10: Flowchart of precursor synthesis process .....	27
Figure 11: Flowchart for the synthesis of apatites via a microwave-assisted method .....	29
Figure 12: Flowchart for the synthesis of apatite via albumen-mediated synthesis .....	31
Figure 13: SEM micrograph of the edge of an eggshell, with the outside in the lower portion of the image.....	35
Figure 14: SEM micrograph of the edge of an eggshell fragment.....	36
Figure 15: SEM micrograph of the outer eggshell membrane.....	37
Figure 16: SEM micrograph of the inner eggshell membrane .....	37
Figure 17: DTA-TGA curves for eggshell with the membrane removed .....	38
Figure 18: XRD spectra for MIC1 samples dried at 80 °C and sintered at 200, 400, 600 and 800 °C.....	39
Figure 19: DTA-TGA curves for MIC1 dried at 80 °C .....	41
Figure 20: XRD spectra for MIC2 samples dried at 80 °C and sintered at 200, 400, 600 and 800 °C.....	42
Figure 21: SEM micrograph of ALB1 sintered at 800 °C.....	44
Figure 22: SEM micrograph of ALB1 sintered at 800 °C.....	45
Figure 23: SEM micrograph of ALB1 sintered at 800 °C.....	45
Figure 24: SEM micrograph of ALB1 sintered at 800 °C.....	46
Figure 25: SEM micrograph of ALB1 sintered at 800 °C.....	46
Figure 26: XRD spectra for ALB1 samples sintered at 800, 1000 and 1200 °C .....	47
Figure 27: DTA-TGA curves for a sample of ALB1 taken after heating to 450 °C .....	49
Figure 28: FTIR spectrum for ALB1 sintered at 800 °C .....	50
Figure 29: FTIR spectrum for ALB1 sintered at 800 °C for a limited range of transmittance values.....	50
Figure 30: SEM micrograph of ALB2 sintered at 800 °C.....	52
Figure 31: SEM micrograph of ALB2 sintered at 800 °C.....	53

---

Figure 32: SEM micrograph of ALB2 sintered at 800 °C.....	53
Figure 33: SEM micrograph of ALB2 sintered at 800 °C.....	54
Figure 34: SEM micrograph of ALB2 sintered at 800 °C.....	54
Figure 35: XRD spectra of ALB2 samples dried at 80 °C and sintered at 800, 1000 and 1200 °C.....	55
Figure 36: DTA-TGA curves for a sample of ALB2 dried at 80 °C.....	57
Figure 37: FTIR spectrum for ALB2 sintered at 800 °C .....	58
Figure 38: SEM micrograph of ALB3 sintered at 800 °C.....	59
Figure 39: SEM micrograph of ALB3 sintered at 800 °C.....	60
Figure 40: SEM micrograph of ALB3 sintered at 800 °C.....	60
Figure 41: SEM micrograph of ALB3 sintered at 800 °C.....	61
Figure 42: XRD spectra of ALB3 dried at 80 °C and sintered at 800, 1000 and 1200 °C.....	62
Figure 43: DTA-TGA curves for the filtration residue of ALB3 dried at 80 °C.....	64
Figure 44: DTA-TGA curves for the filtrate of ALB3 dried at 80 °C .....	64
Figure 45: FTIR spectrum for ALB3 sintered at 800 °C .....	66

# List of Tables

Table 1: Composition of bone .....	3
Table 2: Comparative compositions of human enamel, bone and hydroxyapatite (HAp) .....	5
Table 3: Calcium phosphates and their properties .....	6
Table 4: Composition of calcined eggshell.....	10
Table 5: Main types of thermogravimetric curves, corresponding to Figure 6.....	21
Table 6: Phase analysis of MIC1 samples at different temperatures expressed as a percentage .....	40
Table 7: Estimated crystallite sizes for MIC1 dried at 80 °C and sintered at 200, 400, 600 and 800 °C.....	40
Table 8: Phase analysis of MIC2 samples at different temperatures expressed as a percentage .....	43
Table 9: Estimated crystallite sizes for MIC2 dried at 80 °C and sintered at 200, 400, 600 and 800 °C.....	43
Table 10: Phase analysis of ALB1 samples at different temperatures expressed as a percentage .....	47
Table 11: Crystallite sizes for ALB1 estimated using the Scherrer equation.....	48
Table 12: Phase analysis of ALB2 samples at different temperatures expressed as a percentage .....	55
Table 13: Crystallite sizes for ALB2 estimated using the Scherrer equation.....	56
Table 14: Phase analysis of ALB3 samples at different temperatures expressed as a percentage .....	63
Table 15: Crystallite size for ALB3 dried at 80 °C estimated using the Scherrer equation .....	63
Table 16: Crystallite sizes for ALB3 sintered at 800, 1000 and 1200 °C estimated using the Scherrer equation ..	63
Table 17: Project cost.....	75

# Table of Contents

<b>ACKNOWLEDGEMENTS</b> .....	<b>I</b>
<b>DECLARATION</b> .....	<b>II</b>
<b>SUMMARY</b> .....	<b>III</b>
<b>PUBLICATION ABSTRACTS</b> .....	<b>IV</b>
<b>AUTHOR'S ASSESSMENT</b> .....	<b>VIII</b>
<b>ABBREVIATIONS</b> .....	<b>IX</b>
<b>LIST OF FIGURES</b> .....	<b>X</b>
<b>LIST OF TABLES</b> .....	<b>XII</b>
<b>TABLE OF CONTENTS</b> .....	<b>XIII</b>
<b>CHAPTER 1: INTRODUCTION</b> .....	<b>1</b>
1.1 PROJECT BACKGROUND.....	1
1.2 PROJECT SPECIFICATION .....	2
1.2.1 <i>Aims</i> .....	2
1.2.2 <i>Objectives</i> .....	2
<b>CHAPTER 2: LITERATURE REVIEW</b> .....	<b>3</b>
2.1 BONE .....	3
2.1.1 <i>Structure</i> .....	3
2.1.2 <i>Composition</i> .....	4
2.1.3 <i>Desirable properties for engineered replacements</i> .....	5
2.2 CALCIUM PHOSPHATES .....	6
2.3 BONE GRAFTS .....	8
2.3.1 <i>Autografts</i> .....	8
2.3.2 <i>Isografts</i> .....	8
2.3.3 <i>Allografts</i> .....	8
2.3.4 <i>Xenografts</i> .....	8
2.3.5 <i>Synthetic bone grafts</i> .....	8
2.4 AVIAN EGG .....	9
2.4.1 <i>Eggshell</i> .....	9
2.4.2 <i>Albumen</i> .....	10
2.4.3 <i>Yolk</i> .....	11
2.4.4 <i>Indicators of Freshness and Quality</i> .....	11
2.5 METHODS OF APATITE SYNTHESIS.....	12
2.5.1 <i>Precipitation</i> .....	12
2.5.2 <i>Hydrothermal precipitation</i> .....	14

2.5.3	<i>Microwave-assisted precipitation</i> .....	14
2.5.4	<i>Sonochemical synthesis</i> .....	15
2.5.5	<i>Sol-gel synthesis</i> .....	16
2.5.6	<i>Emulsion techniques</i> .....	17
2.5.7	<i>Protein-templated synthesis</i> .....	17
2.5.8	<i>Membrane-templated synthesis</i> .....	18
2.5.9	<i>Albumen-mediated synthesis as a potential route</i> .....	18
<b>CHAPTER 3: THEORETICAL BACKGROUND</b> .....		<b>19</b>
3.1	CHARACTERISATION TECHNIQUES .....	19
3.1.1	<i>Electron microscopy</i> .....	19
3.1.2	<i>Thermal analysis</i> .....	20
3.1.3	<i>X-ray diffractometry (XRD)</i> .....	22
3.1.4	<i>Fourier transform infrared spectroscopy (FTIR)</i> .....	24
<b>CHAPTER 4: EXPERIMENTAL METHODOLOGY</b> .....		<b>26</b>
4.1	PREPARATION OF EGG COMPONENTS FOR ANALYSIS .....	26
4.2	PREPARATION OF PRECURSOR SOLUTIONS .....	27
4.2.1	<i>Calcium sources</i> .....	27
4.2.2	<i>Phosphate sources</i> .....	28
4.2.3	<i>Other solutions</i> .....	28
4.3	MICROWAVE-ASSISTED SYNTHESIS.....	29
4.3.1	<i>Experiment 1 (MIC1)</i> .....	29
4.3.2	<i>Experiment 2 (MIC2)</i> .....	30
4.4	ALBUMEN-MEDIATED SYNTHESIS.....	31
4.4.1	<i>Experiment 1 (ALB1)</i> .....	31
4.4.2	<i>Experiment 2 (ALB2)</i> .....	32
4.4.3	<i>Experiment 3 (ALB3)</i> .....	32
4.5	CHARACTERISATION .....	33
4.5.1	<i>SEM</i> .....	33
4.5.2	<i>XRD</i> .....	33
4.5.3	<i>DTA-TGA</i> .....	33
4.5.4	<i>FTIR</i> .....	34
<b>CHAPTER 5: RESULTS AND ANALYSIS</b> .....		<b>35</b>
5.1	EGGSHELL.....	35
5.1.1	<i>SEM</i> .....	35
5.1.2	<i>DTA-TGA</i> .....	38
5.2	MICROWAVE-ASSISTED SYNTHESIS.....	39
5.2.1	<i>Experiment 1 (MIC1)</i> .....	39

5.2.2	<i>Experiment 2 (MIC2)</i> .....	42
5.3	ALBUMEN-MEDIATED SYNTHESIS.....	44
5.3.1	<i>Experiment 1 (ALB1)</i> .....	44
5.3.2	<i>Experiment 2 (ALB2)</i> .....	52
5.3.3	<i>Experiment 3 (ALB3)</i> .....	59
<b>CHAPTER 6:</b>	<b>DISCUSSION</b> .....	<b>67</b>
6.1	MICROWAVE-ASSISTED SYNTHESIS.....	67
6.2	ALBUMEN-MEDIATED SYNTHESIS.....	67
6.3	COMPARISON OF SYNTHESIS METHODS.....	69
<b>CHAPTER 7:</b>	<b>CONCLUSIONS</b> .....	<b>70</b>
7.1	MICROWAVE-ASSISTED SYNTHESIS.....	70
7.2	ALBUMEN-MEDIATED SYNTHESIS.....	70
<b>CHAPTER 8:</b>	<b>RECOMMENDATIONS FOR FURTHER WORK</b> .....	<b>72</b>
8.1	REDUCTION OF CRYSTALLITE SIZE.....	72
8.2	REMOVAL OF PROTEIN.....	72
8.3	PROPERTIES OF ALBUMEN.....	72
8.4	EFFECT OF PRECURSOR CHOICE.....	73
8.5	REMOVAL OF CALCIUM OXIDE IMPURITIES.....	73
8.6	CELL STUDIES AND BIOLOGICAL DATA.....	73
8.7	OTHER POTENTIAL SYNTHESIS METHODS.....	74
8.7.1	<i>Membrane templated</i> .....	74
8.7.2	<i>Yolk templated</i> .....	74
<b>CHAPTER 9:</b>	<b>PROJECT COSTING</b> .....	<b>75</b>
<b>REFERENCES</b> .....		<b>76</b>
<b>APPENDICES</b> .....		<b>A</b>
APPENDIX 1:	DIMENSIONED SEM OF ALB1.....	A
APPENDIX 2:	DIMENSIONED SEM OF ALB2.....	E
APPENDIX 3:	DIMENSIONED SEM OF ALB3.....	I

# Chapter 1: Introduction

*The introduction provides the background and context of the report, indicating the potential importance and value of the research. The aims and objectives of the project are also described.*

## 1.1 Project Background

Calcium phosphates have a wide range of applications, from hard tissue engineering to drug delivery mechanisms [1–4], as well as in non-medical applications such as packing media for column chromatography, gas sensors and catalysts [5]. Calcium phosphates are typically both biocompatible and bioresorbable, with the resorption rate being dependent on the Ca/P ratio. Stoichiometric HAp has a Ca/P ratio of 1.67 and is around 20 times less soluble than  $\beta$ -TCP, which has a Ca/P of 1.5 [6]. For bone tissue engineering applications, the resorption rate of an implanted material should match the rate of bone formation [7].

Bone is a natural biocomposite material composed of non-stoichiometric carbonated hydroxyapatite (CHAp) nanoparticles embedded in a collagen matrix [8]. Natural bone mineral has a Ca/P ratio of around 1.65 [9], low crystallinity [10] and contains minor substitutions of  $\text{Mg}^{2+}$ ,  $\text{Na}^+$ ,  $\text{Sr}^{2+}$ ,  $\text{F}^-$ ,  $\text{HPO}_4^{2-}$ ,  $\text{CO}_3^{2-}$  and  $\text{SiO}_4^{2-}$  [11]. Divalent cationic substitutions, particularly  $\text{Mg}^{2+}$ , have been shown to aid bone growth, calcification and increase bone density [12], as well as play an active role in cell adhesion mechanisms [13]. Low crystallinity is also desirable, as it increased bioactivity [14].

Eggshell is composed of 94% calcium carbonate, 1% calcium phosphate, 1% magnesium carbonate, and 4% organic matter [15], as well as smaller quantities of strontium, sodium, iron, potassium and chlorine [16,17]. The presence of such a large number of bioactivity increasing ions, and particularly the high magnesium content, make eggshell an excellent precursor for the synthesis of bioactive hydroxyapatite.

Hydroxyapatite has a nominal composition of  $\text{Ca}_{10}(\text{PO}_4)_6(\text{OH})_2$  and is biocompatible, bioresorbable and osteoconductive, as well as being an excellent carrier of osteoinductive growth factors [18]. Combined with the similarity to natural bone mineral, this leads to hydroxyapatite being a very useful material for hard tissue engineering, especially when combined with ionic substitutions and low crystallinity.

Several methods of HAp synthesis have been developed, with the focus recently being on the production of hydroxyapatite with low crystallinity, small particle sizes and desirable ionic substitutions.

## 1.2 Project Specification

### 1.2.1 Aims

The main aim of this project is to investigate and critically analyse the methods of synthesis currently used to produce apatites, primarily for hard tissue engineering applications.

The project will provide further understanding of the factors affecting apatite production via various synthesis routes as well as with the use of various precursors. This will allow for comparison of the effectiveness of each method, as well as highlighting the possible influence of precursor choice on the properties of the produced apatites.

Characterisation of the produced apatites will be achieved through the use of analytical techniques such as SEM, XRD, DTA-TGA and FTIR, which allow for both qualitative and quantitative analyses.

### 1.2.2 Objectives

- 1) Explore and evaluate current synthesis methodologies through an in-depth literature review, including a brief look at methodologies with the potential for application to apatite synthesis, but which are not currently being used for this purpose
- 2) Develop a novel method of synthesising hydroxyapatite from an eggshell precursor, in order to produce magnesium substituted apatites
- 3) Fully characterise and analyse the produced apatites
- 4) Compare the results with that of a more conventional synthesis method in order to critically evaluate the potential of the developed methodology

# Chapter 2: Literature Review

*This chapter presents an in-depth literature review covering topics relevant to the production of apatites for biomedical purposes. The structure and composition of bone is considered, followed by brief descriptions of the different forms of calcium phosphates. Sources of bone grafts are categorised and their advantages and disadvantages discussed. An analysis of the structure and composition of avian eggs is presented along with the rationale for using eggshell as a source of calcium for hard tissue engineering. Synthesis methods relevant to the production of apatites are then considered.*

## 2.1 Bone

### 2.1.1 Structure

Bone is a functionally gradient biological composite typically consisting of 69% apatite, 22% organic material and 9% water, as given in Table 1. The organic component is primarily composed of collagen, most of which is type-I collagen, with the rest consisting of other proteins such as proteoglycans and glycoproteins [14]. The functionally gradient properties arise from the different structures found within bone; cortical (compact) bone makes up the dense outer layer of bone, and cancellous (spongy) bone makes up the internal portion of the bone. The proportion of mineral is the same in both cortical and cancellous bone [10], and the differing properties are due mainly to the difference in porosity, with 70-80% of the variance in strength dependent upon this [19].

Table 1: Composition of bone [8]

Component	Amount (w/o)
Mineral (apatite)	69
Organic matrix	22
collagen	(90-96% of organic matrix)
others	(4-10% of organic matrix)
Water	9

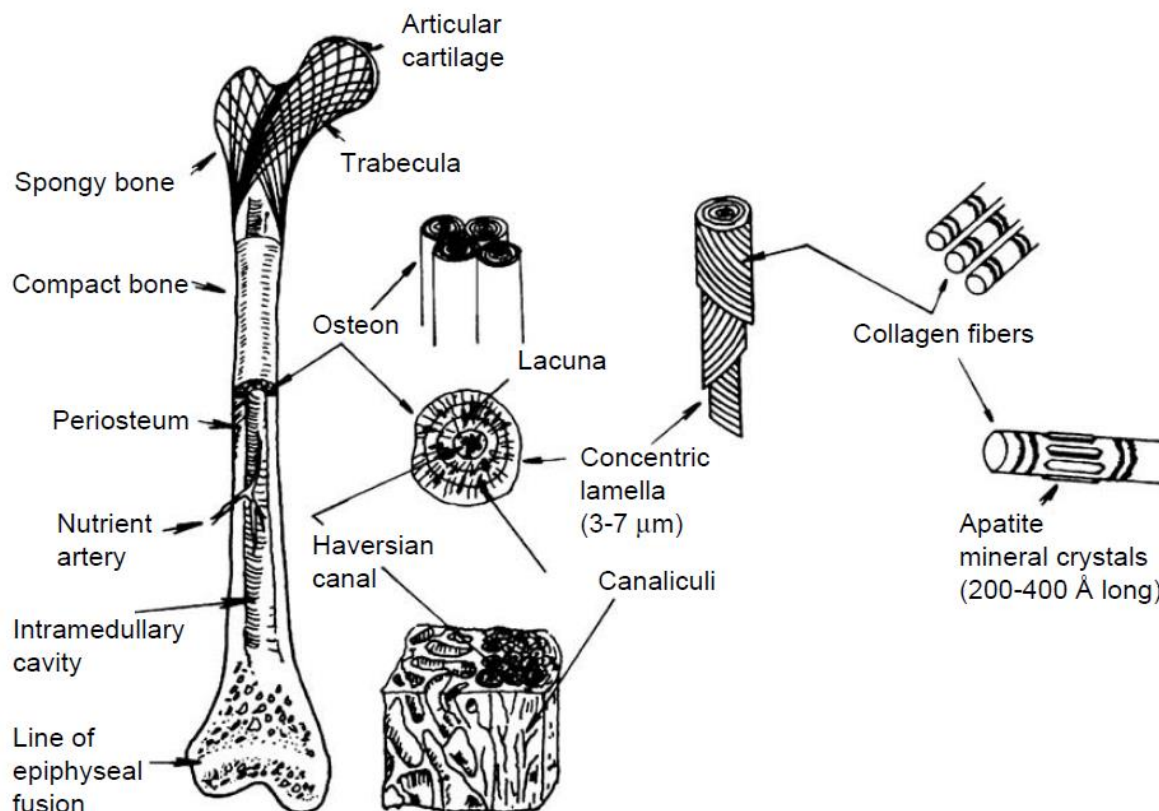


Figure 1: Structural organisation of a typical bone [8]

Needle shaped apatite crystals, with a length of 20-40 nm and a diameter of 1.5-3 nm, are embedded in a collagen fibre matrix [8]. The resulting collagen fibrils run helically and are combined into concentric lamellae. Osteons, which are typically 150-250  $\mu\text{m}$  in diameter, consist of 4 to 20 lamellae arranged around the Haversian canal. Canaliculi supply nutrients to the cells within bone. The structural organisation of bone is shown in Figure 1.

Bone is a living tissue containing four cell types [8,14,20]: osteoprogenitor cells, osteoblasts, osteocytes, and osteoclasts. Osteoprogenitor cells are mesenchymal stem cells, and differentiate into osteoblasts. During osteogenesis, osteoblast cells secrete the collagen organic matrix which is later mineralised [20]. After calcium phosphate deposition, osteocytes, which are mature bone cells, remain encased within the lacunae. Osteoclasts are responsible for the dissolution and resorption of bone, aiding remodelling in response to physical stresses.

### 2.1.2 Composition

The mineral component of bone is composed of poorly crystalline, carbonate-substituted, nonstoichiometric, calcium-deficient apatites, which contain trace ions that improve both the strength and the biological properties [6,10,14,21]. When compared to sintered HAp, biological apatite has a crystallinity of 33-37% [9]. In natural carbonated HAp, phosphate ions are substituted

by carbonate ions; as a person ages, the apatite in their bone becomes more crystalline and more carbonated, so the Ca/P ratio increases towards 1.67 [14]. The compositions of enamel, bone, and HAp are given in Table 2, and it can be seen that HAp has a similar Ca/P ratio to both enamel and bone.

The natural apatitic phase of bone has a nominal composition of  $\text{Ca}_{8.3}(\text{PO}_4)_{4.3}(\text{CO}_3)_x(\text{HPO}_4)_y(\text{OH})_3$ , where  $x$  increases with age and  $x + y = 1.7$  [14].

**Table 2: Comparative compositions of human enamel, bone and hydroxyapatite (HAp) [9]**

	Enamel (wt%)	Bone (wt%)	HAp (wt%)
$\text{Ca}^{2+}$	36.0	24.5	39.6
P	17.7	11.5	18.5
<b>Ca/P molar</b>	<b>1.62</b>	<b>1.65</b>	<b>1.67</b>
$\text{Na}^+$	0.5	0.7	trace
$\text{K}^+$	0.08	0.03	trace
$\text{Mg}^{2+}$	0.44	0.55	Trace
$\text{CO}_3^{2+}$	3.2	5.8	-
$\text{F}^-$	0.01	0.02	-
$\text{Cl}^-$	0.30	0.10	-
<b>Total inorganic</b>	<b>97.0</b>	<b>65.0</b>	<b>100</b>
<b>Organic</b>	<b>1.0</b>	<b>25.0</b>	<b>-</b>
<b>Absorbed H<sub>2</sub>O</b>	<b>1.5</b>	<b>1.5</b>	<b>-</b>

### 2.1.3 Desirable properties for engineered replacements

Ideal materials for tissue replacement are biocompatible, porous, osteoinductive, osteoconductive, mechanically similar, and capable of inducing cell adhesion [6]. It is therefore desirable to produce synthetic apatites with a similar composition, size and morphology to that of the mineral component of natural bone, as these materials will have these properties.

Histological evaluation has shown that, upon implantation, bone formation was more extensive for scaffolds which were prepared without the use of organic solvents, and so use of organic solvents is contraindicated where alternative methods are available [22].

It has been shown that  $\text{NO}_3^-$  and  $\text{NH}_4^+$  are not incorporated into crystalline apatites, except in very limited quantities, meaning that the presence of these ions during synthesis does not affect the composition of the produced apatite [14].

## 2.2 Calcium Phosphates

Calcium phosphates can be synthesised with a variety of compositions. Table 3 summarises the main forms of calcium phosphate along with the properties of these materials. Many of these calcium phosphates can be found in the human body, including hydroxyapatite, dicalcium phosphate, dicalcium phosphate dihydrate, tricalcium phosphate, octacalcium phosphate and amorphous calcium phosphate [23].

Table 3: Calcium phosphates and their properties

Calcium Phosphate	Properties
<b>Monocalcium phosphate anhydrous</b> <i>MCPA, Ca(H<sub>2</sub>PO<sub>4</sub>)<sub>2</sub></i>	- Highly soluble and acidic - Incompatible with biological environments
<b>Dicalcium phosphate anhydrous</b> <i>DCPA, CaHPO<sub>4</sub></i>	- Biocompatible, biodegradable, and osteoconductive - DCPD is a metastable precursor to HAp in bone remodelling
<b>Dicalcium phosphate dihydrate</b> <i>DCPD, CaHPO<sub>4</sub>·2H<sub>2</sub>O</i>	
<b>Tricalcium phosphate</b> <i>α-TCP, β-TCP, Ca<sub>3</sub>(PO<sub>4</sub>)<sub>2</sub></i>	- α and β forms have different crystallographic structures - β-TCP is less degradable - Both polymorphs are widely used as bone substitutes
<b>Tetracalcium phosphate</b> <i>TTCP, Ca<sub>4</sub>(PO<sub>4</sub>)<sub>2</sub>O</i>	- Basic, and soluble at pH <5 - Biocompatible, but poorly biodegradable
<b>Octacalcium phosphate</b> <i>OCP, Ca<sub>8</sub>H<sub>2</sub>(PO<sub>4</sub>)<sub>6</sub>·5H<sub>2</sub>O</i>	- Metastable HAp precursor in bone and teeth
<b>Hydroxyapatite</b> <i>HAp, Ca<sub>10</sub>(PO<sub>4</sub>)<sub>6</sub>(OH)<sub>2</sub></i>	- Osteoconductive and stable except at very low pH - Found in teeth and bone
<b>Calcium-deficient hydroxyapatite</b> <i>CDHAp, Ca<sub>10-x</sub>(HPO<sub>4</sub>)<sub>x</sub>(PO<sub>4</sub>)<sub>6-x</sub>(OH)<sub>2-x</sub></i>	- Similar to bone material but without substitutional ions - Poorly crystalline (1.5 < Ca/P < 1.67)
<b>Carbonated hydroxyapatite</b> <i>CHAp,</i>	- HAp with substitutional carbonate ions - Poorly crystalline
<b>Oxyapatite</b> <i>OxHAp, Ca<sub>10</sub>(PO<sub>4</sub>)<sub>6</sub>O</i>	- Product of the decomposition of HAp
<b>Biphasic calcium phosphate</b> <i>BCP</i>	- Mixture of two calcium phosphates, usually HAp and β-TCP - Composition determines properties
<b>Amorphous calcium phosphate</b> <i>ACP</i>	- Various compositions - Involved in biological transformation of calcium phosphates into HAp

The osteoinductive properties of TCP stimulate local osteoblast activity, leading to body repair. TCP is also highly bioresorbable, and resorbs at a rate of 10-20 times that of HAp [6].

Magnesium substituted β-TCP, also known as Whitlockite, is less soluble than pure β-TCP and more stable at temperatures up to 1450 °C [24]. The substitution of magnesium reduces the plane spacings and prevents the inversion of the crystal structure from β-TCP to α-TCP [24,25].

CHAp can be categorised as A-type and B-type, with CO<sub>3</sub><sup>2-</sup> ions substituting OH<sup>-</sup> ions and PO<sub>4</sub><sup>3-</sup> ions, respectively; A-type CHAp is produced at higher temperatures, whilst B-type CHAp is produced at

lower temperatures [14]. A-type CHAp has a nominal composition of  $\text{Ca}_{10}(\text{PO}_4)_6(\text{CO}_3)_x(\text{OH})_{2-x}$ , whilst B-type substitution produces a nominal composition of  $\text{Ca}_{10-x/2}(\text{PO}_4)_{6-x}(\text{CO}_3)_x(\text{OH})_2$  [14].

The crystallographic structure of pure HAp is shown in Figure 2. This structure allows for the inclusion of substitutional ions, including  $\text{Na}^+$ ,  $\text{K}^+$ ,  $\text{Mg}^{2+}$ ,  $\text{Sr}^{2+}$ ,  $\text{Cl}^-$ ,  $\text{F}^-$ ,  $\text{CO}_3^{2-}$ ,  $\text{SiO}_4^{2-}$  and  $\text{HPO}_4^{2-}$  [11]. The presence of substitutional ions distorts the crystal lattice and so reduces crystallinity, resulting in increased bioactivity [14].

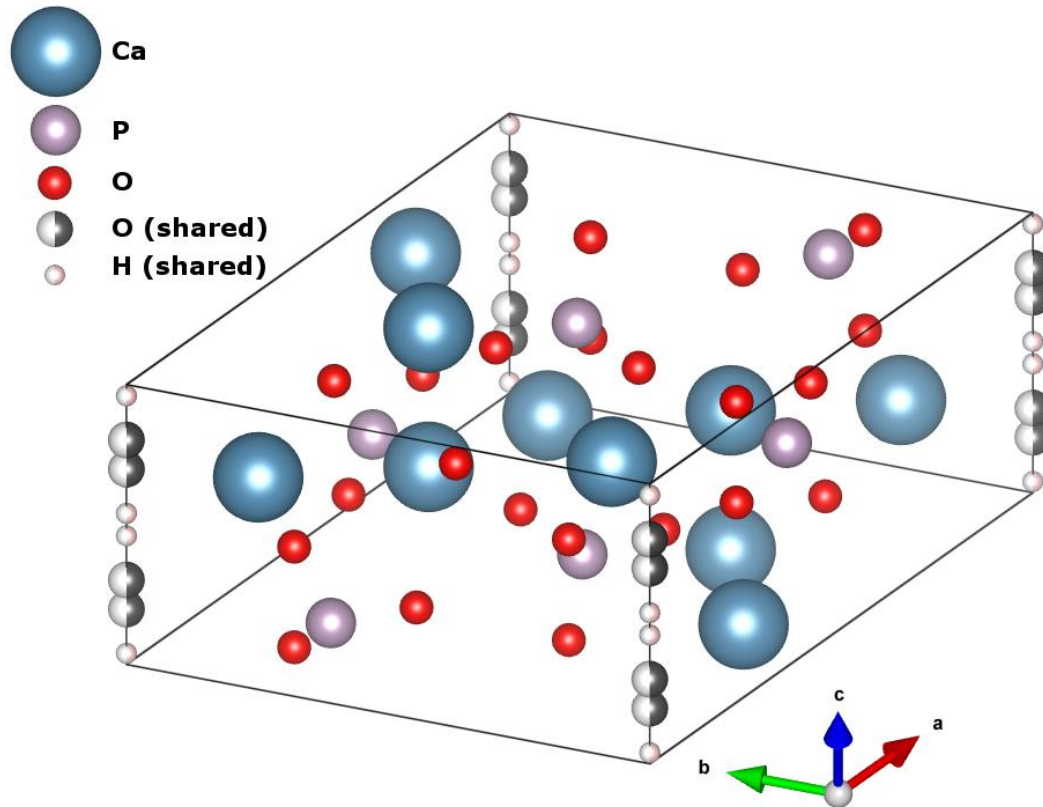


Figure 2: Unit cell of the hydroxyapatite crystal structure, generated from data by Hughes et al [26]

## 2.3 Bone Grafts

There are multiple sources available for bone grafts; these can be categorised as homografts, xenografts and synthetic grafts. Homografts are grafts taken from a donor of the same species as the recipient and can be subdivided into three main types: autografts, isografts and allografts. The advantages and disadvantages of each type of graft are explained here.

### 2.3.1 Autografts

Autografts use tissue from a donor site elsewhere within an individual in order to repair or replace lost or damaged tissue. This type of transplant is considered to be the “gold standard” because of the lack of immunological rejection and inherent compatibility of using a patient’s own tissues [27,28]. However, the supply of suitable tissues is limited and use of autografts leads to donor site morbidity, additional scarring, and prolonged operations.

### 2.3.2 Isografts

When the patient has an identical twin, Isografts are sometimes used. Material is taken from the genetically identical individual and implanted into the patient. The transplanted tissue is not rejected by the recipient’s immune system because it is genetically similar to the recipient’s own tissues, making it very similar to autografts.

### 2.3.3 Allografts

The use of tissues from a genetically dissimilar donor can lead to complications due to disease transmission, infection, and immunological rejection [8,29]. Despite this, it is widely used because of the potential use cadaver donors, which greatly increases the available supply. Tissues can also be taken from living individuals, but this is typically only the case for tissues and organs such as blood, bone marrow, or kidneys. Rejection rates of over 50% have been seen with bone allografts [28].

### 2.3.4 Xenografts

Grafts taken from a different species to the recipient are known as xenografts. These carry a significant risk of disease transmission. Histological examinations have shown significant cell reactions to deproteinated bone xenografts which resulted in non-unions of arthrodeses [30].

### 2.3.5 Synthetic bone grafts

Synthetic grafts can be made of materials such as calcium sulphates, HAp, TCP, and bioactive glass ceramics. These avoid the issues of donor site morbidity and disease transmission, but synthetic materials do not generally have the same biological and mechanical properties [31].

## 2.4 Avian Egg

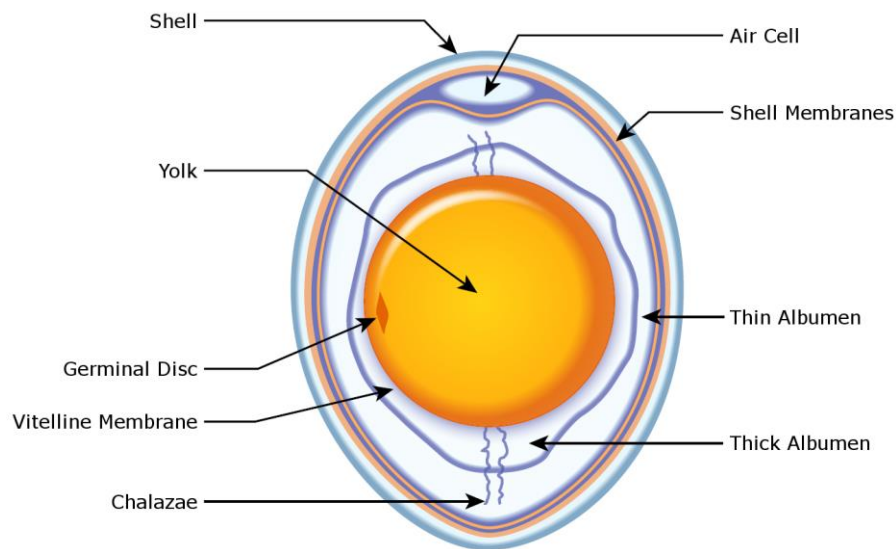


Figure 3: Structure of an avian egg. Adapted from [32]

The three main components of eggs are the eggshell, the albumen and the yolk. Eggshell represents 9-11% of the mass of the egg, albumen represents 60-63%, with the remaining 28-29% consisting of the yolk [32]. An outline of the structure of a typical avian egg is shown in Figure 3.

### 2.4.1 Eggshell

#### 2.4.1.1 Structure

The external surface of eggshell is covered in a thin (10-30  $\mu\text{m}$ ) porous layer known as the cuticle. The mineral layer can be subdivided into the outer palisade layer, which consists of a 200  $\mu\text{m}$  thick spongy organic matrix containing dense vertically orientated columnar crystals, and the inner mammillary layer from which the crystals grow [32]. Two membranes separate the eggshell from the albumen, the outer membrane (50  $\mu\text{m}$ ) and the more densely packed inner membrane (20  $\mu\text{m}$ ) [32]. The inner and outer membranes are connected except at the blunt pole of the egg, where an air cell is present [33].

#### 2.4.1.2 Composition

Eggshell is composed of around 94% calcium carbonate, 1% calcium phosphate, 1% magnesium carbonate, and 4% organic matter, which is mostly protein [15]. Witoon [16] presented a more complete compositional analysis of calcined eggshell, shown in Table 4, indicating that calcined eggshell is 1.63% magnesium oxide by weight. Other work has also demonstrated the presence of 0.09% sodium in eggshell [17]. The calcium phosphate component of eggshell is mainly in the form of tricalcium phosphate [34]. This composition makes eggshell an excellent precursor for HAp synthesis for bone tissue engineering because magnesium has been found to aid bone growth, calcification

and increase bone density [12]. Divalent cations such as  $Mg^{2+}$  also play an active role in cell adhesion mechanisms [13].

Table 4: Composition of calcined eggshell [16]

	CaO	MgO	P <sub>2</sub> O <sub>5</sub>	SO <sub>3</sub>	K <sub>2</sub> O	SrO	Cl	Fe <sub>2</sub> O <sub>3</sub>	CuO
Proportion (wt%)	97.42	1.63	0.52	0.26	0.08	0.05	0.02	0.01	0.01

The cuticle layer is predominantly organic, typically being composed of 90% insoluble protein and 5% carbohydrate [32]. The mammillary layer and base of the palisade layer contain eggshell matrix proteins which support the calcium carbonate crystals; many of these are also expressed in albumen, including ovalbumin, lysozyme, ovotransferrin, osteopontin and clusterin [32].

## 2.4.2 Albumen

### 2.4.2.1 Structure

Egg white consists of two distinct layers with the thick albumen surrounding the yolk and the thin albumen nearest the shell. There are also twisted protein structures known as chalazae which anchor the yolk in the centre of the albumen.

### 2.4.2.2 Composition

The main component of egg white is water, which accounts for more than 80% of egg white [32]. Approximately 40 different proteins have been identified in egg white, most of which are water-soluble [35]. In terms of dry weight, egg white is composed of 54% ovalbumin, 12-13% ovotransferrin, 11% ovomucoid, 3.5% lysozyme, 2% G2 and G3 ovoglobins, and 1.5-3% ovomucin [32].

Ovalbumin is the main protein responsible for the gelling properties of egg white and it is the conversion to S-ovalbumin which is responsible for this [32]. Conversion to the more thermally stable S-ovalbumin is the result of denaturation which occurs even during low temperature storage; the rate of denaturation is increased by high pH and high temperatures [32]. Both ovalbumin and ovomucoid have been shown to activate immunoglobulin E (IgE)-mediated allergic reactions [32,36].

Ovomucin is present in albumen in soluble and insoluble subtypes. Both thick albumen and thin albumen contain the soluble form of ovomucin, but the insoluble form is only present in thick albumen [32].

It is important to maintain the distinction between albumen and albumin; albumen refers to the egg white, which is a mix of proteins, whilst albumin refers to a specific class of water-soluble proteins.

## 2.4.3 Yolk

### 2.4.3.1 Structure

A 10 µm thick protein membrane known as the vitelline membrane encapsulates the yolk, which is made up of both white and yellow yolk. White yolk accounts for 2% of the total weight of the yolk and mainly consists of structures from which the embryo is supported, such as the germinal disc [32]. The yellow yolk is mainly plasma containing lipid-protein particles; the particles can be separated into spheres (4-150 µm diameter), profiles (12-48 µm) and granules (0.3-2 µm) [32].

### 2.4.3.2 Composition

Egg yolk contains 51% water, with the dry fraction being 62.5% lipid and 33% protein [32]. The dry fraction consists primarily of lipoproteins, namely low density lipoprotein (LDL) and high density lipoprotein (HDL), which are composed of 80-90% lipid and 10-20% protein, and 20% lipid and 80% protein, respectively [35].

The emulsifying ability of egg yolk comes from two components. LDLs constitute approximately two-thirds of dry mass of egg yolk and are formed from a lipid core surrounded by phospholipids and proteins; the amphiphilic properties of phospholipid and apoproteins present in LDLs are responsible for the emulsifying properties of egg yolk [32]. Phosvitin also acts as an emulsifier and is particularly emulsion-stabilising [35].

Another interesting component of egg yolk is bone peptides; these are biologically active proteins which can be utilised to enhance bone growth. Experiments have shown that the use of yolk water-soluble protein (YSP) can lead to an increase of 50% in bone elongation rate compared to a control [37].

## 2.4.4 Indicators of Freshness and Quality

The freshness and quality of eggs can be determined qualitatively by certain factors. The thick albumen of low quality eggs is much less viscous than in high quality eggs and can be indistinguishable from the thin albumen [32]. In addition, the chalazae of fresh eggs are more prominent than those of less fresh eggs. Interestingly, the colour of the eggshell is not an indicator of freshness or quality and is dependent only upon the breed of chicken [32].

## 2.5 Methods of Apatite Synthesis

Numerous methods exist for the synthesis of HAp; the choice of which of these methods to use, along with the various experimental parameters, is generally determined by the desired HAp size and morphology. Synthesis methods include: precipitation [38–43], hydrothermal [5,44–46], microwave [17,47–50], sonochemical synthesis [51–53], sol-gel [54–56], micro-emulsion [57–60], protein-templated [61] and membrane-templated [62].

### 2.5.1 Precipitation

HAp synthesis can be achieved by precipitation from an aqueous solution, producing large quantities with low costs [63]. In a typical precipitation reaction, an aqueous phosphate source is added in a dropwise fashion to an aqueous calcium source.

Viswanath and Ravishankar [38] described the effect of temperature and pH on the morphology of HAp crystals; this relationship is shown in Figure 4. With a temperature of 423 K, equiaxed morphology with a diameter of around 30 nm was produced at pH 11, whilst rods 100 nm by 25 nm were produced at pH 9, and platelets with dimensions of 200 nm by 5  $\mu\text{m}$  were produced at pH 6.

Similarly, Zhang et al [46] demonstrated the dependence of morphology on pH and went further to explain the mechanism behind this, which is shown schematically in Figure 5. Whilst Zhang et al used a hydrothermal synthesis method with a temperature of 180  $^{\circ}\text{C}$  (450 K), the results are consistent with those achieved by Viswanath and Ravishankar [38] and so it is expected that the same mechanisms should apply to other methodologies, unless another factor is present in a particular reaction which itself has an effect on morphology.

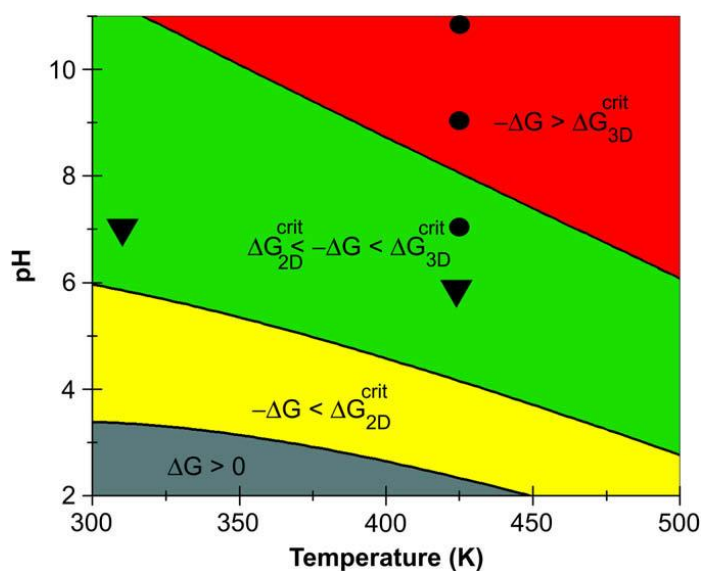


Figure 4: Effect of temperature and pH on the produced morphology of HAp crystals, with experimental data corresponding to two-dimensional and three-dimensional shapes are marked as ▼ and ●, respectively [38]

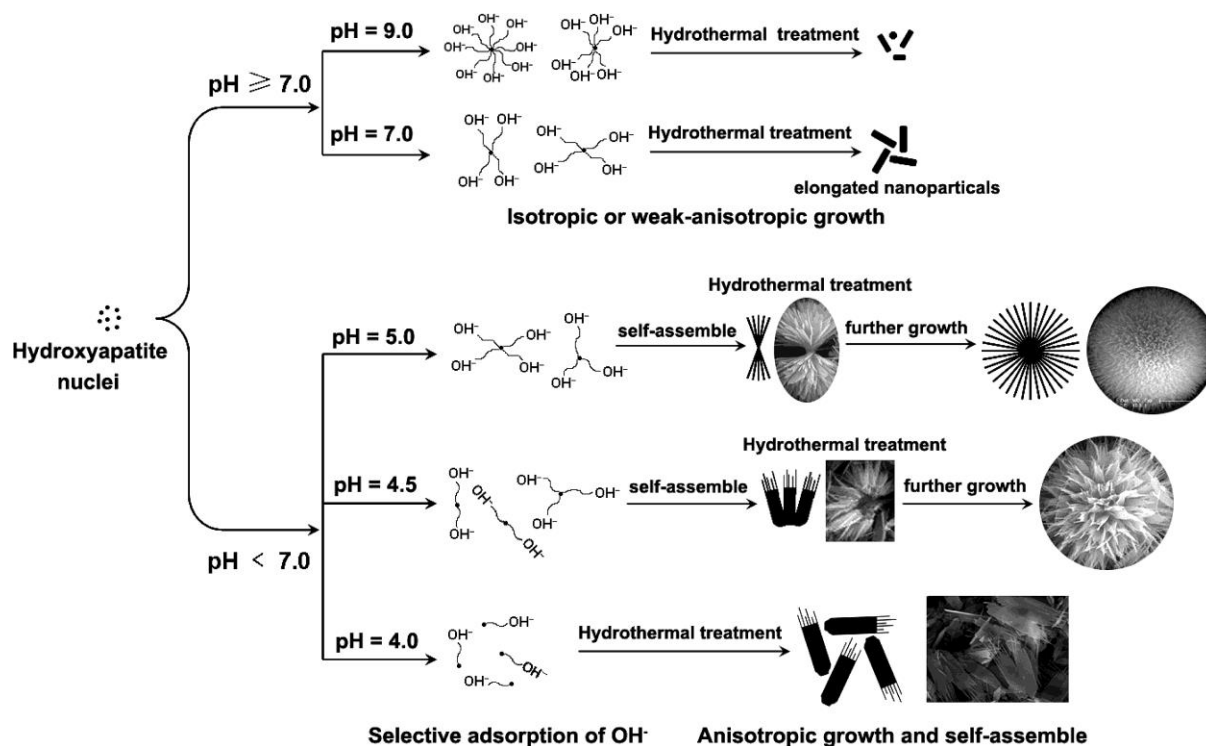


Figure 5: Schematic showing the variation of HAP morphology with  $\text{OH}^-$  concentration at 180 °C (450 K) [46]

Temperatures of less than 60 °C were shown by Bouyer et al [39] to produce monocrystalline HAP particles, with temperatures greater than this favouring the formation of polycrystalline particles.

Cengiz et al [40] presented the synthesis of HAP nanoparticles from  $\text{CaCl}_2$  and  $\text{K}_2\text{HPO}_4$  in the presence of either simulated body fluid (SBF) or calcium phosphor tris (CaPTris). SBF produced needle-shaped HAP nanoparticles with a diameter of 10-50 nm and a length of 120-450 nm, whilst CaPTris produced HAP nanoparticles with an irregular morphology and dimensions in the range of 100-500 nm. Analysis of X-ray diffraction results indicated that these particles consisted of crystallites with sizes of the order of 20 nm.

Wang et al [41] investigated the effects of varying the solvent, dispersant, method of drying, initial pH, and reaction temperature. HAP was synthesised from  $\text{Ca}(\text{NO}_3)_2 \cdot 4\text{H}_2\text{O}$  and  $(\text{NH}_4)_2\text{HPO}_4$  and the size, morphology and dispersibility were characterised. The amount of ethanol in the solvent system was shown to correlate with worse dispersibility and larger particle sizes, with ethanol producing particles with a diameter of 100-150 nm compared to 20-30 nm in water; this was due to the lower solubility of HAP in ethanol compared to water. It was further shown that ethanolamine was superior as a dispersant compared to PEG-12000 and citric acid, but no comparison was made to a system without a dispersant. Vacuum drying decreased dispersibility, whilst freeze drying produced slightly larger particles compared to atmospheric drying, which suggests that particle shrinkage may be prevented by freeze drying, meaning that the particle morphology is better preserved. However, freeze drying is complex, energy intensive and requires long treatment times. Investigation of the

effect of pH demonstrated similar results to that previous described and further demonstrated the production of a predominately  $\beta$ -TCP biphasic mixture at a pH of 8, and a predominantly HAp biphasic mixture at a pH of 9. At a pH of 10, a mixture of spherical and rod-shaped particles were produced at 25 °C, spherical particles at 40 °C, rod-like at 60 °C and bamboo-leaf-like at 80 °C; this appears to run contrary to the findings of Viswanath and Ravishankar [38] which suggest that spherical or near-spherical morphologies should have been produced for all temperatures within this range.

Elongated nanorods with a diameter of 50 nm and length of 1  $\mu$ m were produced by Swain and Sarkar [42] from  $\text{Ca}(\text{CH}_3\text{COO})_2$  (calcium acetate) and  $\text{KH}_2\text{PO}_4$  at a pH of 4. The nanorods were found to be HAp with low crystallinity when dried at 80 °C, but decomposed to 90%  $\beta$ -TCP when heated to 1000 °C, further decomposing at 1250 °C into a triphasic mixture of 56%  $\alpha$ -TCP, 30%  $\beta$ -TCP and 12% HAp. Spherical nanoparticles with a diameter of 60 nm were produced from  $\text{Ca}(\text{NO}_3)_2 \cdot 4\text{H}_2\text{O}$  and  $(\text{NH}_4)_2\text{HPO}_4$  at a pH at 10; these were found to have a lower crystallinity after drying compared to the produced nanorods and were thermally stable up to 1250 °C.

Landi et al [43] synthesised B-type carbonated hydroxyapatite from  $\text{Ca}(\text{NO}_3)_2 \cdot 4\text{H}_2\text{O}$ ,  $(\text{NH}_4)_2\text{HPO}_4$  and  $\text{NaHCO}_3$ . The produced CHAp was shown to be less crystalline and demonstrated increased solubility in both *in vitro* and *in vivo* tests.

### 2.5.2 Hydrothermal precipitation

Hydrothermal methods utilise sealed pressure vessels to maintain elevated temperatures and pressures. The Ca/P ratio is improved by an increase in hydrothermal pressure or temperature [64].

Riman et al [5] produced HAp nanoparticles via a hydrothermal reaction between  $\text{Ca}(\text{NO}_3)_2$  and either  $(\text{NH}_4)_2\text{HPO}_4$  or  $(\text{NH}_4)\text{H}_2\text{PO}_4$ . Needle-like morphologies were observed with particle sizes in the range of 20-300 nm. A dependence of particle size upon temperature was demonstrated, with particle sizes increasing from 14 nm at 50 °C to 44 nm at 200 °C.

Zhang and Darvell [44] prepared highly crystalline HAp whiskers by hydrothermal synthesis from  $\text{Ca}(\text{NO}_3)_2 \cdot 4\text{H}_2\text{O}$  and  $(\text{NH}_4)_2\text{HPO}_4$  in the presence of acetamide which increases the pH as it hydrolyses. The initial pH was 3 and increased to 5-6 during synthesis. The concentration of acetamide affected the aspect ratio of the produced whiskers, with higher concentrations producing longer whiskers with lower aspect ratios.

### 2.5.3 Microwave-assisted precipitation

Siddharthan et al [17] reported the production of nano-spherical HAp, with diameters of 50 nm, from eggshell via microwave irradiation with a power of 800 W for 15 minutes. Minor substitutions of Mg,

Sr, Si and Na were shown and it was demonstrated that these did not affect the thermal stability of the produced apatites.

Han et al [47] developed a microwave hydrothermal methods which was used to produce nano-sized HAp from  $\text{H}_3\text{PO}_4$  and  $\text{Ca}(\text{OH})_2$  at 600 psi and 300 °C. Mixed phases of  $\text{Ca}(\text{OH})_2$ , DCPA and HAp were found for microwave energies of 450 W or less, with 550 W producing phase-pure HAp after an irradiation of just 4 minutes. Needle-shaped morphologies were produce with dimensions of 4-15 nm by 20-50 nm, as well as nano-spheres with diameter of 10-30 nm.

Liu et al [48] demonstrated the synthesis of HAp from  $\text{Ca}(\text{NO}_3)_2 \cdot 4\text{H}_2\text{O}$  and  $\text{Na}_2\text{PO}_4$  at various pH values in the presence of ethylenediaminetetraacetic acid (EDTA). Solutions were irradiated at a power of 700 W for 30 minutes, with a working cycle of 6 second on and 10 seconds off. Nanorods with a diameter of 40 nm and length of 400 nm were produced at a pH of 9, and bow-knot like structures were produced, with bundles of nanorods with diameters of 150 nm and length of 1-2  $\mu\text{m}$  connected at a central point, at a pH of 11. Flower-like structures with a diameter of 2-4  $\mu\text{m}$  were produced at a pH of 13.

Building on the work of Liu et al [48], Mg substituted b-type carbonated HAp with a flower-like morphology was produced by Kumar et al [49] through microwave conversion of eggshell. EDTA was used as a chelating agent to form a Ca-EDTA complex and  $\text{Na}_2\text{HPO}_4$  was used as the phosphate source. An initial pH of 13 was used and the mixture was irradiated in a microwave at 600 W for 10 minutes. Analysis indicated the incorporation of  $\text{Mg}^{2+}$  and  $\text{CO}_3^{2-}$  in the produced sample. Leaf-like flakes formed the flower-like structures and measured 100-200 nm by 0.5-1  $\mu\text{m}$ , extending radially from the centre.

#### 2.5.4 Sonochemical synthesis

The use of ultrasonic irradiation significantly increases the rate of synthesis. Acoustic cavitation leads to the generation and collapse of bubbles which release concentrated energy in very short times, with heating and cooling rates greater than  $10^{10}$  K/s [65]. Cavitation implosions are very localised and generate transient temperatures of 5000 K and pressures of 1000 bar, allowing access to a reaction space normally inaccessible [66]. Areas of high supersaturation are created during cavitation, and so rapid nucleation occurs [67]. Homogenisation also plays a role in sonochemistry and acts to reduce agglomeration through the intense mixing caused by microstreaming, jetting and shockwaves generated by cavitation [53].

Poinern et al [51] used sonication to produce HAp with a particle size of 30 nm from  $\text{Ca}(\text{NO}_3)_2 \cdot 4\text{H}_2\text{O}$  and  $\text{K}_2\text{HPO}_4$ . The mixture was irradiated with ultrasound with a frequency of 30 kHz for a processing

time of 1 hour at 50 W, 25 W and 0 W. Poinern et al demonstrated that the use of sonication reduced particle sizes, from 230 nm with no irradiation, to 88 nm and 58 nm for irradiation at 25 W and 50 W, respectively.

The effect of dilute gelatine on the sonochemical synthesis of HAp was investigated by Brundavanam et al [52].  $\text{Ca}(\text{NO}_3)_2 \cdot 4\text{H}_2\text{O}$  and  $\text{KH}_2\text{PO}_4$  were mixed with dilute gelatine and sonicated at a frequency of 30 kHz with a power of 50 W. It was found that gelatine concentration had a large effect on particle size when there was no sonication, with higher concentrations producing smaller particles, but no variation of particle size with gelatine concentration was observed when there was sonication. Particle sizes of 30 nm were produced with sonication, compared to particle sizes of 90-230 nm produced without.

Zou et al [53] combined sonochemical and microwave irradiation to produce HAp nano-rods with a diameter of 6 nm and length of 30 nm, attaining a yield of 98.8% in an ultra-short period of 5 minutes. The product had a very high dispersibility and very low agglomeration. Pulsed ultrasound with a frequency of 25 kHz and power of 720 W was used along with microwave irradiation at a power of up to 300 W, controlled to maintain a temperature of 80 °C.

### 2.5.5 Sol-gel synthesis

Sol-gel methods rely on the hydrolysis and condensation of precursors, involving a sudden increase in viscosity [14]. Size and morphology can be closely controlled, producing very uniform size distributions with high purity. There are six main stages to sol-gel synthesis, although in practice not all of these may be followed: hydrolysis, polymerisation, gelification, drying, dehydration, and densification [14].

Haddow et al [54] synthesised apatite films from calcium acetate and one of phosphoric acid, phosphorous pentoxide and triethyl phosphite, via a sol-gel process. The Ca/P ratio was dependent both on the solvent used and the phosphor precursor with a variation from 0.34 to 1.62. Triethyl phosphite in a water solvent proved best, however for phosphoric acid the Ca/P ratio was increased by the use of an ethanediol solvent but still remained low at around 0.7.

Vijayalakshmi and Rajeswari [55] produced HAp via a sol-gel synthesis method using calcium acetate and triethyl phosphate in both water and ethanol media; it is important to note that triethyl phosphate is different from the triethyl phosphite used by Haddow et al [54]. The produced HAp had a spherical morphology with a typical diameter of 0.5-1  $\mu\text{m}$  and was not significantly affected by the presence of ethanol.

The production of HAp from  $\text{Ca}(\text{NO}_3)_2 \cdot 4\text{H}_2\text{O}$  and  $\text{P}_2\text{O}_5$  was reported by Fathi and Hanifi [56]. The precursors were dissolved in ethanol, then mixed and stirred for 24 hours, producing a transparent white gel. Agglomerated HAp nanoparticles were produced with crystallite sizes of 30-35 nm.

### 2.5.6 Emulsion techniques

Emulsion techniques aim to limit the growth of particles by separating the reactants into small localised regions, essentially limiting the growth of crystals to the size of the aqueous phase of the emulsion. The terms “reverse emulsion” and “reverse micelle” are often used to denote water-in-oil emulsions in which aqueous solutions are contained within aggregated surfactant molecules in a hydrophobic solvent.

Bose and Saha [57] utilised a microemulsion technique to produce HAp with a particle size of 30-50 nm. A reverse micelle emulsion was formed by mixing NP-5 and NP-12 surfactants in cyclohexane, then adding aqueous solutions of  $\text{Ca}(\text{NO}_3)_2$  and  $\text{H}_3\text{PO}_4$ .

Guo et al [58] used cyclohexane as the oil phase, n-butanol and n-hexanol as cosurfactants and polyoxyethylene and polysorbate 80 surfactants to form a reverse micelle emulsion with aqueous solutions of  $\text{Ca}(\text{NO}_3)_2$  and  $(\text{NH}_4)_2\text{HPO}_4$ . This method produced short nanorods with diameters less than 30 nm and lengths less than 100 nm.

In work presented by Koumoulidis et al [59],  $\text{Ca}(\text{H}_2\text{PO}_4)_2 \cdot \text{H}_2\text{O}$  and  $\text{CaCl}_2$  were prepared in an aqueous solutions and added to n-octane containing cetyltrimethylammonium bromide (CTAB) and 1-butanol as the surfactant and cosurfactants, respectively. Particle sizes of 40-120 nm were attained after calcination at 650 °C for 3 hours.

Hollow spheres were produced by Ye et al [60] for use as a mechanism of drug delivery.  $\text{Ca}(\text{NO}_3)_2$  and  $\text{H}_3\text{PO}_4$  were added to a water and ethanol mixture containing Pluronic  $\text{EO}_{20}\text{PO}_{70}\text{EO}_{20}$  (P123; EO = ethylene oxide, PO = propylene oxide), which has two hydrophilic heads ( $\text{EO}_{20}$ ), with the middle section being hydrophobic at certain temperatures. Hollow nanospheres were produced with a diameter of 60 nm and wall thickness of 12 nm.

### 2.5.7 Protein-templated synthesis

Han et al [61] precipitated HAp from  $\text{Ca}(\text{H}_2\text{PO}_4)_2$  and  $\text{Ca}(\text{OH})_2$  in the presence of bovine serum albumin (BSA). Sonication was used to homogenise the mixture. Rod-like particles were produced with diameters of 60-160 nm and a length of 500 nm. The BSA protein was denatured at a temperature of 90 °C.

## 2.5.8 Membrane-templated synthesis

Neelakandeswari et al [62] synthesised HAp from  $\text{CaCl}_2$  and  $(\text{NH}_4)_2\text{HPO}_4$  solutions separated by inner ESM. The phosphate source was contained within a test tube covered with ESM and placed in a flask containing the calcium precursor. Diffusion was allowed to proceed for 24 hours. Needle-like particles with a width less than 5 nm and length of 50-100 nm were produced at a pH of 9, whilst a pH of 10 or 11 produced slightly shorter rods with diameters of 2-5 nm and lengths of 50 nm.

### 2.5.8.1 Membrane-templated synthesis of non-apatites

Flower-like agglomerates of calcium carbonate were synthesised on an eggshell membrane by Takiguchi [68]. Aqueous calcium chloride and calcium carbonate solutions were separated by an eggshell membrane and diffusion was allowed to occur. Crystallisation proceeded for 1-10 days without stirring. The outer, inner and limiting membranes were not separated, and both directions were tested. Flower-like structures formed on the inner surface of the ESM with a large (10  $\mu\text{m}$ ) hemispherical core with 10  $\mu\text{m}$  long rods extending outwards from the edge in contact with the membrane. Spherical particles with diameters of less than 1  $\mu\text{m}$  formed on the outer surface when in contact with calcium chloride solution, whilst cubic morphologies were produced with side-lengths of around 5  $\mu\text{m}$  resulted from contact with sodium carbonate solution.

Eggshell membrane was used by Dong et al [69] as a template on which to synthesise interwoven ZnO microfibers. ESM was infiltrated with zinc nitrate and subsequently sintered. The structure of the produced ZnO replicated the structure of the ESM template and was composed of crystallites with a size of 4.5 nm.

Su et al [70] demonstrated the production of lead sulphide nanoclusters on an ESM substrate. Calcium prepared outer eggshell membrane was dipped into a solution of lead acetate and acetic acid, washed with deionised water, then immersed in  $\text{Na}_2\text{S}$  solution. Spherical nanoparticles with diameters of 20 nm were deposited on the surface of the ESM.

## 2.5.9 Albumen-mediated synthesis as a potential route

Nouroozi and Farzaneh [71] reported the production of zinc oxide nanorods via an albumen mediated reaction from zinc acetate. The produced nanorods had an average diameter of 90 nm and length greater than 1  $\mu\text{m}$ . Before sintering, the sample was shown to be highly amorphous, with no distinguishable peaks; however, after treatment at temperatures above 400  $^\circ\text{C}$ , crystalline peaks began to appear in the XRD spectra, finally resulting in a highly crystalline material after heat treatment at 700  $^\circ\text{C}$ .

# Chapter 3: Theoretical Background

*This chapter describes the theoretical background behind the characterisation techniques utilised in this report, whilst noting the most common sources of error.*

## 3.1 Characterisation Techniques

### 3.1.1 Electron microscopy

The maximum resolution of a microscope is limited by the wavelength of light used; optical microscopy has a maximum resolution of 200 nm, although resolutions of 20 nm have been achieved through the application of special techniques requiring fluorescence [72]. By utilising the wave-like properties of electrons, electron microscopy can achieve much higher resolutions than optical microscopy, typically of the order of a few nanometres, depending on the type of microscope [73,74]. The wavelength of an electron is related to the energy of the electron, and so the higher the voltage used to accelerate it, the smaller the wavelength, and the higher the maximum resolution. However, the use of electrons requires that the microscope be operated under a vacuum.

Whilst there are myriad forms of electron microscopy, only two will be considered here: scanning electron microscopy and transmission electron microscopy.

#### 3.1.1.1 Scanning electron microscopy (SEM)

The surface morphology of a sample can be imaged at high-resolutions using scanning electron microscopy (SEM); an electron beam is scanned across the surface and the back scattered electrons are detected [75]. Currently, 5nm resolutions are typical [73], although resolutions of 1 nm or below have also been attained [74]. The practical resolution is generally poorer than the diameter of the focused beam due to the electron beam penetrating and diffusing sideways into the specimen [74]. Detailed images may be produced at resolutions over 50,000x [76], and on more advanced systems, up to 100,000x [77].

Typically, electrons are accelerated to 30-60 keV [73], and focused to a diameter of 2-10 nm by condensing lenses [78]. Scan coils direct the beam over the surface in a raster pattern of parallel lines [74], and the backscattered electrons are detected; sometimes low-energy secondary electrons and other radiation are also detected [78].

To avoid an electrical charge being induced on the surface of non-conducting materials by the incident electron beam, a thin layer of gold, typically 3-10 nm thick, is applied before the sample is placed in the microscope [79]; this layer is electrically grounded and so prevents charge from

building up. However, the layer limits the maximum magnification as it becomes visible at high magnifications [73].

A specimen may be tilted in order to show up small surface irregularities which may be hard to see without tilt [74]. Tilt often causes the top and bottom edges of the image to become out of focus and there are a couple of ways in which this issue can be resolved; smaller aperture lenses provide a greater depth of field and so bring more of the image into focus, whilst dynamic focusing operates by varying the power of the final lens progressively as it scans each line [74].

### 3.1.1.2 *Transmission electron microscopy (TEM)*

Transmission electron microscopy (TEM) forms an image by passing an electron beam through the specimen, with contrast produced by differences in beam scattering and diffraction [76]. Due to the need to transmit a reasonable proportion of the incident electron beam through the specimen, very thin samples must be prepared [76]. TEMs require the use of high vacuums and must be continuously evacuated to a pressure less than  $10^{-4}$  mbar [74].

Magnifications can typically be varied between 1,000x and 250,000x, or between 2,500x and 500,000x, but some more modern models, employing five or six imaging lenses, can cover magnifications between 50x and 1,000,000x [74].

High-resolution transmission electron microscopy (HRTEM) is a term used to describe modern TEMs which can achieve sub-nanometre resolutions, and are sometimes termed ultra-high resolution TEMs where crystal lattices are to be studied and atomic resolutions are achieved [74].

## 3.1.2 Thermal analysis

Thermal analysis involves heating whilst continuously measuring certain parameters about the sample. This allows for the determination of the temperature at which certain thermal events occur; thermal events include phase transitions, melting, sublimation, decomposition, glass transition, oxidation, and combustion [80].

There are many types of thermal analysis, but only two will be considered here: thermogravimetric analysis (TGA) and differential thermal analysis (DTA). The combination of these two methods is known as DTA-TGA, and generates more information than the sum of the information obtained from the individual techniques [80].

### 3.1.2.1 *Thermogravimetric analysis (TGA)*

Thermogravimetric analysis (TGA) uses a microbalance to measure the change in mass of a sample as it is heated. This allows for thermal event involving mass changes to be identified.

Although solid samples may have identical nominal compositions, their thermogravimetric behaviour can vary due to defects, porosity and surface properties; single crystals also behave differently to finely ground powders, which in turn behave differently to bulk materials [80]. Small sample sizes ensure uniform heating, and are desirable even in the case of inhomogeneous samples for which a large sample size would be more representative [80].

The main types of thermogravimetric curves are shown in Figure 6, and the descriptions of the thermal event occurring in each of these cases is summarised in Table 5.

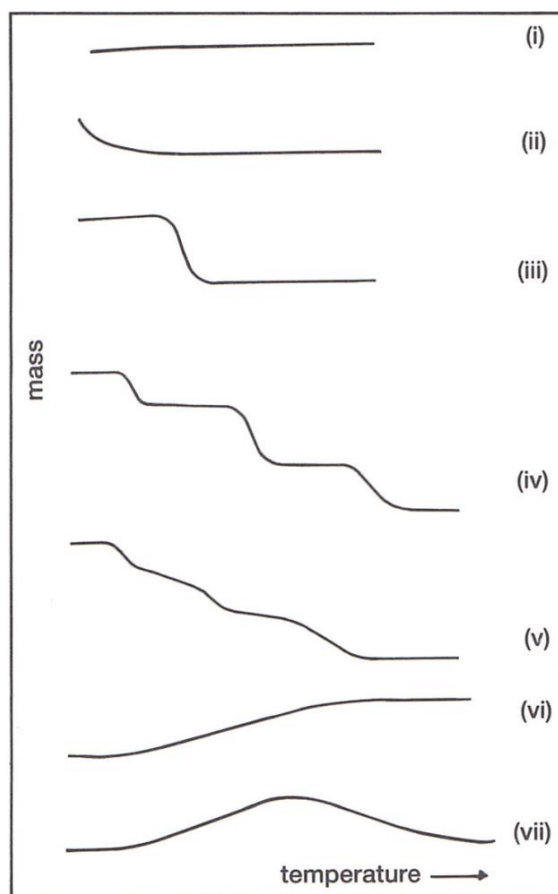


Figure 6: Main types of thermogravimetric curves [80]

Table 5: Main types of thermogravimetric curves, corresponding to Figure 6 [80]

Type	Description
(i)	No decomposition involving loss of volatile products. Other analysis required to check for changes not involving a change of mass.
(ii)	Rapid initial loss due to desorption or drying. Advisable to re-run sample to check whether the mass loss is real; type (i) should be obtained.
(iii)	Single stage decomposition.
(iv)	Multi-stage decomposition with relatively stable intermediates.
(v)	Multi-stage decomposition without stable intermediates.
(vi)	Reaction of sample with surrounding atmosphere (eg. oxidation).
(vii)	Oxidation product which decomposes upon further heating.

### 3.1.2.2 Differential thermal analysis (DTA)

Differential thermal analysis (DTA) compares the temperature of the sample with the temperature of a reference material, typically alumina or carborundum for inorganic samples, whilst both undergo the same heating [80]. Endothermic thermal events cause the temperature of the sample,  $T_s$ , to lag the temperature of the reference,  $T_r$ ; similarly, exothermic events cause the sample temperature to lead the reference temperature [80]. The minimum measurable temperature difference is around 0.01 K [81].

Endothermic events are conventionally shown as negative on DTA graphs, and the endothermic direction is marked [80].

### 3.1.3 X-ray diffractometry (XRD)

The wavelength of X-rays is around 0.1 nm, which is similar to the atomic spacings in a crystalline lattice [75]. This dimensional similarity causes the lattice acts as a three-dimensional diffraction grating [79]. X-rays incident on a material diffract and interfere to produce a diffraction pattern. The angles at which constructive interference occurs can be measured from the diffraction pattern and compared to the characteristic diffraction angles for different materials, allowing for the composition to be determined.

X-ray photons interact with orbital electrons and are scattered. When the path lengths of two coherent electrons differ in by an integer number of wavelengths, constructive interference occurs and so the intensity is increased [79]. The peak intensity occurs at the Bragg angle, which is determined by the lattice parameters of the material. The distance between crystal planes can be calculated using Equation 1, the derivation of which can be seen in Figure 7; where  $n$  is an integer,  $\lambda$  is the wavelength,  $d$  is the plane spacing, and  $\theta$  is the Bragg angle.

Equation 1: Rearranged form of Bragg's Law to allow calculation of planar spacing [75]

$$d = \frac{n\lambda}{2 \sin \theta}$$

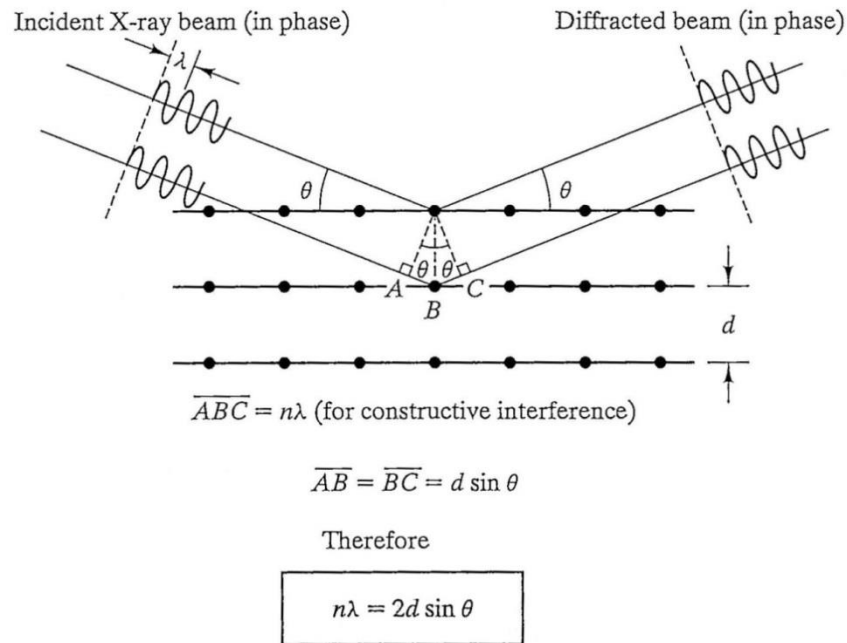


Figure 7: Diagram showing the geometry for the diffraction of X-rays, with the derivation of Bragg's Law [79]

Typically, the X-ray source remains in a fixed position whilst the specimen is rotated by an angle of  $\theta$  and the detector is rotated through an angle of  $2\theta$ . The angle of the detector is measured, and so graphs generated by X-ray diffractometry (XRD) show the intensity at the angle  $2\theta$ ; the schematic layout of such an X-ray diffractometer is shown in Figure 8. However, in some X-ray diffractometers, the specimen remains stationary, and both the source and detector are rotated around it.

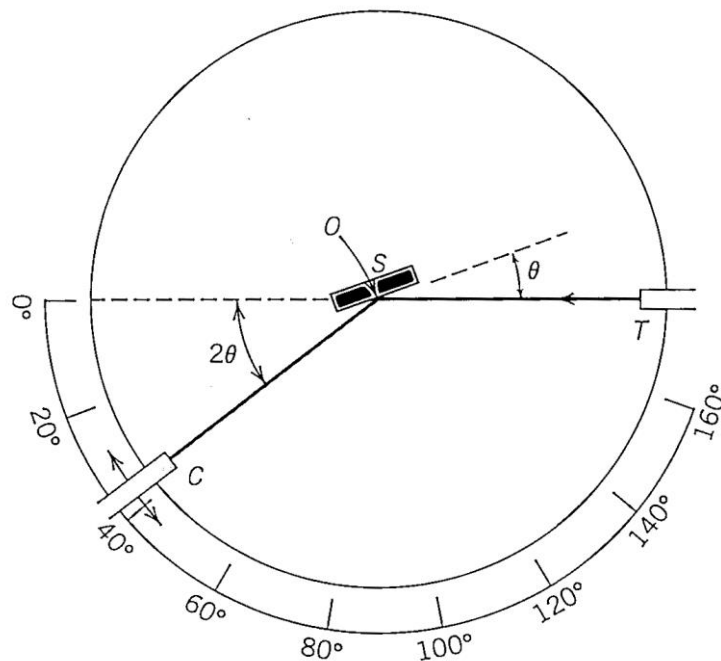


Figure 8: Schematic diagram of an X-ray diffractometer. T = X-ray source, S = specimen, C = detector, O = axis of rotation for specimen and detector [76]

Peak broadening in XRD spectra results from small crystallite sizes or a large number of crystal lattice imperfections. This means that crystallite sizes, or the size of ordered regions of the lattice, can be estimated using the Scherrer equation, given in Equation 2, where  $L$  is the crystallite size,  $K$  is the crystallite shape factor ( $K \approx 0.9$  for spherical or near-spherical particles),  $\lambda$  is the X-ray wavelength,  $B$  is the broadening based on full-width half maximum (FWHM) measured in radians and  $\theta$  is the Bragg angle [82].

Equation 2: Scherrer equation for peak broadening

$$L = \frac{K\lambda}{B \cos \theta}$$

Attempts to refine the Scherrer equation generally focus on different methods of measuring peak broadening, such as the standard deviation or the integral breadth; however, FWHM remains the simplest method by which to calculate peak broadening [83]. The instrument also introduces a small amount of peak broadening and so multiple methods have been developed to remove this from estimations of crystallite sizes [83]. If broadening due to the instrument is not accounted for in numerical analysis, crystallite sizes will be underestimated.

### 3.1.4 Fourier transform infrared spectroscopy (FTIR)

Molecules can be promoted to transition between rotational and vibrational energy levels of the ground electron energy state by infrared irradiation [84]. Bond vibrations can occur as both stretching and bending, with stretching being oscillation along the axis of the bond and bending being oscillation in a direction perpendicular to the axis of the bond [84]. Molecular vibrations occur when the incident infrared radiation is of the same frequency as the vibration, meaning that this frequency of infrared radiation is absorbed by the molecule; absorption bands also occur at multiples of this fundamental frequency [84]. Excitation by infrared radiation requires a dipole moment in the bond and so homonuclear molecules such as  $H_2$ ,  $N_2$  and  $O_2$  are unable to gain vibrational energy [85].

Most interferometers utilise a Michelson interferometer, in which radiation is split by a semi-transparent mirror, on the reflected path it is reflected back by a fixed mirror and recombined with the transmitted radiation which is reflected back by a moveable mirror, and is then reflected into a detector; this is shown schematically in Figure 9 [86]. Constructive and destructive interference occurs when the beams are combined, and so as the position of the moveable mirror varies, there is a sinusoidal variation of the detector signal [86].

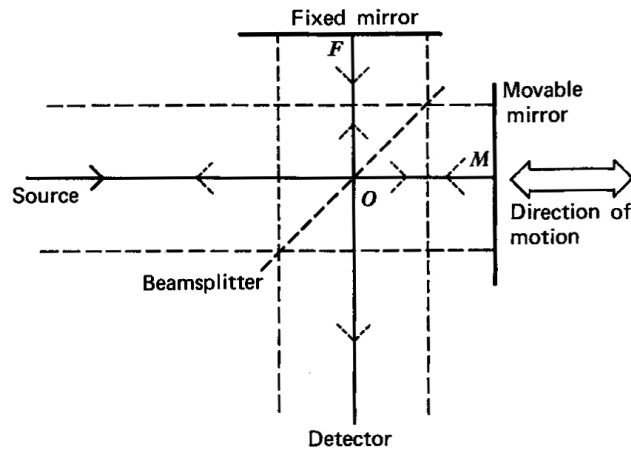


Figure 9: Schematic of a Michelson interferometer [86]

Infrared radiation is generated by a black body, for example by passing a current through a silicon carbide rod, and is reflected off of a diffraction grating to form a spectrum from polychromatic radiation. Detector designs can be categorised as either quantum or thermal. Quantum designs rely on the excitation of electrons in semiconductor materials with small energy gaps, which increases the conductivity of the material and produces a signal [85]. The disadvantage is that for sensitivity in the low-frequency region, very small energy gaps are required, leading to a large amount of noise at room temperature [85]. Thermal designs are more common with thermocouple devices utilising blackened gold foil connected to wires of dissimilar metals which produce an e.m.f. proportional to the temperature [85]. Another thermal design is known as a bolometer and measures the change in resistance of a metal filament or semiconductor crystal [84,85].

Optical components are typically made from sodium chloride or potassium bromide as these do not absorb radiation with wavenumbers greater than  $600\text{ cm}^{-1}$  or  $350\text{ cm}^{-1}$ , respectively, or thallium iodide-bromide in more specialist applications where wavenumbers down to  $250\text{ cm}^{-1}$  are to be looked at [85].

## Chapter 4: Experimental Methodology

*The adopted experimental methodologies are described in this section, starting from the preparation of precursor solutions, moving to the synthesis reactions and finally to the methodologies required for characterisation of the synthesis products.*

### 4.1 Preparation of Egg Components for Analysis

A fresh egg from a local supermarket was cracked open and the contents removed. Both the inner and outer eggshell membranes were separately removed from the eggshell and washed in distilled water. The eggshell was broken into smaller pieces and sections from the flattest part of the eggshell were selected for analysis.

A small sample of each of the inner and outer ESM were dried and mounted separately on SEM stubs using silver paint. Similarly, samples of eggshell were mounted on SEM stubs in various orientations, such that the outer surface, inner surface and a fractured cross-section were visible in in various samples. All samples were gold coated using a sputter coater before SEM analysis.

A sample of eggshell was ground and used for thermal analysis.

## 4.2 Preparation of Precursor Solutions

### 4.2.1 Calcium sources

The calcium precursors were synthesised by following the process shown in Figure 10. The egg shell membrane was separated from eggshells by boiling and subsequent heating to 230 °C; the eggshells were then crushed and ground. The resultant powder was calcined into calcium oxide at 950 °C. Hot calcium oxide was added to either distilled water or acetic (ethanoic) acid to form calcium hydroxide or calcium acetate, respectively.

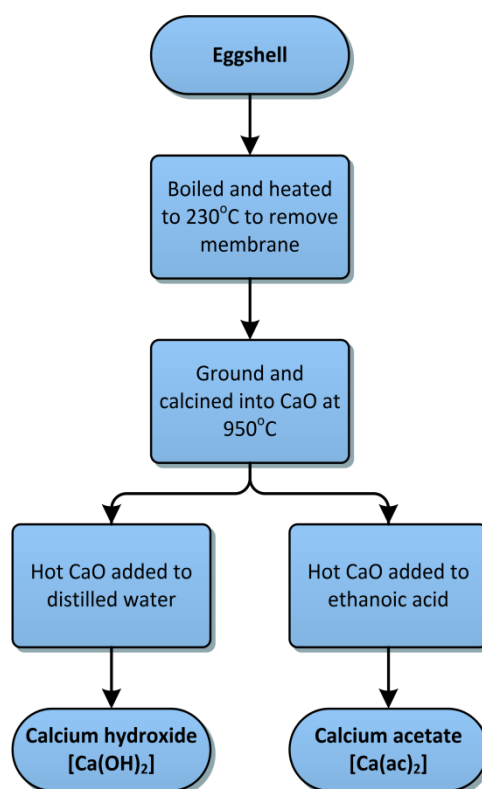


Figure 10: Flowchart of precursor synthesis process

#### 4.2.1.1 Calcium hydroxide

A 0.75 M solution of  $\text{Ca(OH)}_2$  was obtained by adding 4.2 g of calcined CaO to 100 ml of deionised water, and 1.2 M and 1.5 M solutions of  $\text{Ca(OH)}_2$  were obtained by the addition of 3.37 g of calcined CaO to 50 ml and 40 ml of deionised water, respectively.

#### 4.2.1.2 Calcium acetate

Calcium acetate was prepared by first adding 6.9 ml of glacial acetic acid (BDH, 99.5%) to 33.1 ml of distilled water. To this, 3.37 g of hot eggshell-derived CaO was added and the resultant mixture was stirred vigorously until a white homogenous solution was obtained.

## 4.2.2 Phosphate sources

### 4.2.2.1 Orthophosphoric acid

A 0.72 M solution of phosphoric acid was obtained by the slow addition of 3.7 ml of  $\text{H}_3\text{PO}_4$  (Fischer Chemicals, 85%) to 71.3 ml of distilled water.

### 4.2.2.2 Ammonium dihydrogen phosphate (monobasic)

A 0.72 M solution of ammonium dihydrogen phosphate was obtained by dissolving 6.2 g of  $(\text{NH}_4)_2\text{H}_2\text{PO}_4$  (Sigma-Aldrich, 98.5%) in 50 ml of distilled water then adding distilled water to increase the volume to 75 ml.

### 4.2.2.3 Diammonium hydrogen phosphate (dibasic)

A 0.45 M solution of diammonium hydrogen phosphate was obtained by dissolving 5.94 g of  $(\text{NH}_4)_2\text{HPO}_4$  (Sigma-Aldrich, 98%) in 75 ml of distilled water then topping the solution up to 100 ml with distilled water.

## 4.2.3 Other solutions

### 4.2.3.1 Ammonium hydroxide

A 1 M solution of ammonium hydroxide was prepared by the dilution of 11.9 ml of  $\text{NH}_4\text{OH}$  (Riedel-de Haën, 31-33%) in 88.1 ml of distilled water.

## 4.3 Microwave-assisted Synthesis

The adopted microwave-assisted synthesis method discussed in this section is shown schematically in Figure 11.

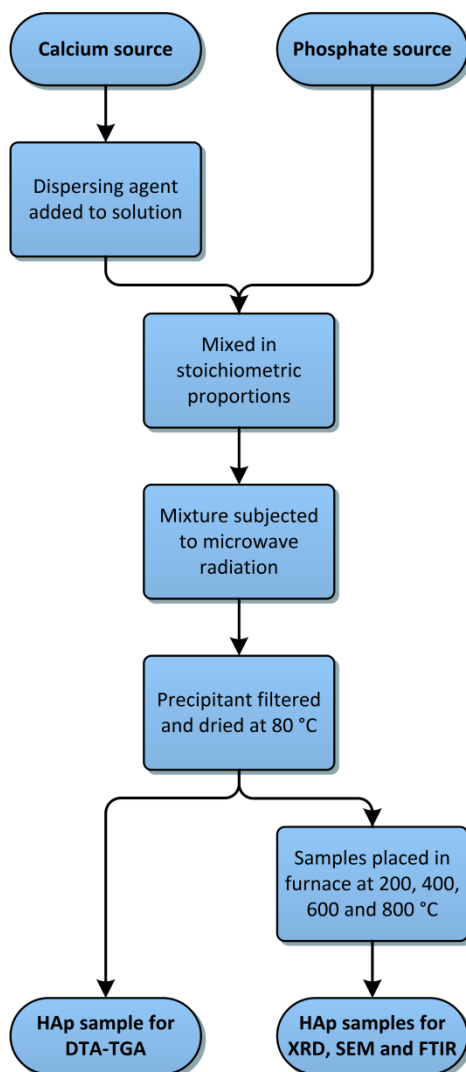


Figure 11: Flowchart for the synthesis of apatites via a microwave-assisted method

### 4.3.1 Experiment 1 (MIC1)

A 50 ml, 0.75 M solution of  $\text{Ca}(\text{OH})_2$  was prepared and 1 ml of Dolapix CE 64 (Zschimmer & Schwarz, 65%) was added as a dispersant. The mixture was stirred whilst 50 ml of 0.45 M  $\text{H}_3\text{PO}_4$  was added dropwise. A household microwave (Sharp R-26ST, 800 W) was used to irradiate the resultant mixture in 10 second pulses at 55% power (440 W), for a total irradiation time of 10 minutes, excluding cooling time. An ice bath was used to cool the mixture to below 50 °C between pulses. The product was filtered and dried on a hotplate at 80 °C.

Small samples were heated sequentially to 200, 400, 600 and 800 °C with a dwell time of 30 minutes, then ground for XRD analysis.

#### 4.3.2 Experiment 2 (MIC2)

A 100 ml, 0.75 M solution of  $\text{Ca}(\text{OH})_2$  was prepared and 1 ml of Dolapix CE 64 (Zschimmer & Schwarz, 65%) was added as a dispersant. The mixture was stirred and 100 ml of 0.45 M  $(\text{NH}_4)_2\text{HPO}_4$  was rapidly added. The resultant mixture was subjected to microwave irradiation in a household microwave (Sharp R-26ST, 800 W) at 55% power (440 W) in 15 second pulses. Between each pulse the mixture was cooled in an ice bath until the temperature decreased to 50 °C. The mixture was irradiated for a total of 10 minutes, not counting the time spent cooling, then filtered and dried on a hotplate at 80 °C.

Small samples were heated sequentially to 200, 400, 600 and 800 °C with a dwell time of 30 minutes, then ground for XRD analysis.

## 4.4 Albumen-mediated Synthesis

The experiments described in this section broadly follow the methodology shown schematically in Figure 12. This methodology was deviated from where experimental conditions necessitated.

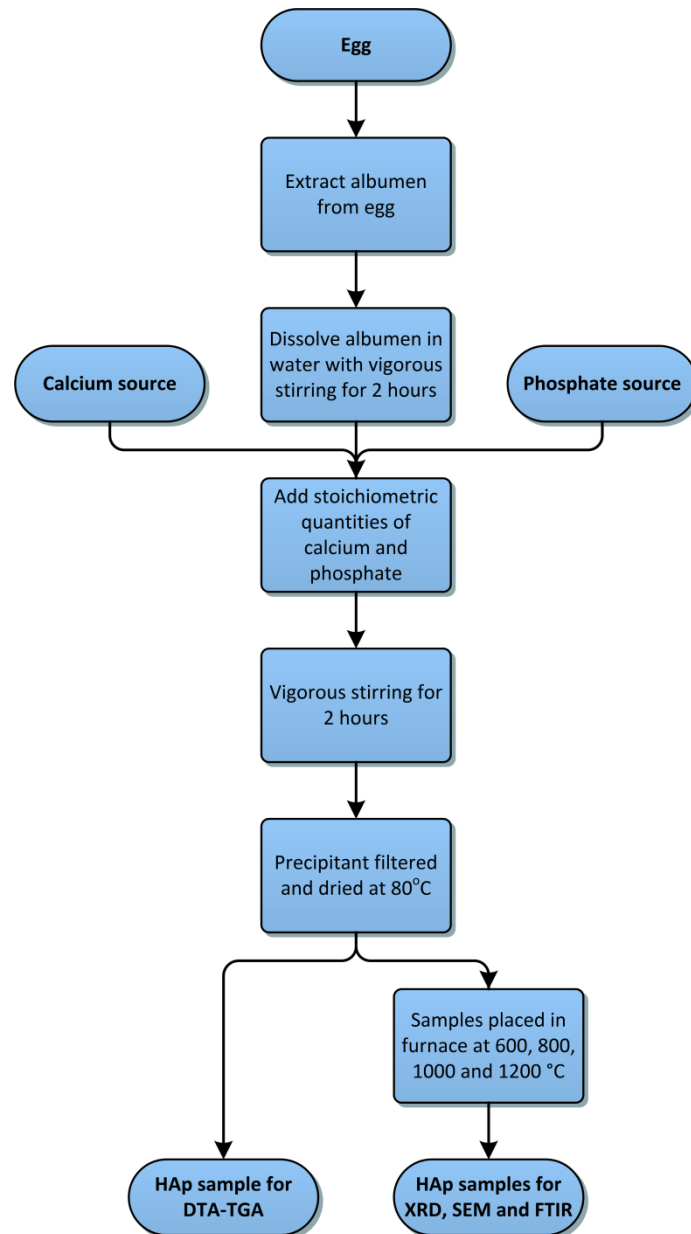


Figure 12: Flowchart for the synthesis of apatite via albumen-mediated synthesis

### 4.4.1 Experiment 1 (ALB1)

Albumen was extracted from 4 large eggs purchased from a local supermarket, with a total albumen volume of approximately 160 ml, and was added to 40 ml of distilled water. The mixture was stirred vigorously for 1 hour.  $\text{Ca}(\text{OH})_2$  was prepared and added to the albumen under constant, vigorous stirring and was left to mix for 1 hour. The albumen was found to have gelled, so phosphoric acid was added rapidly and the gel was broken up. The mixture was placed in a furnace and heated to 450 °C

for 2 hours, in order to burn the gelled protein and allow the reaction to take place. A sample of the charred mixture obtained was taken for thermal analysis, and the remainder was heated at 750 °C for 12 hours. The resultant white solid was ground in an agate mortar and pestle, sintered at 800 °C for 2 hours, and then ground.

Small samples were sintered at 1000 °C and 1200 °C with a dwell time of 2 hours, then ground.

#### 4.4.2 Experiment 2 (ALB2)

160 ml of albumen was added to 40 ml of distilled water and stirred vigorously until a homogenous solution was obtained.  $\text{Ca}(\text{OH})_2$  and  $\text{H}_3\text{PO}_4$  were added simultaneously. The solution was determined to be highly basic, with a pH around 12. A milky yellow-white mixture was obtained.

The solution was aged overnight, and subsequently dried in an oven at 80 °C. A glassy orange substance was produced with white inclusions nearer to the base of the beaker.

The dried product was heated to 400 °C for 2 hours, resulting in a blue substance. The product was then ground and further heated to 600 °C for 2 hours. To remove the remaining carbon, the sample was heated to 800 °C for 2 hours, and finally ground in an agate mortar.

Small samples were sintered at 1000 °C and 1200 °C with a dwell time of 2 hours, then ground.

#### 4.4.3 Experiment 3 (ALB3)

160 ml of freshly extracted albumen was added to 40 ml of distilled water and stirred vigorously until a homogeneous solution was obtained. Calcium acetate and ammonium dihydrogen phosphate were added simultaneously. The pH was found to be neutral, so 100 ml of 1 M ammonium hydroxide solution was added in order to increase the pH to approximately 12. Upon addition of the ammonium hydroxide, the formation of fine white particles was observed.

The mixture was aged for 24 hours, diluted with approximately one litre of water, then aged for a further 18 hours. The mixture was filtered and both the residue and filtrate were dried at 80 °C. The filtrate started as a colourless solution and dried to form a reddish-brown glassy substance, whilst the residue started as a fine, soft, pale yellow substance which dried to form a similarly fine, yellow solid.

To completely burn off the protein, the residue was heated sequentially to 500, 600 and 700 °C with a dwell time of 1 hour, then sintered at 800 °C for 2 hours. The residue was ground between heating at each temperature and after sintering.

Small samples were sintered at 1000 °C and 1200 °C with a dwell time of 2 hours, then ground.

## 4.5 Characterisation

### 4.5.1 SEM

#### 4.5.1.1 For Eggshell and ESM

A Philips XL30 ESEM operated variously at 15 and 25 kV was used to image samples of eggshell and eggshell membrane. A working distance of 8.5-11 mm was maintained.

#### 4.5.1.2 For ALB1, ALB2 and ALB3

Silver paint was used to adhere the powdered samples to SEM stubs and the excess was removed by tapping the sample with a metal spatula. Samples were then coated with two thin layers of gold using an Agar Auto Sputter Coater.

A Zeiss Sigma FE-SEM operated variously at 10 and 15 kV was used to image the samples. An aperture of 30  $\mu\text{m}$  and working distance of 9-10 mm were used. Some of the produced micrographs were enhanced using the GNU Image Manipulation Program by shifting the mid-grey values such that the main features became more visible; care was taken to not distort the images or introduce artefacts.

### 4.5.2 XRD

#### 4.5.2.1 For MIC1 and MIC2

XRD was conducted using a Philips PW1830 with a copper target ( $\lambda = 1.54056 \text{ \AA}$ ). A voltage of 40 kV was used at a current of 30 mA to examine a range of 20° to 70° with a step size of 0.02° and a step time of 5 seconds.

#### 4.5.2.2 For ALB1, ALB2 and ALB3

XRD was conducted using a PANalytical Empyrean with a cobalt target ( $\lambda = 1.78901 \text{ \AA}$ ). A voltage of 40 kV was used with a current of 40 mA. The sample was rotated at a rate of 1 rotation every 2 seconds whilst a range of 10° to 80° was investigated with a step size of 0.013°. The background radiation was removed from the data using X'Pert Highscore Plus.

### 4.5.3 DTA-TGA

#### 4.5.3.1 For Eggshell and MIC1

A Stanton Redcroft STA1500 was utilised with a step size of 20 °C per minute, up to a maximum temperature of 1300 °C in an alumina crucible.

#### 4.5.3.2 *For ALB1, ALB2 and ALB3*

A Mettler Toledo TGA/DSC 1 STARe System was used from 30 °C to 1500 °C in an alumina crucible at a heating rate of 10 °C per minute. Data was recorded with a step size of 0.167 °C.

#### 4.5.4 FTIR

FTIR was conducted using a Perkin-Elmer Spectrum One FTIR Spectrometer. A range of 4000 to 650  $\text{cm}^{-1}$  was investigated at a resolution of 4  $\text{cm}^{-1}$ .

# Chapter 5: Results and Analysis

*This chapter presents the results obtained, along with quantitative and qualitative analyses. Explanations are given for the produced results with cross-referencing to the results of other forms of characterisation.*

## 5.1 Eggshell

### 5.1.1 SEM

The thickness of the eggshell can be seen to be 300  $\mu\text{m}$ . The columnar structure of the calcite crystals present in mammillary layer of the eggshell can clearly be seen in Figure 13. These crystals have a typical diameter of 50  $\mu\text{m}$  and can only be seen in the upper portion of the image, which corresponds to the internal surface of the eggshell. Columnar structures cannot be seen in the palisade layer, shown in the lower half of Figure 13, which suggests that the columnar structures have fused as they have grown outwards. Figure 14 demonstrates that crystal sizes in the palisade region are small, typically less than 5  $\mu\text{m}$ , with an irregular plate-like morphology and further shows that these are connected in a layered fashion with a degree of nanoporosity.

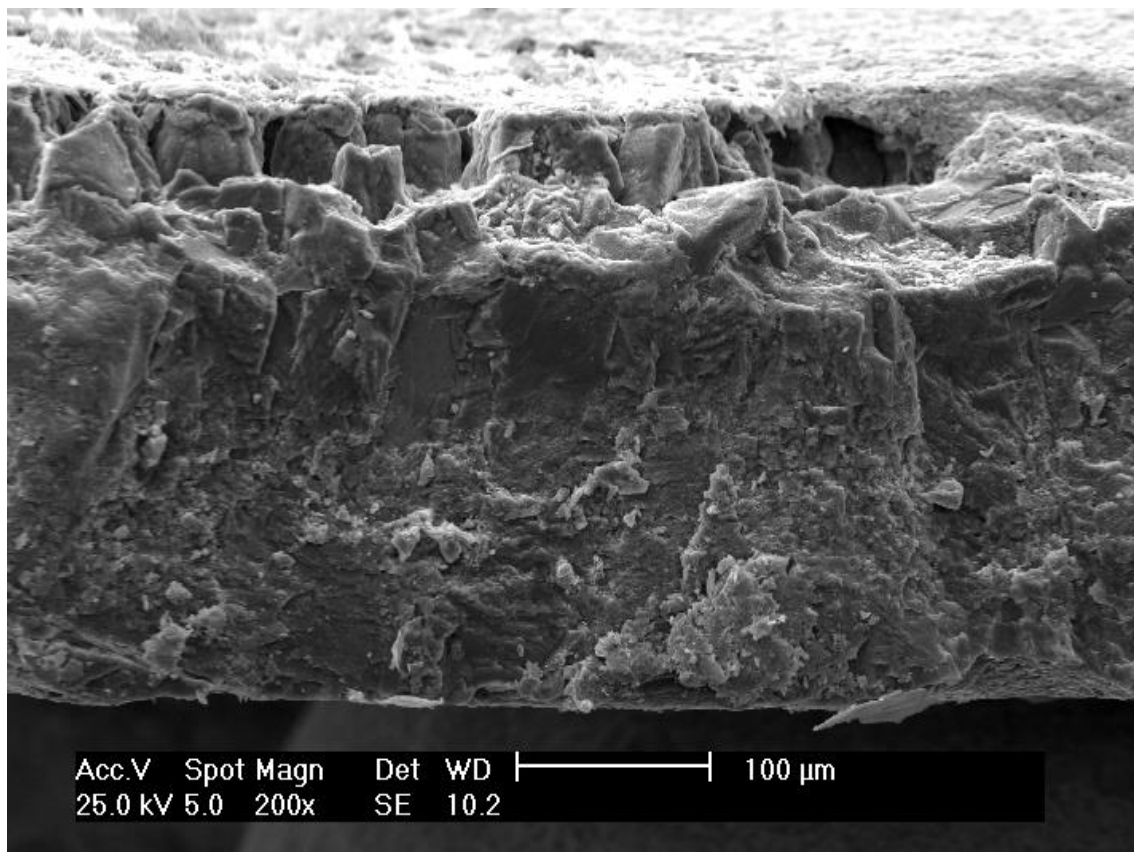


Figure 13: SEM micrograph of the edge of an eggshell, with the outside in the lower portion of the image

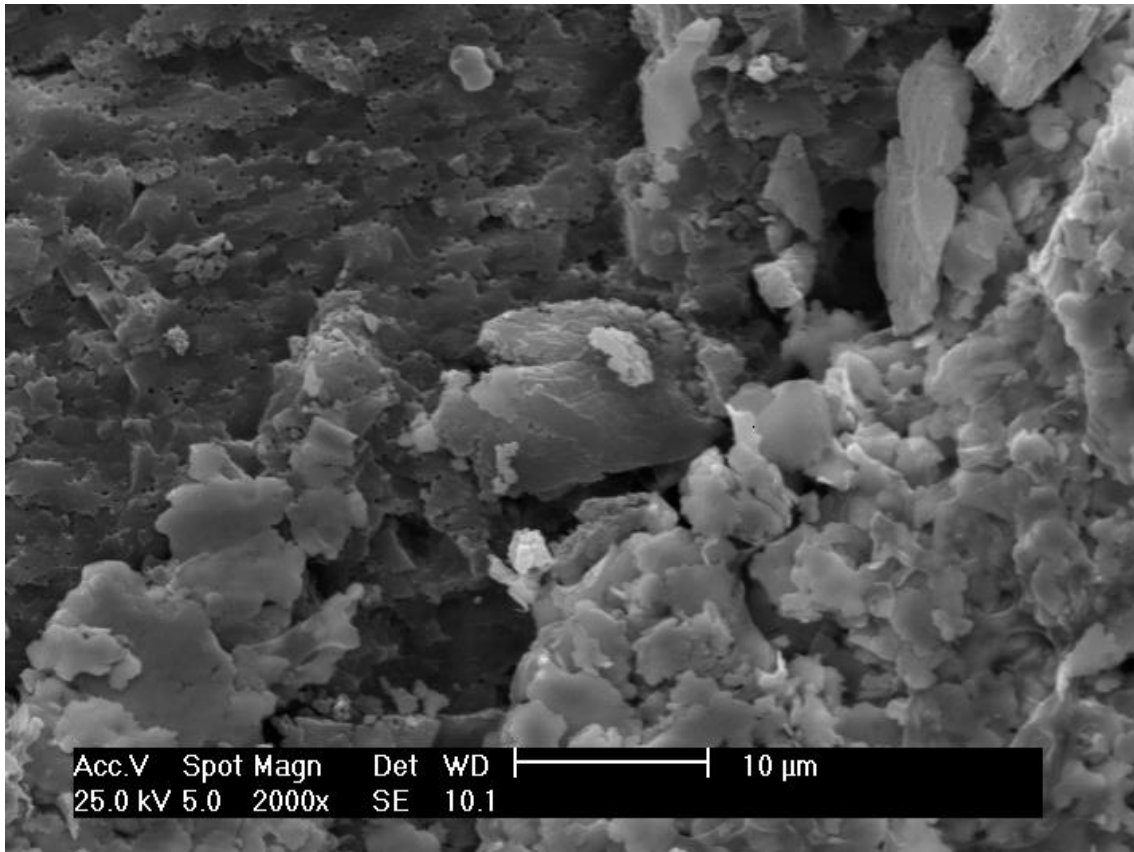


Figure 14: SEM micrograph of the edge of an eggshell fragment

The outer eggshell membrane is shown in Figure 15. It can be seen that the membrane is formed from highly connected fibres with a diameter of 2-5  $\mu\text{m}$  in an open pore structure. Pore sizes range from 5  $\mu\text{m}$  to 20  $\mu\text{m}$ . Crystal structures with diameters less than 20  $\mu\text{m}$  appear to be encapsulated within parts of the protein matrix.

The inner eggshell membrane, shown in Figure 16, can be seen to have a very different structure compared to the outer eggshell membrane, shown in Figure 15. It can be seen that the inner ESM is more densely packed and consists of fibres with diameters of 1-2  $\mu\text{m}$ , which is less than the 2-5  $\mu\text{m}$  of the outer ESM.

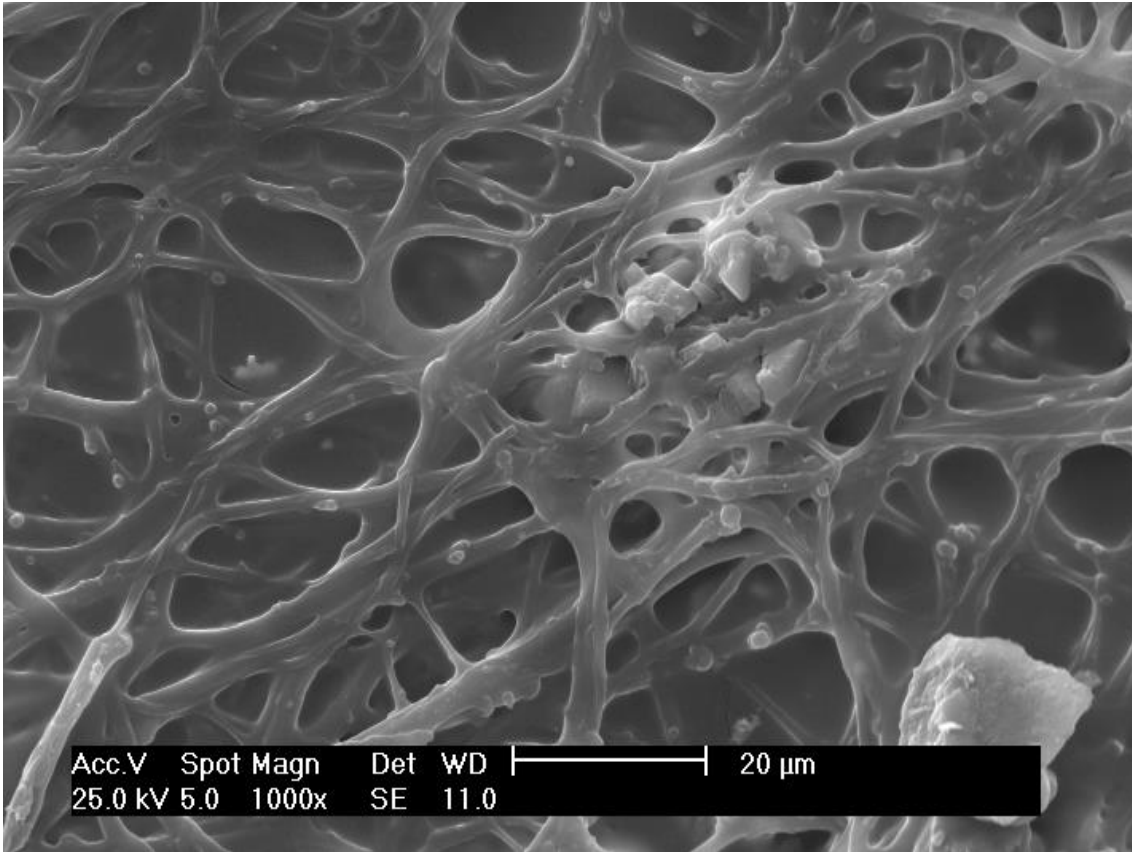


Figure 15: SEM micrograph of the outer eggshell membrane

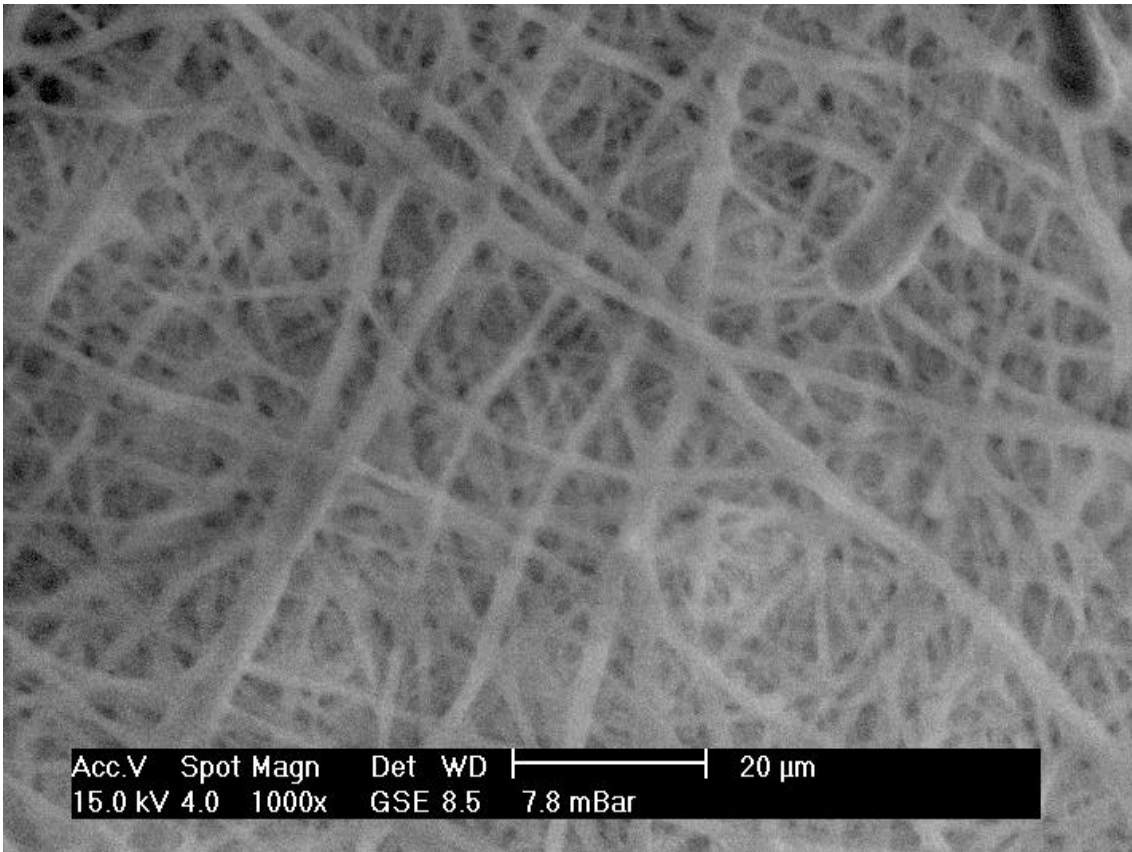


Figure 16: SEM micrograph of the inner eggshell membrane

### 5.1.2 DTA-TGA

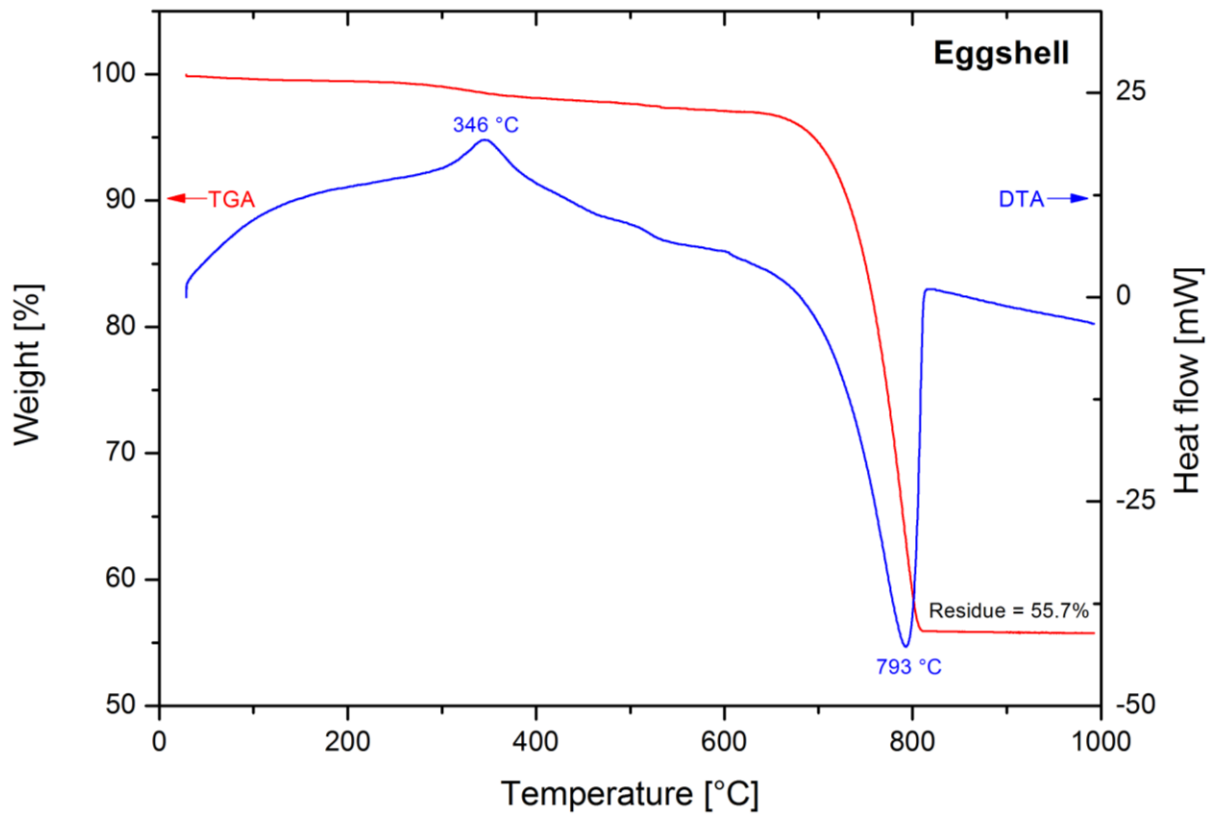


Figure 17: DTA-TGA curves for eggshell with the membrane removed

The exotherm at 346 °C is accompanied by a very small mass loss and can be attributed to the combustion of the eggshell matrix proteins.

At 793 °C, an endothermic peak occurs with a corresponding mass loss of more than 40%; this peak represents the calcination of calcium carbonate into calcium oxide as well as the calcination of a small amount of magnesium carbonate present in the eggshell. Mass is lost in the form of evolved carbon dioxide, although this was not confirmed experimentally.

## 5.2 Microwave-assisted Synthesis

### 5.2.1 Experiment 1 (MIC1)

#### 5.2.1.1 XRD

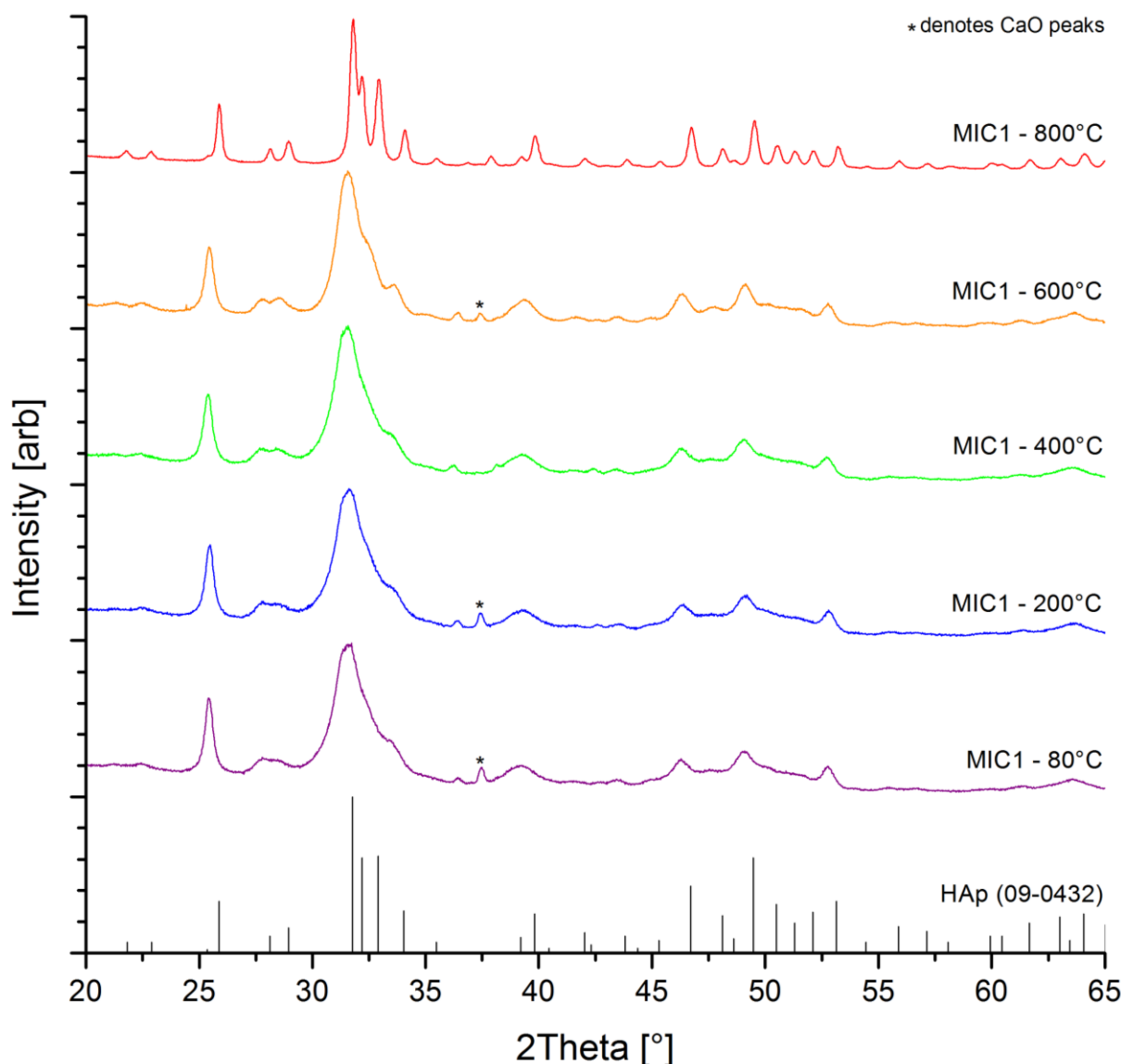


Figure 18: XRD spectra for MIC1 samples dried at 80 °C and sintered at 200, 400, 600 and 800 °C

As can be seen in Figure 18, the XRD spectra of all samples are consistent with the standard spectrum for HAp. Small peaks can be seen in most of the spectra indicating the presence of unreacted calcium oxide. The compositions of the MIC1 samples are given in Table 6, and show that CaO represents 10% of the sample both after drying at 80 °C and sintering at 200 °C, but this is reduced in the samples heated to higher temperatures to a large extent, with a 0 %, 4.8% and 0% content of CaO corresponding to sintering temperatures of 400, 600 and 800 °C, respectively. The maximum CaO peak ( $\approx 37.5^\circ$ ) is indistinguishable from background noise in the samples sintered at 400 °C and 800 °C.

Table 6: Phase analysis of MIC1 samples at different temperatures expressed as a percentage

	80 °C	200 °C	400 °C	600 °C	800 °C
<b>HAp</b>	89.7	89.9	100.0	95.2	100.0
<b>CaO</b>	10.3	10.1	0.0	4.8	0

Crystallite sizes remained largely unchanged by temperatures up to 600 °C and were typically found to be 19 nm for this region, as shown in Table 7. Sintering at 800 °C increases the crystallite size to around 30 nm, leading to a substantial change in the peak broadening shown in Figure 18.

Table 7: Estimated crystallite sizes for MIC1 dried at 80 °C and sintered at 200, 400, 600 and 800 °C

Temperature (°C)	Peak position (2 $\theta$ °)	FWHM (2 $\theta$ °)	Crystallite size (nm)
<b>80</b>	25.44	0.42	<b>19.4</b>
<b>200</b>	25.47	0.43	<b>18.9</b>
<b>400</b>	25.40	0.45	<b>18.1</b>
<b>600</b>	25.45	0.45	<b>18.1</b>
<b>800</b>	25.89	0.27	<b>30.2</b>

## 5.2.1.2 DTA-TGA

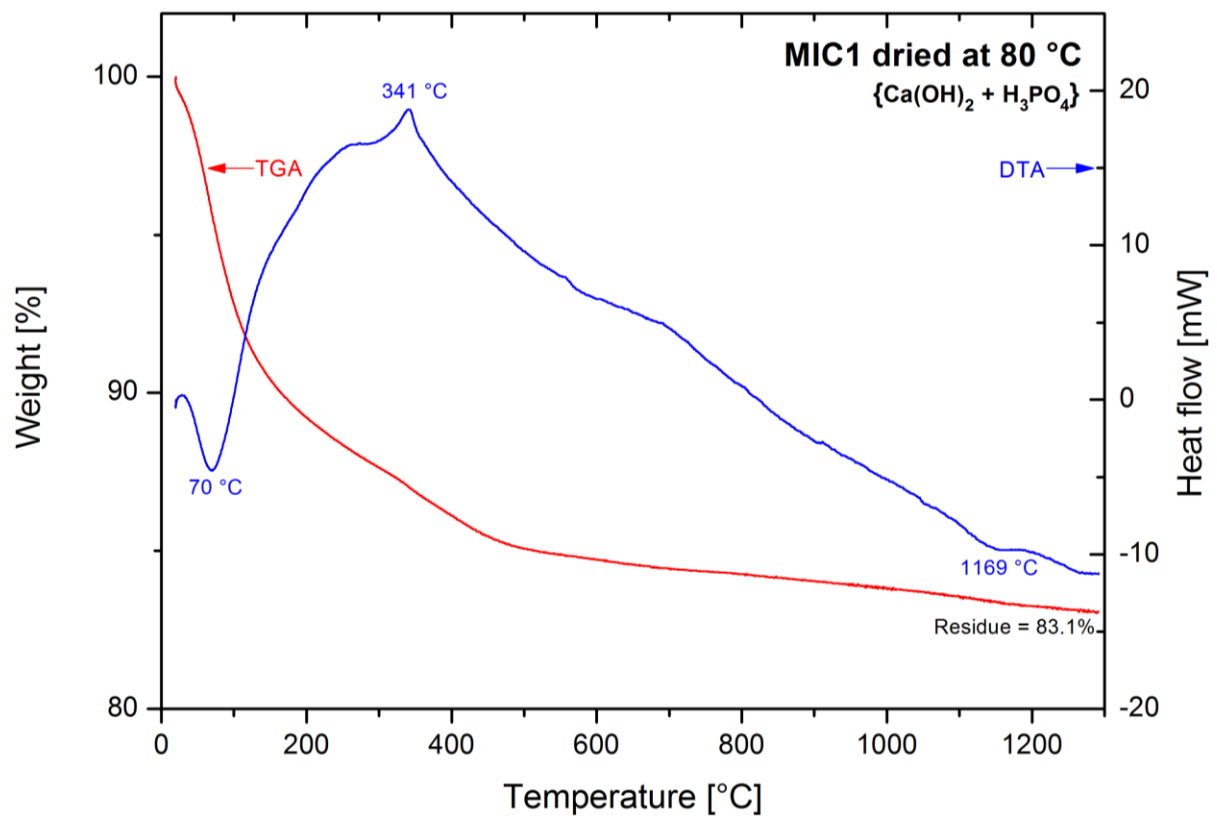


Figure 19: DTA-TGA curves for MIC1 dried at 80 °C

The loss of absorbed water is demonstrated by the endothermic peak at 70 °C with a corresponding mass loss of more than 5%.

An exotherm can be seen at 341 °C and is accompanied by relatively large mass loss of more than 5%. This suggests that a significant quantity of the dispersant (Dolapix 64) was present in the samples, even after filtration and drying.

The endotherm at 1169 °C indicates a phase change, and is believed to be that of HAp into  $\beta$ -TCP.

## 5.2.2 Experiment 2 (MIC2)

### 5.2.2.1 XRD

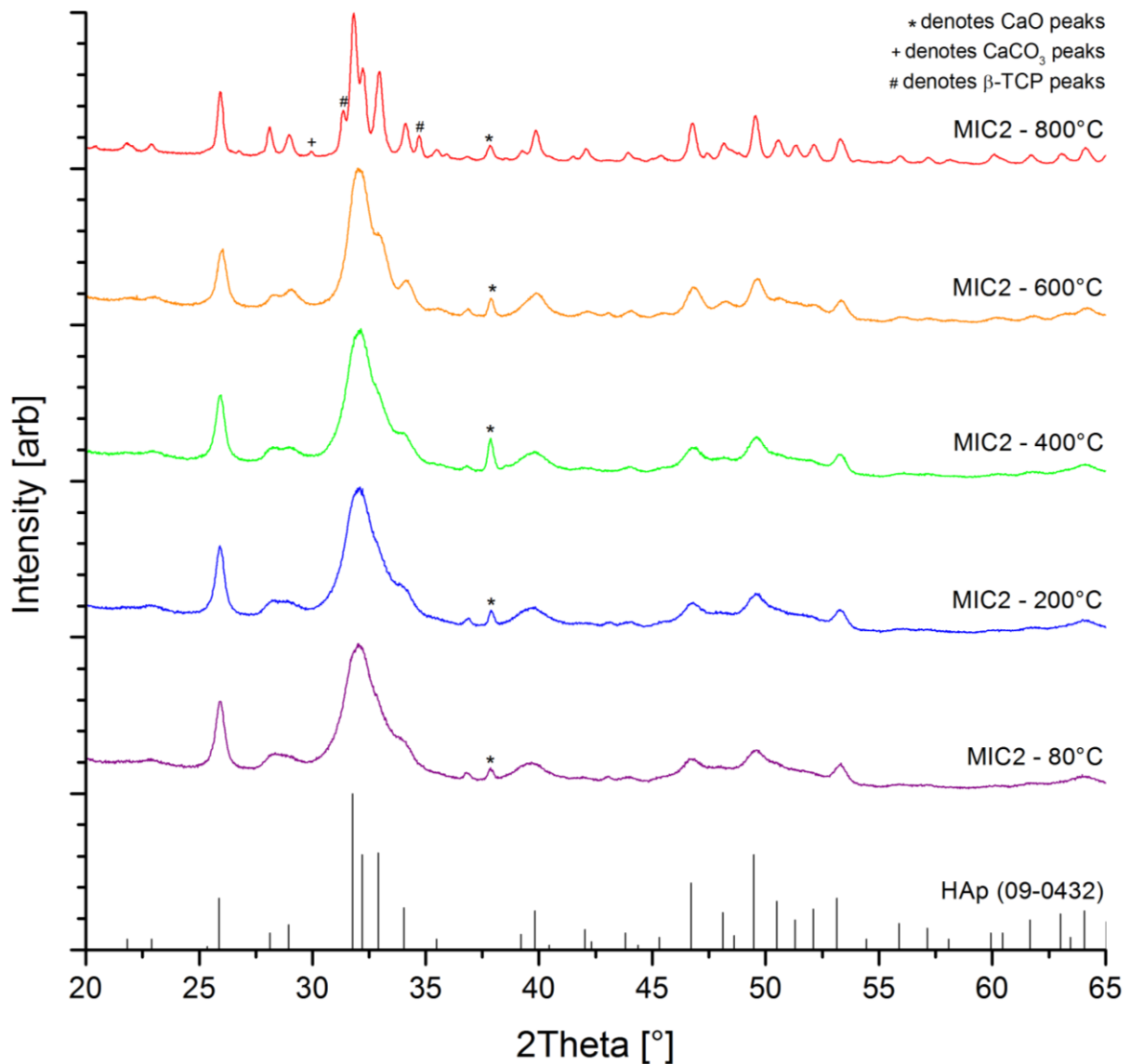


Figure 20: XRD spectra for MIC2 samples dried at 80 °C and sintered at 200, 400, 600 and 800 °C

Figure 20 shows that the XRD spectra for samples of MIC2 heated to temperatures up to 600 °C are all consistent with HAp containing a small calcium oxide impurity, with samples typically being composed of 90% HAp and 10% CaO, as shown in Table 8. The changes in the proportion of CaO seen in Table 8 for sintering temperatures up to 600 °C are expected to be erroneous, as the pattern of changes seen is not likely to occur; particularly in the case of the sample sintered at 400 °C, which suggests that the proportion of CaO in the sample doubled, then returned to 10% in the sample heated to 600 °C.

For the sample heated to 800 °C, it was found that approximately 29% of the HAp had decomposed into  $\beta$ -TCP. Some calcium carbonate was also seen in this sample. The estimated composition is given in Table 8.

**Table 8: Phase analysis of MIC2 samples at different temperatures expressed as a percentage**

	80 °C	200 °C	400 °C	600 °C	800 °C
<b>HAp</b>	92.5	90.0	81.2	88.9	61.5
<b>CaO</b>	7.5	10.0	18.8	11.1	5.9
<b>CaCO<sub>3</sub></b>	0.0	0.0	0.0	0.0	7.4
<b><math>\beta</math>-TCP</b>	0.0	0.0	0.0	0.0	25.1

A significant amount of peak broadening can clearly be seen in Figure 20. It can also be seen that there is little change in crystallinity for sintering at temperatures up to 600 °C; quantitative analysis, given in Table 9, supports this, indicating a crystallite size of approximately 17 nm. For the sample heated to 800 °C, the crystallite size was shown to have increased to around 27 nm.

**Table 9: Estimated crystallite sizes for MIC2 dried at 80 °C and sintered at 200, 400, 600 and 800 °C**

Temperature (°C)	Peak position (2 $\theta$ °)	FWHM (2 $\theta$ °)	Crystallite size (nm)
<b>80</b>	25.93	0.47	<b>17.3</b>
<b>200</b>	25.92	0.45	<b>18.1</b>
<b>400</b>	25.94	0.47	<b>17.3</b>
<b>600</b>	26.00	0.50	<b>16.3</b>
<b>800</b>	25.94	0.30	<b>27.2</b>

## 5.3 Albumen-mediated Synthesis

### 5.3.1 Experiment 1 (ALB1)

#### 5.3.1.1 SEM

At low magnifications, it can be seen that the sample includes particles with very varied size and morphology. Figure 21 demonstrates the presence of large plate-like structures 100-300  $\mu\text{m}$  across, along with smaller particles with sizes of the order of 10  $\mu\text{m}$ . The white areas present in the image indicate that a charge was built up on the surface.

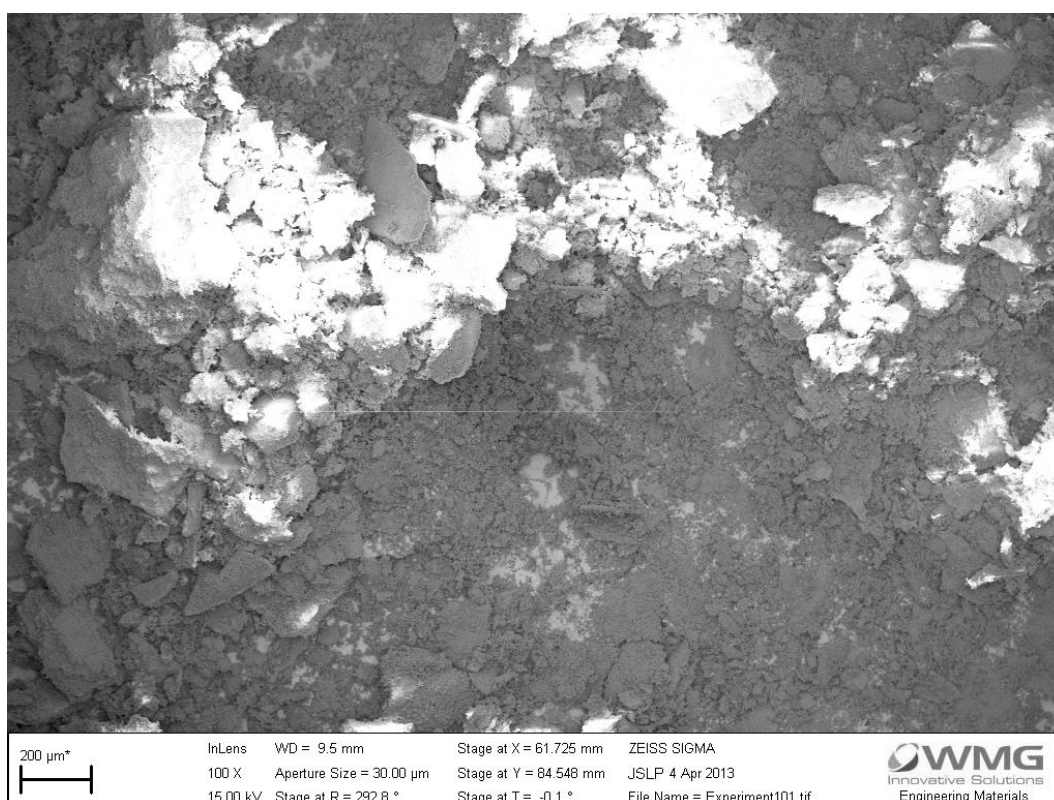


**Figure 21: SEM micrograph of ALB1 sintered at 800 °C**

Figure 22 shows that the large structures contain micropores and at higher magnifications, such as in Figure 23, it can be seen that these larger structures are formed from microcrystals of varying sizes which have been fused together at a high temperature (800 °C).

The irregularly shaped plate-like crystals, with a length and width less than 20  $\mu\text{m}$ , shown in Figure 23 are unlikely to be hydroxyapatite as the morphology is atypical of apatitic crystal structures. It is possible that these structures are unreacted calcium oxide, the presence of which is indicated in the XRD spectra presented in §5.3.1.2 (Figure 26). Similar structures can be seen in Figure 24.

Figure 24 shows that the sample is composed of some particles with a near-spherical morphology and a diameter of 1-2.5  $\mu\text{m}$ , as well as rods with similar diameters and lengths of 4-6  $\mu\text{m}$ . Smaller,

near-spherical particles with diameters of the order of 500 nm can be seen in Figure 25, although these are present only in very small quantities.

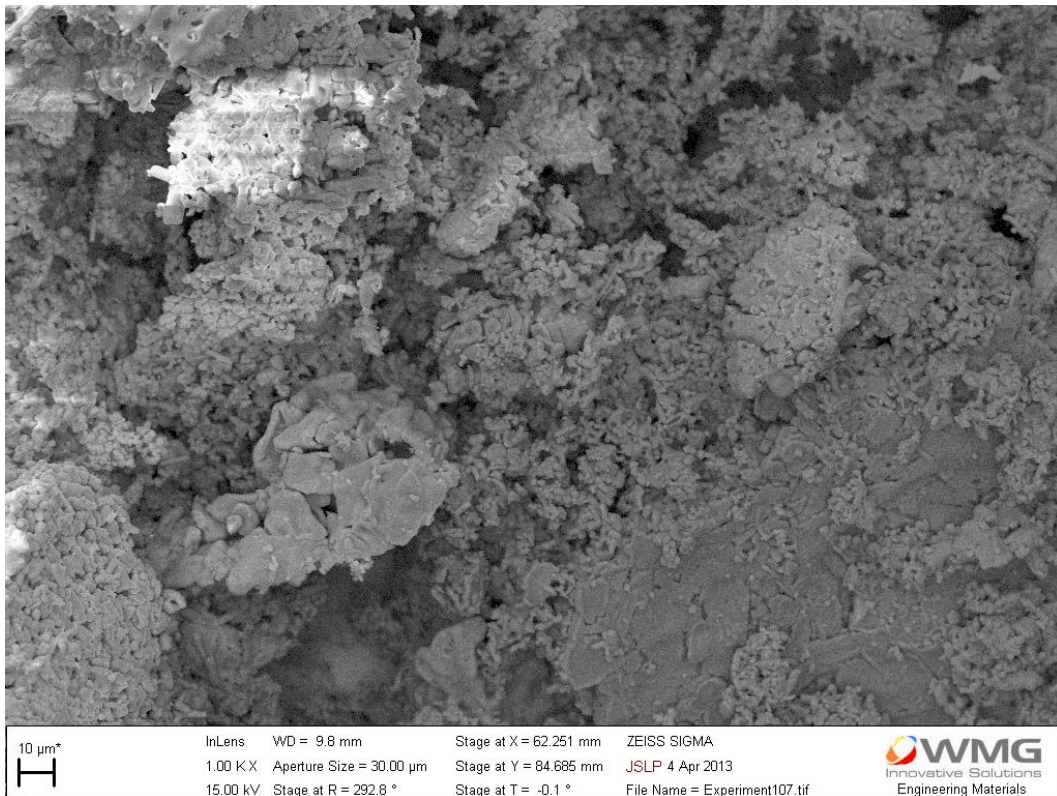


Figure 22: SEM micrograph of ALB1 sintered at 800 °C

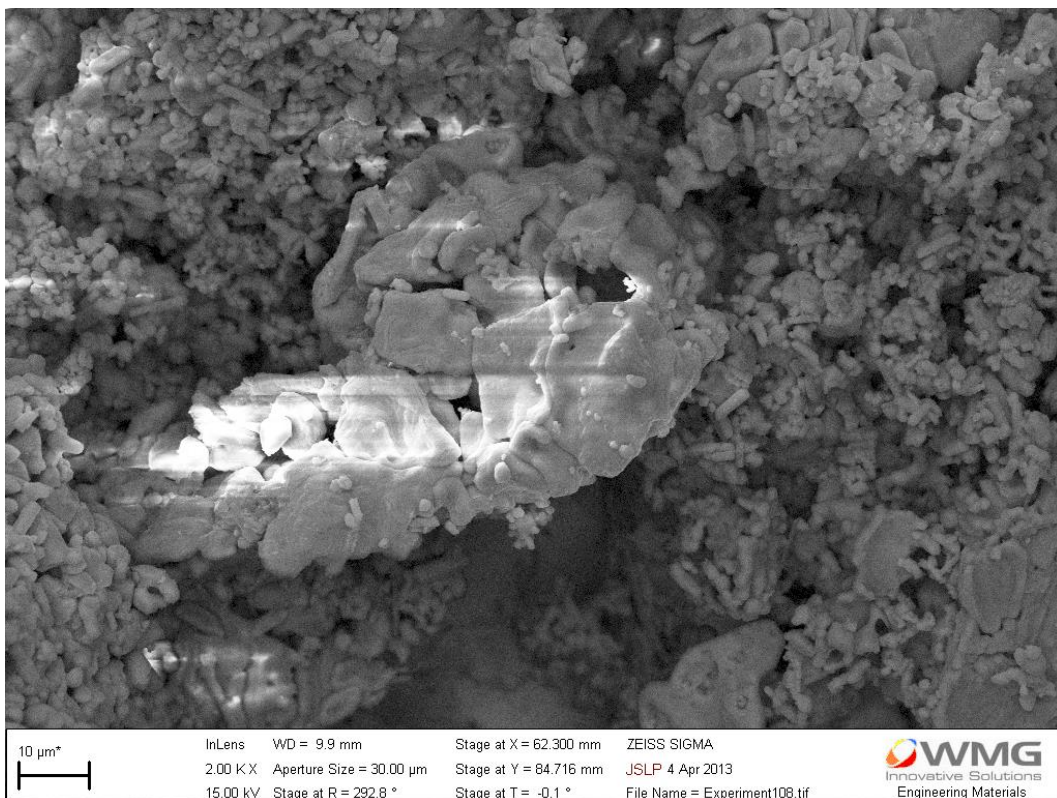


Figure 23: SEM micrograph of ALB1 sintered at 800 °C

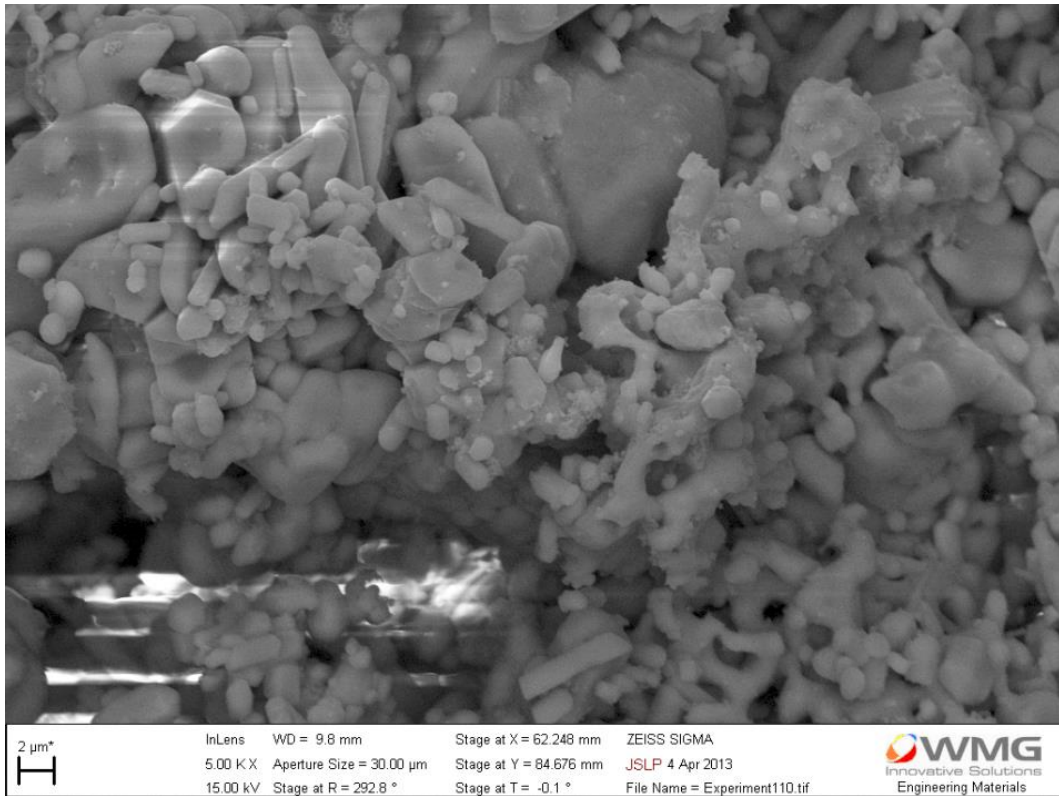


Figure 24: SEM micrograph of ALB1 sintered at 800 °C

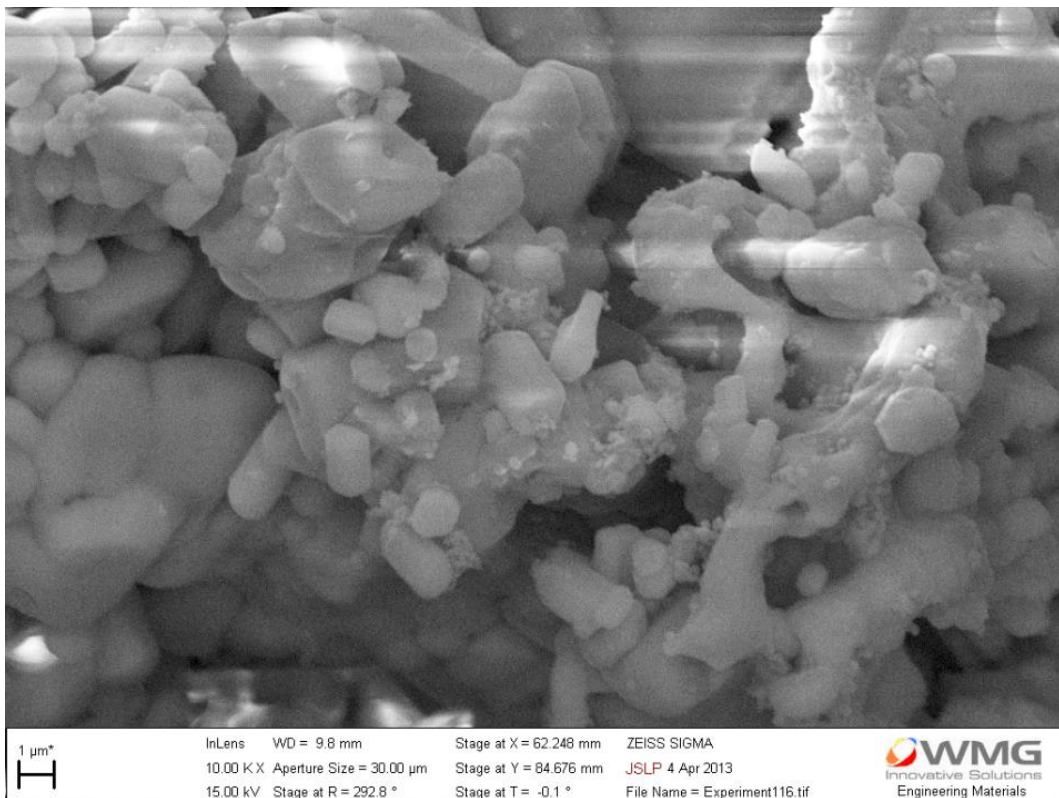


Figure 25: SEM micrograph of ALB1 sintered at 800 °C

## 5.3.1.2 XRD

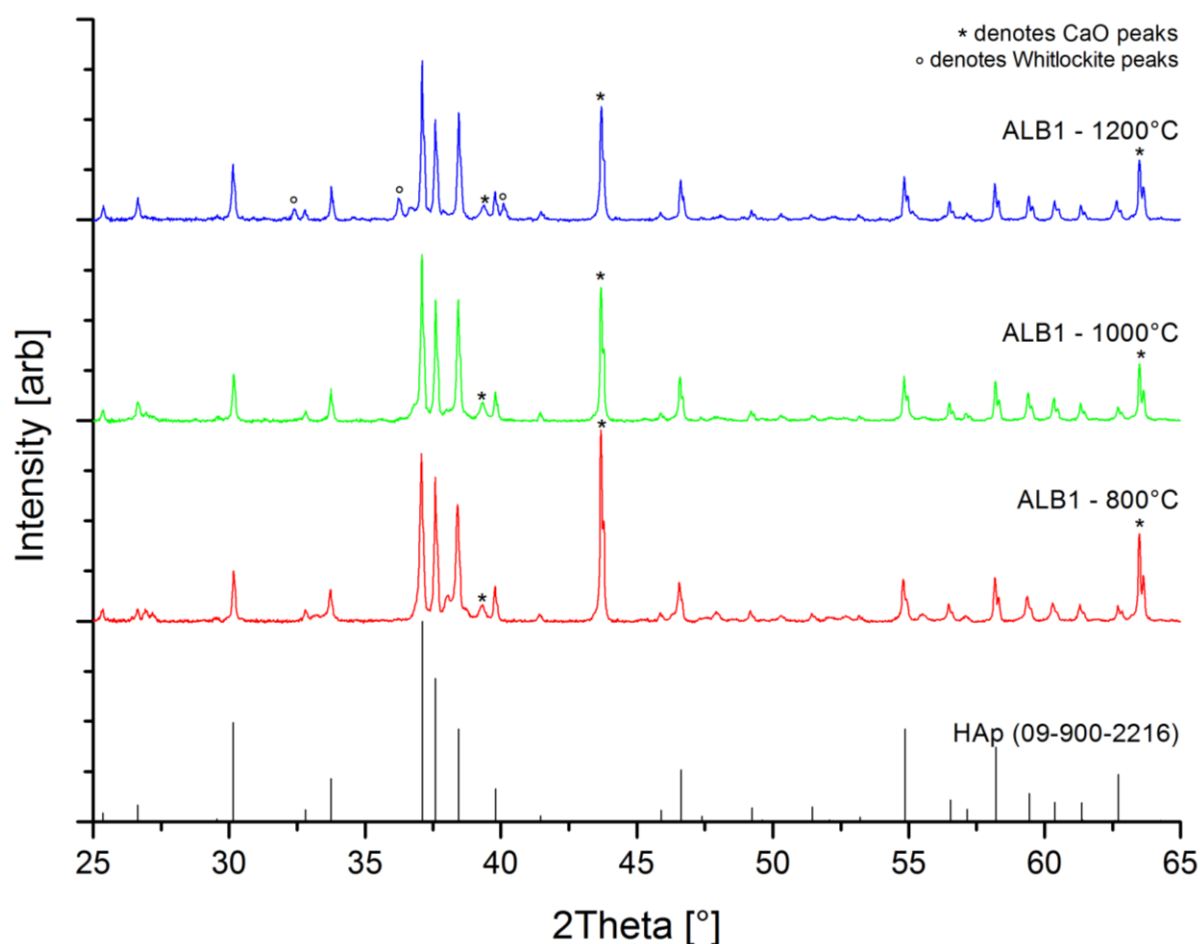


Figure 26: XRD spectra for ALB1 samples sintered at 800, 1000 and 1200 °C

Figure 26 shows that the peaks for ALB1 sintered to 800 °C and 1000 °C were consistent with HAp, except for the presence of calcium oxide. It can also be seen that in the sample sintered to 1200 °C, there has been a partial decomposition of HAp into Whitlockite with a nominal composition of  $\text{Ca}_{60.69}\text{Mg}_{2.31}\text{P}_{42.00}\text{O}_{168.00}$ , although the exact composition of the produced Whitlockite phase cannot be determined from XRD alone. Decomposition of HAp into magnesium containing Whitlockite indicates that magnesium from the eggshell has been incorporated into the produced apatite. The calculated proportions of each phase shown in Figure 26 are given in Table 10. Excluding the CaO phase, the sample of ALB1 sintered at 1200 °C was composed of approximately 88% HAp and 12% Whitlockite.

Table 10: Phase analysis of ALB1 samples at different temperatures expressed as a percentage

	800 °C	1000 °C	1200 °C
CaO	53.0	44.6	38.5
HAp	47.0	55.4	54.0
Whitlockite	0.0	0.0	7.4

The variation in the calculated proportion of calcium oxide content is indicative of the approximate nature of this type of analysis.

Numerical analysis is displayed in Table 11 and indicates a crystallite size of around 175 nm for the sample sintered at 800 °C. Comparison of this value to the particle sizes of 1-2 µm seen in the SEM images presented in §5.3.1.1 suggests that the particles contain many crystal imperfections, with ordered regions with diameters of approximately 175 nm. Little change in crystallinity is observed for samples sintered at 800, 1000 and 1200 °C, with estimated crystallite sizes increasing by approximately 20% upon sintering to 1000 °C compared to 800 °C, and no significant change of crystallite size for sintering at 1200 °C compared to 1000 °C.

**Table 11: Crystallite sizes for ALB1 estimated using the Scherrer equation**

Peak position	FWHM (2θ °)			Crystallite size (nm)		
	800 °C	1000 °C	1200 °C	800 °C	1000 °C	1200 °C
<b>30.2</b>	0.0640	0.0640	0.1023	166.7	166.7	104.3
<b>37.1</b>	0.0768	0.0640	0.0512	150.5	180.7	225.9
<b>38.4</b>	0.0640	0.0640	0.0640	183.9	184.0	184.0
<b>46.6</b>	0.1279	0.0768	0.0768	104.9	174.8	174.9
<b>54.8</b>	0.0768	0.0640	0.0640	208.4	250.3	250.3
<b>58.2</b>	0.0768	0.0640	0.0768	227.8	273.5	227.8
			<b>Mean</b>	<b>173.7</b>	<b>205.0</b>	<b>194.5</b>
			<b>Standard Deviation</b>	<b>48.7</b>	<b>45.8</b>	<b>31.9</b>

## 5.3.1.3 DTA-TGA

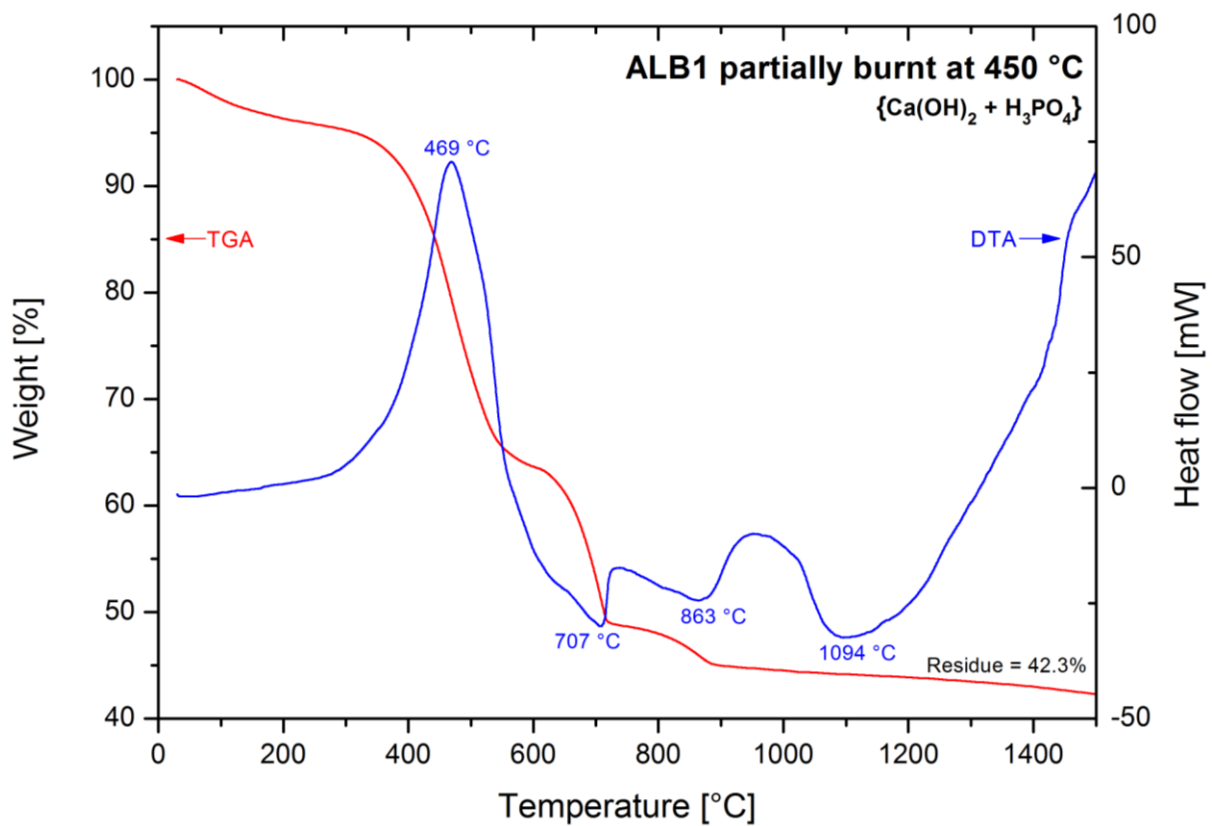


Figure 27: DTA-TGA curves for a sample of ALB1 taken after heating to 450 °C

The initial small mass loss shown in Figure 27 can be attributed to the loss of absorbed water.

An exothermic peak at 469 °C corresponds to the combustion of remaining carbonaceous material which was not previously burnt off by heating to 450 °C.

At 707 °C the calcium carbonate content of the sample is calcined into calcium oxide, with a corresponding loss of mass.

Another endotherm at 863 °C is believed to relate to the calcination of magnesium carbonate, as this is expected to occur at a higher temperature than the calcination of calcium carbonate. This further confirms the presence of magnesium in the eggshell precursor.

The endotherm at 1094 °C is attributable to the conversion of HAp to Whitlockite and is consistent with the change observed in the XRD spectra for ALB1 samples sintered at 1000 °C and 1200 °C.

## 5.3.1.4 FTIR

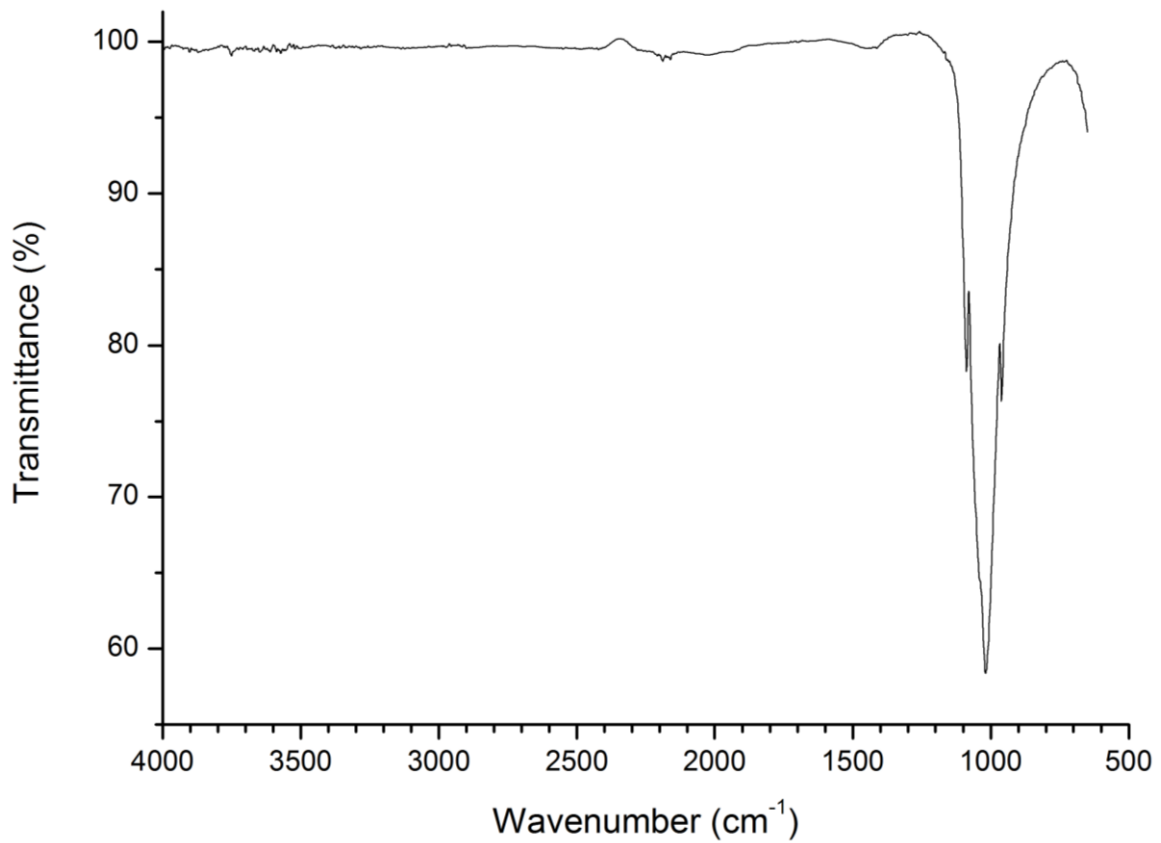


Figure 28: FTIR spectrum for ALB1 sintered at 800 °C

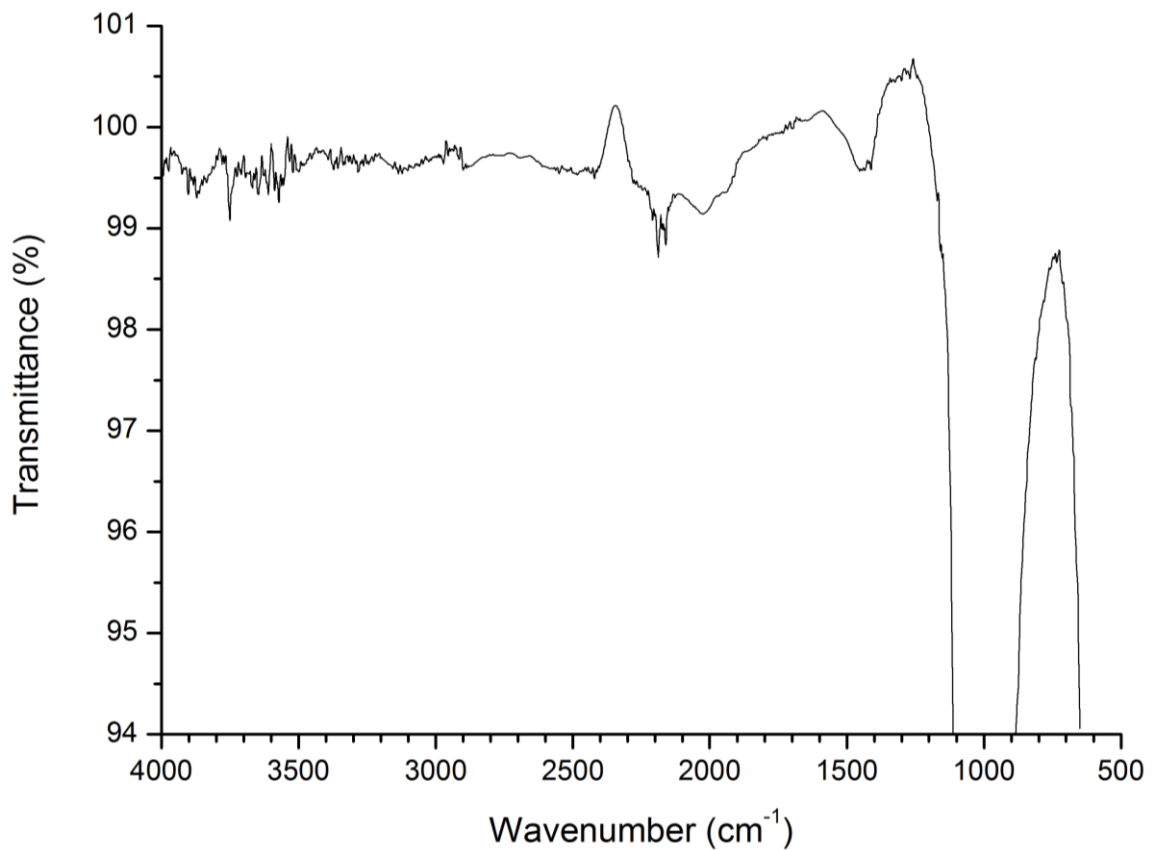


Figure 29: FTIR spectrum for ALB1 sintered at 800 °C for a limited range of transmittance values

The FTIR spectrum for ALB1, given in Figure 28, shows large peaks at  $1019\text{ cm}^{-1}$  and  $961\text{ cm}^{-1}$ , indicating the presence of phosphate groups, with the  $1019\text{ cm}^{-1}$  peak potentially indicating the presence of hydrogen phosphate ions ( $\text{HPO}_4^{2-}$ ). The peak at  $1088\text{ cm}^{-1}$  can represent either  $\text{HPO}_4^{2-}$  or carbonate.

Due to the large size of dominant peaks, little can be seen of the other peaks, and so Figure 29 presents the spectrum for a limited range of transmittances. Peaks at  $1412\text{ cm}^{-1}$  and  $1453\text{ cm}^{-1}$  indicate carbonate content. Due to the presence of calcium oxide in the sample, indicated by the XRD spectra presented in §5.3.1.2 (Figure 26), it is considered to be highly likely that the carbonate peaks are indicating the presence of calcium carbonate within the sample rather than the presence of CHAp.

A small peak corresponding to the presence of  $\text{HPO}_4^{2-}$  is observable at  $2438\text{ cm}^{-1}$ . Other small peaks indicate the presence of  $\text{OH}^-$  ( $3572\text{ cm}^{-1}$ ) and absorbed water ( $3741\text{ cm}^{-1}$ ).

## 5.3.2 Experiment 2 (ALB2)

### 5.3.2.1 SEM

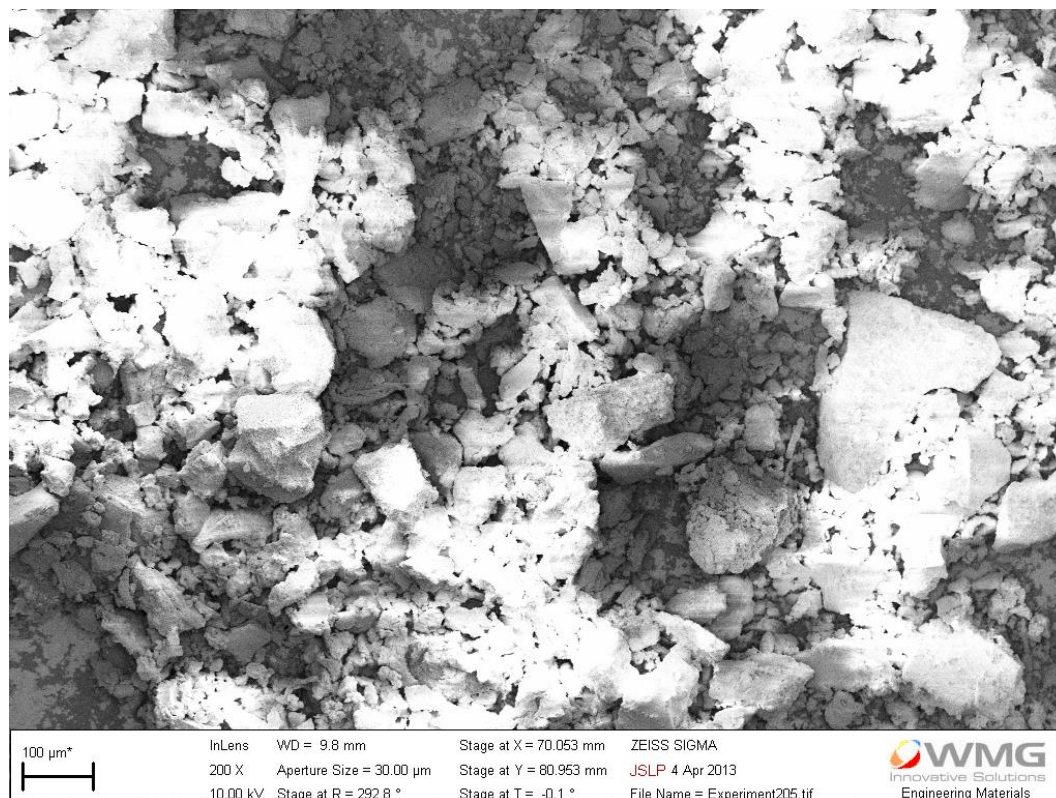


Figure 30: SEM micrograph of ALB2 sintered at 800  $^\circ\text{C}$

Figure 30 shows a large variation in particle size and morphology in the sample. Most of the large particles are irregularly shaped with diameters of 100-200  $\mu\text{m}$ , but some particles can be seen with plate-like morphologies 50-200  $\mu\text{m}$  across and others can be seen with sizes down to below 10  $\mu\text{m}$ .

In Figure 31 and Figure 32 it can be seen that the surfaces of the large particles are not smooth; Figure 33 shows that this rough surface texture consists mainly of rod-shaped particles. The nanorods typically have a diameter of 100-300 nm and a length of 1-2  $\mu\text{m}$  and are fused together to form the larger particles previously described. The predominance of nanorods suggests that the pH may not have been maintained above 12 during synthesis, but the result is consistent with a high pH around 11.

The hexagonal plate-like structures visible in Figure 34 are atypical of hydroxyapatite and may be indicative of the presence of very small impurity. This may be  $\beta$ -TCP, which has been shown to have the potential for hexagonal plate-like structures [87], or may be Whitlockite, which has a similar crystal structure to  $\beta$ -TCP and has been demonstrated to be present in small quantities in a sample sintered at 1200  $^\circ\text{C}$ , and could be present in a very small quantity at lower temperatures.

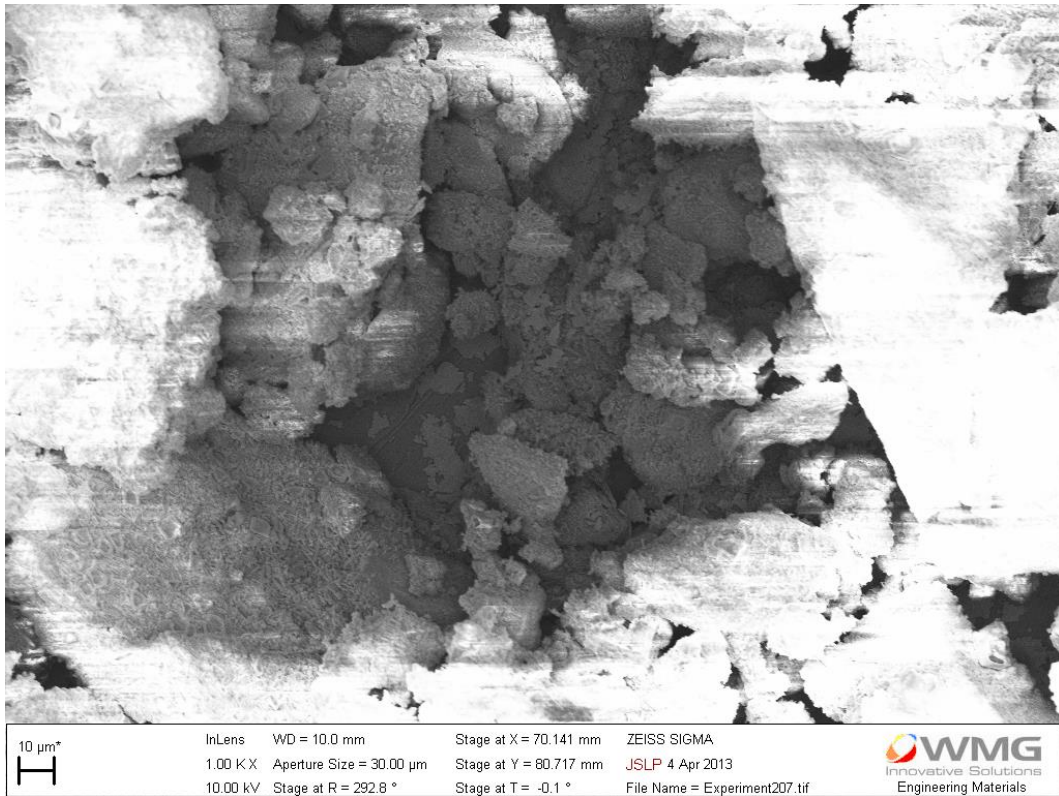


Figure 31: SEM micrograph of ALB2 sintered at 800 °C

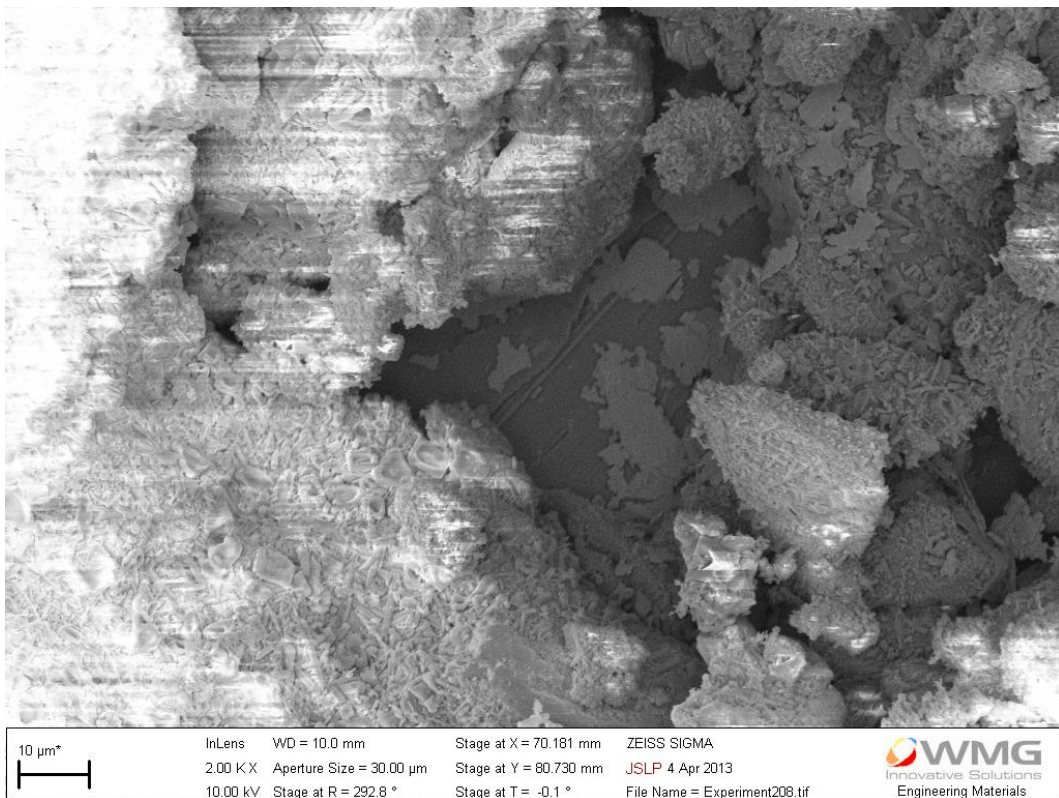


Figure 32: SEM micrograph of ALB2 sintered at 800 °C

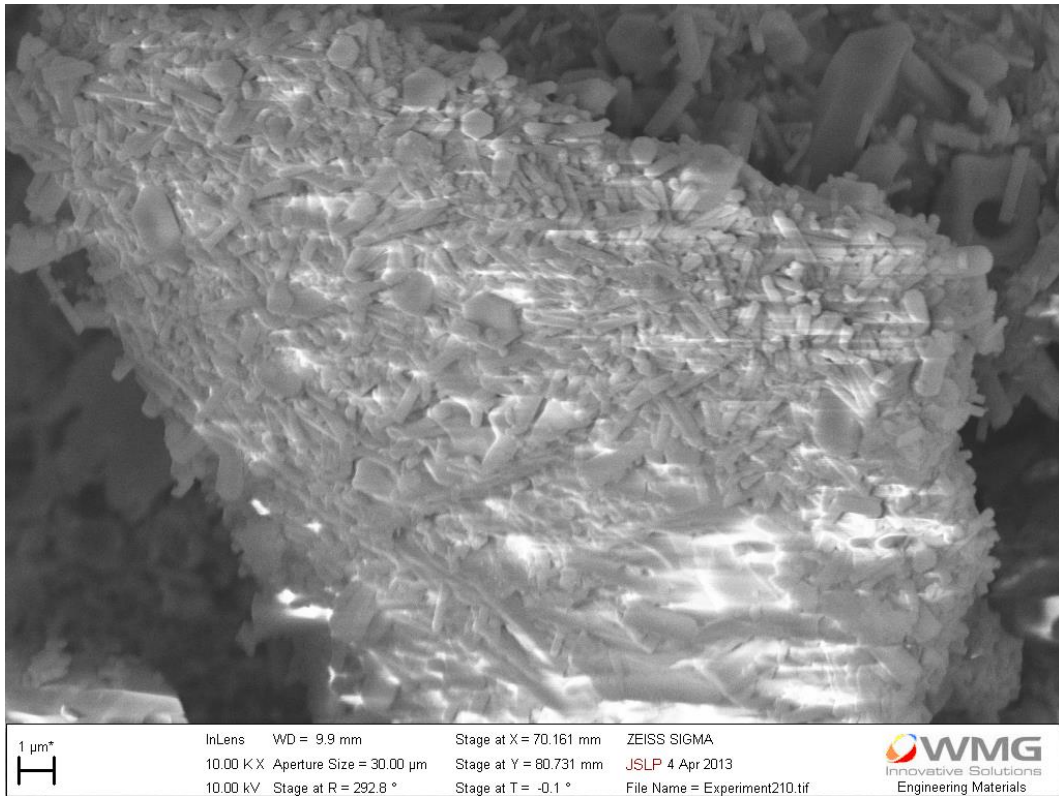


Figure 33: SEM micrograph of ALB2 sintered at 800 °C

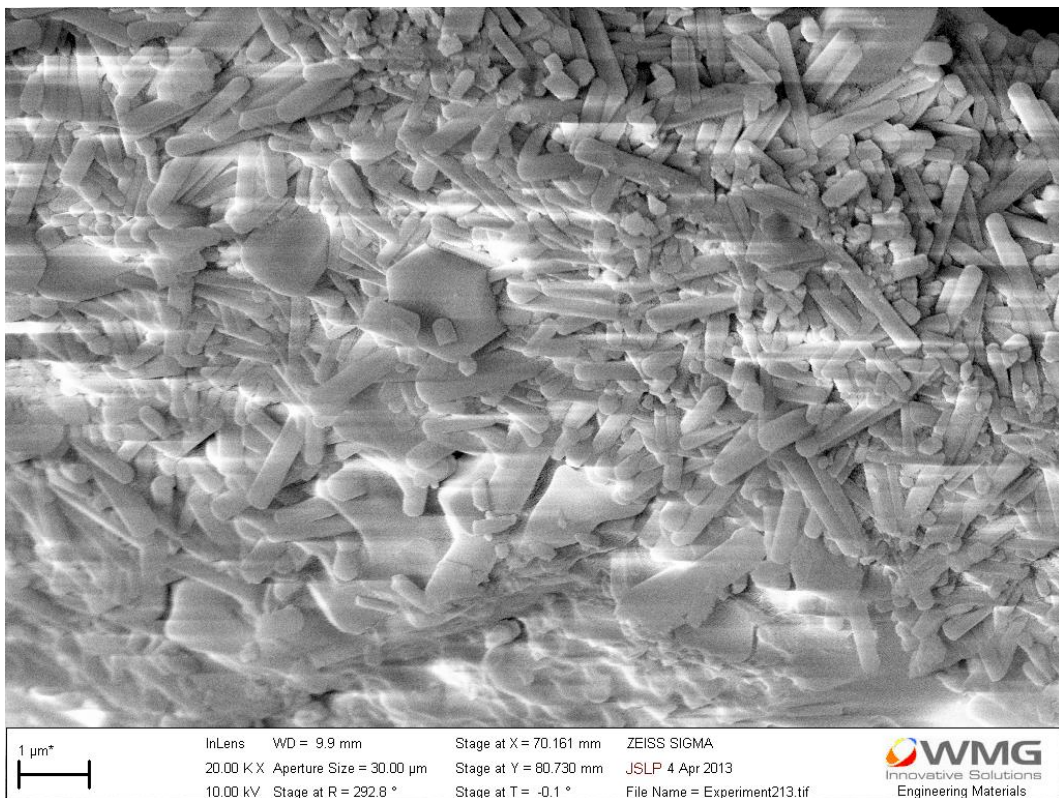


Figure 34: SEM micrograph of ALB2 sintered at 800 °C

## 5.3.2.2 XRD

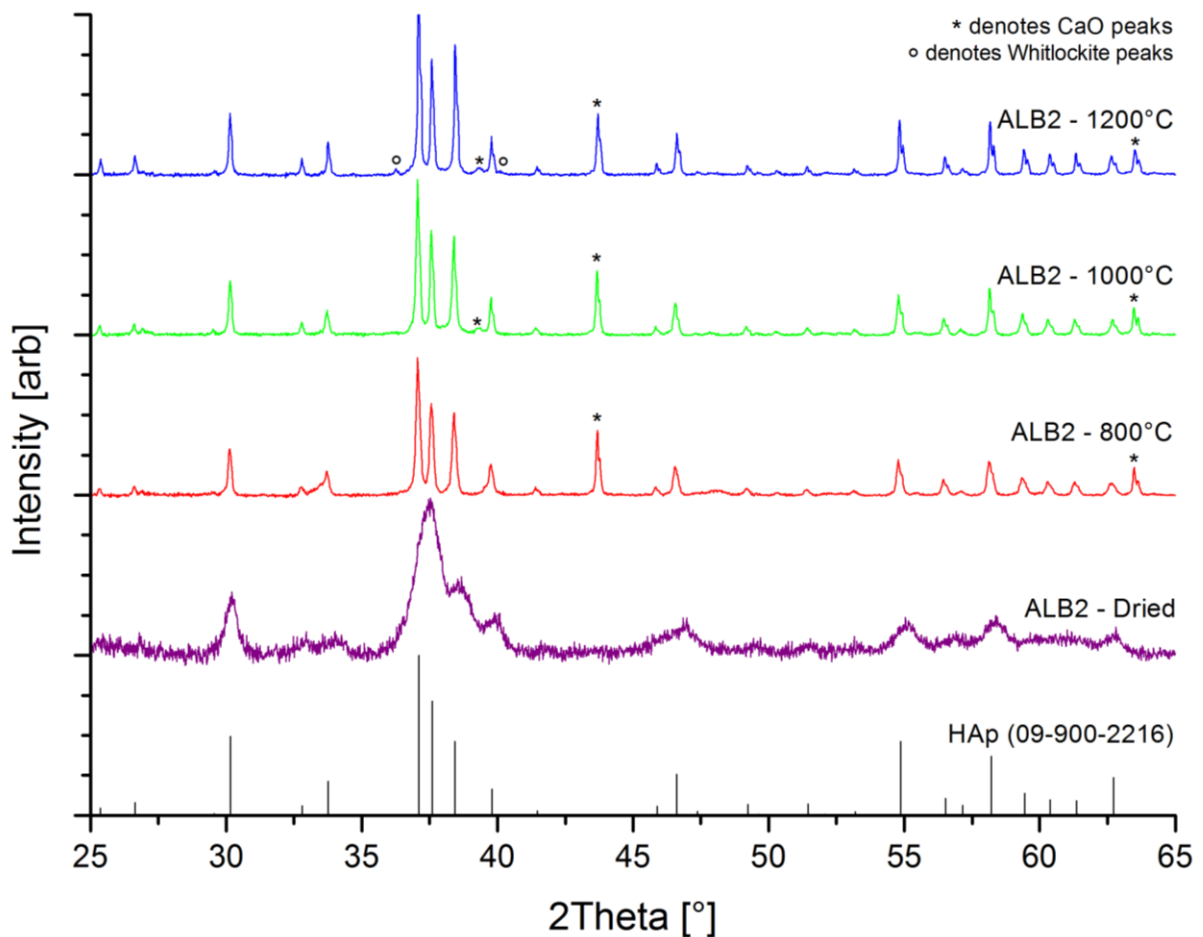


Figure 35: XRD spectra of ALB2 samples dried at 80 °C and sintered at 800, 1000 and 1200 °C

It can clearly be seen from Figure 35 that the XRD spectra of all samples of ALB2 were consistent with HAp with a nominal composition of  $\text{Ca}_{10}\text{P}_6\text{O}_{26}\text{H}_2$ , although a calcium oxide impurity is evident in all samples except for the dried sample, and a small quantity of Whitlockite is present in the sample sintered at 1200 °C, with a nominal composition of  $\text{Ca}_{60.69}\text{Mg}_{2.61}\text{P}_{42.00}\text{O}_{168.00}$ . Compositional analysis based upon the XRD spectra is presented in Table 12 and suggests that, excluding the CaO impurity, 3.2% of the HAp was converted to Whitlockite in the sample sintered to 1200 °C.

Table 12: Phase analysis of ALB2 samples at different temperatures expressed as a percentage

	80 °C	800 °C	1000 °C	1200 °C
CaO	0.0	31.9	29.2	23.8
HAp	100.0	68.1	70.8	73.7
Whitlockite	0.0	0.0	0.0	2.5

Crystallinity was greatly increased by sintering, from the amorphous form present after drying to the more crystalline form present after sintering at 1200 °C. As shown in Table 13, the crystallite sizes varied from 22.8 nm in the as dried sample to 184.7 nm in the sample sintered to 1200 °C. Crystallite

sizes were almost doubled by sintering to 1200 °C compared to sintering to 800 °C. The size of the crystallites in the sample sintered at 800 °C was around 101.2 nm, which is of the same order as the 100-300 nm diameter and 1-2 µm length of the produced nanorods shown in Figure 34.

**Table 13: Crystallite sizes for ALB2 estimated using the Scherrer equation**

Peak position	FWHM (2θ °)				Crystallite size (nm)			
	80 °C	800 °C	1000 °C	1200 °C	80 °C	800 °C	1000 °C	1200 °C
<b>30.2</b>	0.4093	0.1407	0.1023	0.0768	26.1	75.8	104.3	138.9
<b>37.5</b>	0.9210	0.1023	0.0895	0.0512	12.6	113.0	129.2	225.9
<b>38.6</b>	0.5117	0.1151	0.0895	0.0640	23.1	102.3	131.5	184.0
<b>39.9</b>	0.5117	0.1535	0.1791	0.0640	23.5	78.2	67.0	187.6
<b>58.4</b>	0.6140	0.1279	0.0768	0.0936	28.6	136.6	227.6	186.9
				<b>Mean</b>	<b>22.8</b>	<b>101.2</b>	<b>131.9</b>	<b>184.7</b>
				<b>Standard Deviation</b>	<b>6.1</b>	<b>25.3</b>	<b>59.5</b>	<b>30.9</b>

## 5.3.2.3 DTA-TGA

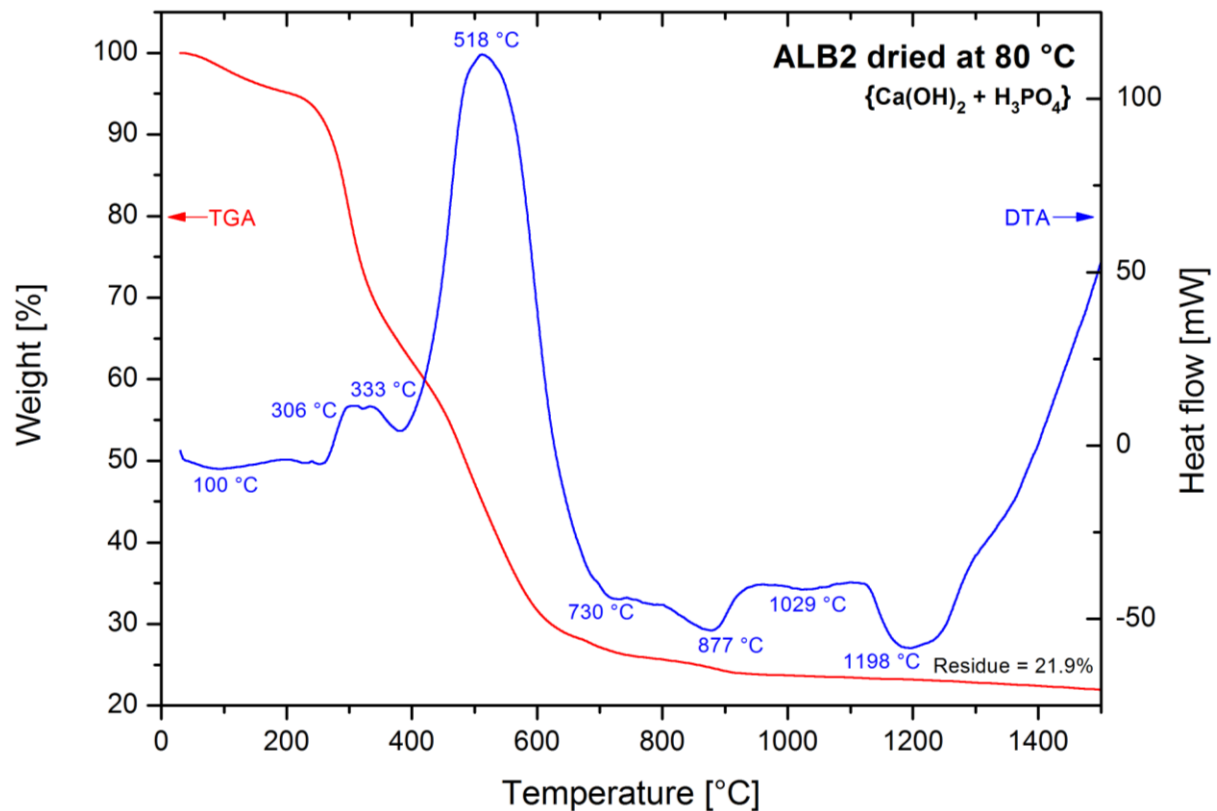


Figure 36: DTA-TGA curves for a sample of ALB2 dried at 80 °C

A small loss in mass with a corresponding endotherm can be seen up to 100 °C; this relates to the loss of absorbed water.

Peaks at 306 °C and 333 °C are the result of the combustion of a portion of the protein present in the sample. This is consistent with the experimental observations from ALB1 described in §4.4.1, in which the protein was seen to be charred and black after heating to 450 °C. The large mass loss observed relates to the combustion of the remaining carbonaceous material from the protein, with an exothermic peak at 518 °C.

A very small mass loss can be seen, with a similarly small endothermic peak at 730 °C, and is the result of the calcination of calcium carbonate into calcium oxide. Despite the large proportion of calcium oxide in the sample (>20%), the mass loss is very small, possibly due to the effect of encapsulation within the dried protein, which prevented carbon dioxide from reaching the calcium oxide until the sample was ground for analysis. The endotherm at 877 °C is also accompanied by a small mass loss and represents the calcination of magnesium carbonate into magnesium oxide.

Endotherms at 1029 °C and 1198 °C represent temperatures at which phase transformations of HAP to Whitlockite occur, which can be inferred from comparison with the XRD spectra for samples sintered at 1000 and 1200 °C.

## 5.3.2.4 FTIR

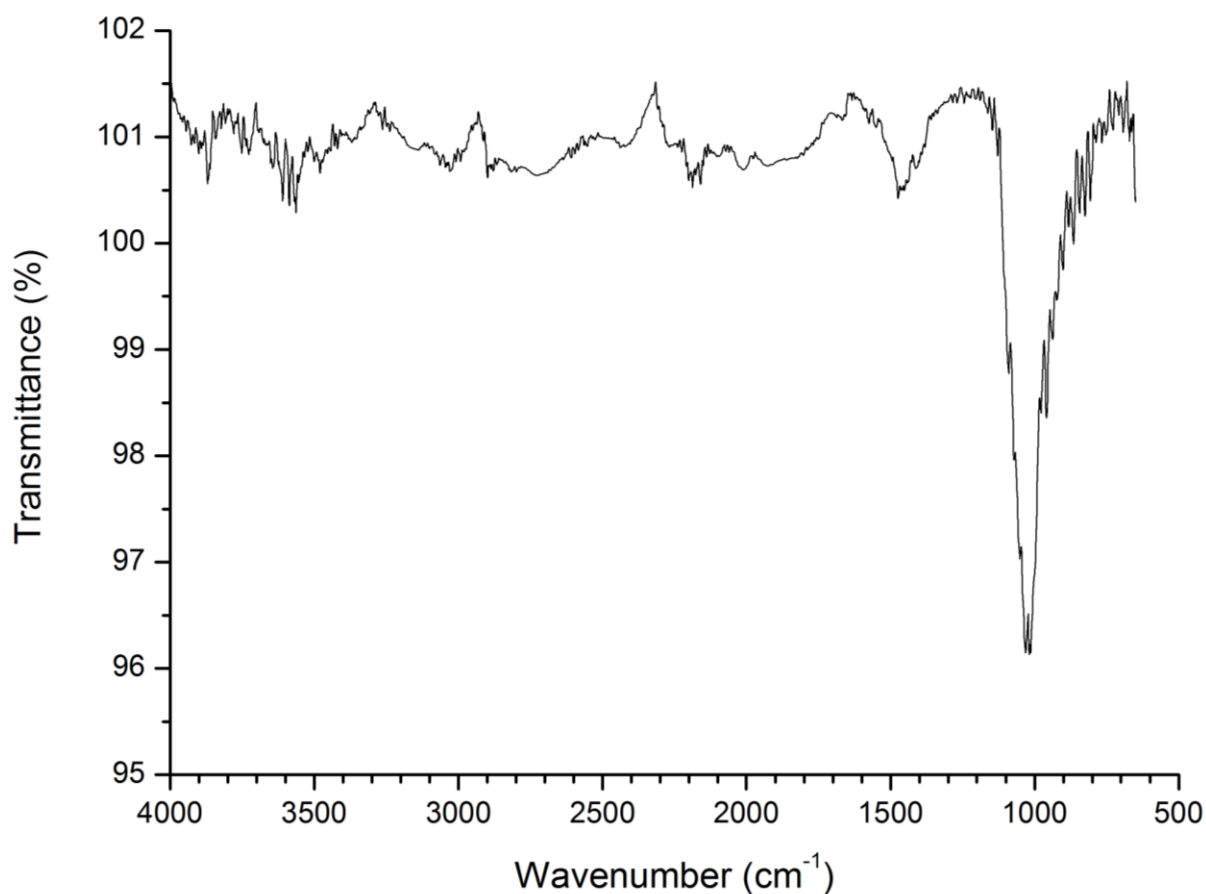


Figure 37: FTIR spectrum for ALB2 sintered at 800 °C

Large peaks corresponding to  $\text{HPO}_4^{2-}$  and  $\text{PO}_4^{3-}$  can be seen at  $1019\text{ cm}^{-1}$  and  $1030\text{ cm}^{-1}$ , respectively. Another peak at  $958\text{ cm}^{-1}$  can correspond to either  $\text{PO}_4^{3-}$  or  $\text{HPO}_4^{2-}$ , whilst a peak at  $1095\text{ cm}^{-1}$  indicates the presence of either  $\text{HPO}_4^{2-}$  or  $\text{CO}_3^{2-}$ .

Peaks at  $1411\text{ cm}^{-1}$  and  $1475\text{ cm}^{-1}$  indicate the presence of  $\text{CO}_3^{2-}$ . However, this does not confirm whether CHAp was produced or not, as these peaks may result from the presence of a calcium carbonate impurity; calcium oxide was shown in §5.3.2.2 (Figure 35) to be present in the sample, and this reacts with carbon dioxide in the air to form calcium carbonate.

Absorbed water is indicated by peaks at  $3420\text{ cm}^{-1}$  and  $3741\text{ cm}^{-1}$ , whilst the peak at  $3586\text{ cm}^{-1}$  indicates the presence of  $\text{OH}^-$ .

### 5.3.3 Experiment 3 (ALB3)

#### 5.3.3.1 SEM

Figure 38 shows significant variations in particle size and morphology. Large plate-like structures can be seen with dimensions of 200-600  $\mu\text{m}$ , whilst irregularly shaped particles are also present with sizes ranging from a few microns to a few hundred microns.

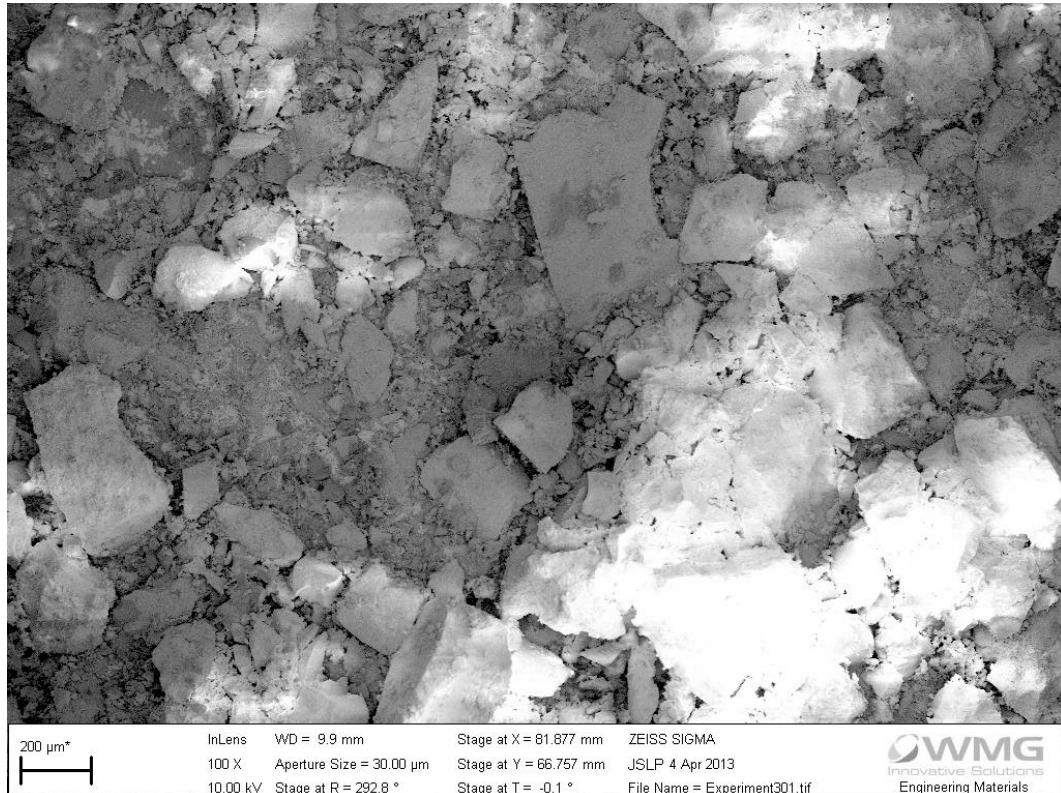


Figure 38: SEM micrograph of ALB3 sintered at 800 °C

The large plate-like structure found near the centre of Figure 38 can be seen in Figure 39 to have a rough surface with numerous smaller particles deposited on top. In Figure 40 it is made clear that the observed roughness is a result of the nanoporosity of the plate-like structure, which consists of nanospheres which have fused together. Figure 41 further demonstrates the nanocrystalline nature of the sample and shows that the crystals have diameters in the range of 100-250 nm. Grain boundaries can be seen between the spherical crystals.

The spherical morphology is the result of the high pH maintained during synthesis and the size is indicative of the relatively long aging time. The nanoporosity present between the fused spheres is the result of the lack of pressure during sintering.

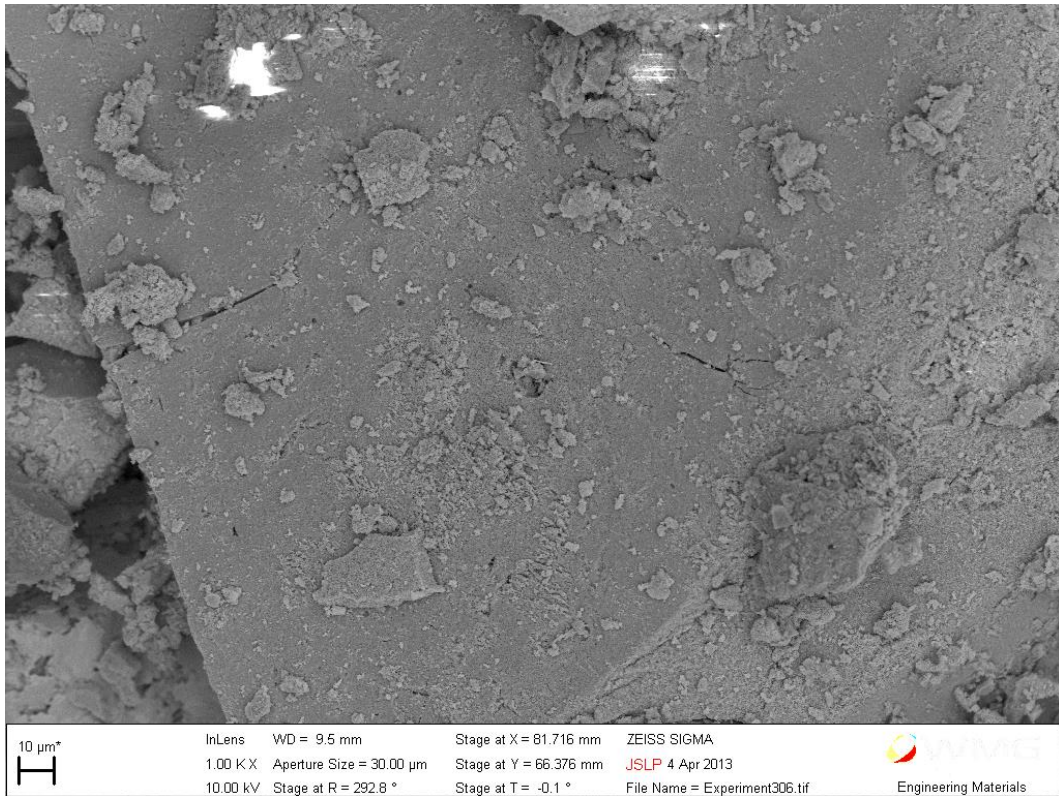


Figure 39: SEM micrograph of ALB3 sintered at 800 °C



Figure 40: SEM micrograph of ALB3 sintered at 800 °C

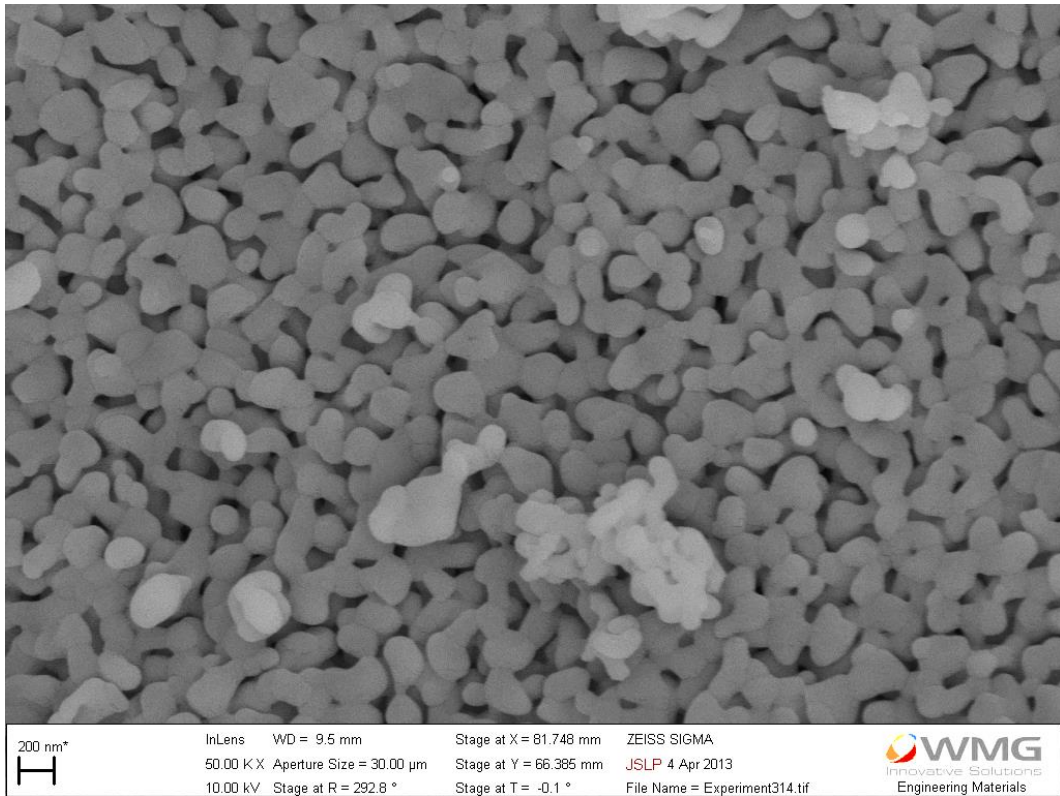


Figure 41: SEM micrograph of ALB3 sintered at 800 °C

## 5.3.3.2 XRD

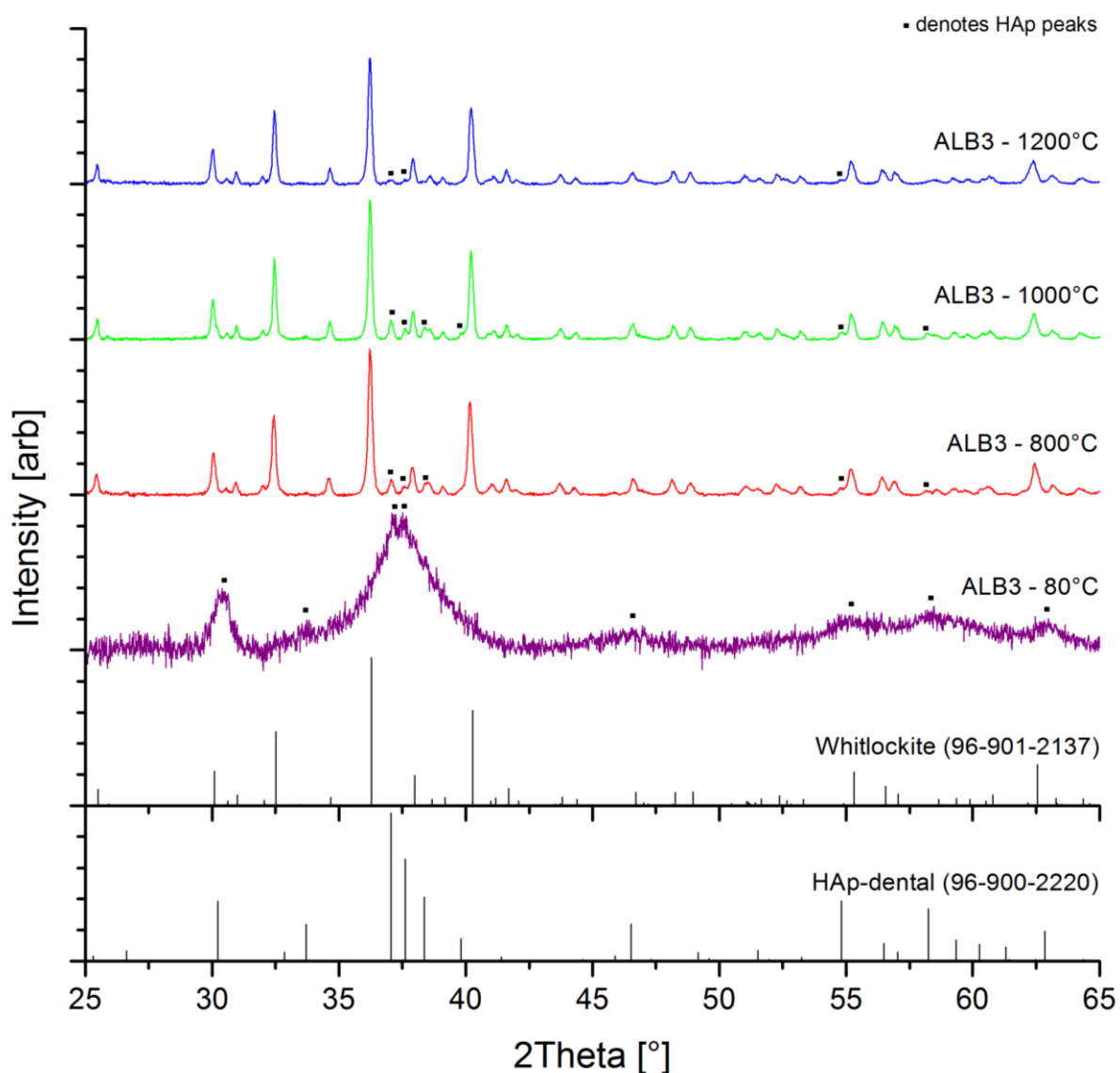


Figure 42: XRD spectra of ALB3 dried at 80 °C and sintered at 800, 1000 and 1200 °C

It can clearly be seen in Figure 42 that the sample dried at 80 °C is highly amorphous and that the spectrum is consistent with the standard spectrum for substituted HAp with a nominal composition of  $\text{Ca}_{9.40}\text{Na}_{0.20}\text{Mg}_{0.10}\text{P}_{5.22}\text{O}_{25.02}\text{H}_{0.92}$ . This suggests that magnesium has been incorporated into the apatitic structure, altering the crystal structure and causing a shift in the XRD peak positions. Whilst there may be some sodium present in the structure, it is unlikely to have been incorporated into the structure in the quantities that the nominal composition suggests, as the magnesium content of eggshell ( $\approx 1\%$ ) is much higher than the sodium content ( $\approx 0.09\%$ ); it was demonstrated by Siddharthan et al [17] that sodium is incorporated into hydroxyapatite less readily than magnesium.

For the samples sintered at 800, 1000 and 1200 °C it is clear that the dominant phase is Whitlockite, with a nominal composition of  $\text{Ca}_{60.69}\text{Mg}_{2.31}\text{P}_{42.00}\text{O}_{168.00}$ . This suggests that magnesium has been

incorporated into the structure, but it also indicates that the HAp present in the sample dried at 80 °C has decomposed into Whitlockite. A further change can be seen between the samples sintered at 1000 °C and 1200 °C, where most of the remaining HAp has decomposed into Whitlockite, lowering the proportion from 12.1% to 2.7%. Whilst the data in Table 14 suggest that the proportion of Whitlockite was decreased by sintering to 1000 °C compared to 800 °C, this variation is most likely due to the approximate nature of the peak intensity analysis and is not expected to reflect an actual change in composition.

**Table 14: Phase analysis of ALB3 samples at different temperatures expressed as a percentage**

	80 °C	800 °C	1000 °C	1200 °C
<b>Whitlockite</b>	0.0	90.9	87.9	97.3
<b>HAp</b>	100.0	9.1	12.1	2.7

**Table 15: Crystallite size for ALB3 dried at 80 °C estimated using the Scherrer equation**

Peak position	FWHM (2 $\theta$ °)		Crystallite size (nm)	
	80 °C		80 °C	
<b>11.5</b>	1.6374		5.7	
<b>30.4</b>	0.6140		15.6	
<b>37.4</b>	1.8420		5.3	
<b>55.2</b>	1.2280		8.5	
<b>58.5</b>	2.0467		5.2	
	<b>Mean</b>		<b>8.0</b>	
	<b>Standard Deviation</b>		<b>4.4</b>	

**Table 16: Crystallite sizes for ALB3 sintered at 800, 1000 and 1200 °C estimated using the Scherrer equation**

Peak position	FWHM (2 $\theta$ °)			Crystallite size (nm)		
	800 °C	1000 °C	1200 °C	800 °C	1000 °C	1200 °C
<b>19.8</b>	0.1023	0.0768	0.1023	91.5	121.9	91.5
<b>30.1</b>	0.1279	0.1279	0.1151	74.7	74.7	83.0
<b>32.4</b>	0.1535	0.0895	0.1023	62.6	107.4	93.9
<b>36.2</b>	0.1023	0.1407	0.1279	94.9	69.0	75.9
<b>40.2</b>	0.0895	0.1407	0.1023	109.7	69.8	96.0
			<b>Mean</b>	<b>86.7</b>	<b>88.6</b>	<b>88.1</b>
			<b>Standard Deviation</b>	<b>18.4</b>	<b>24.5</b>	<b>8.4</b>

There is a significant amount of peak broadening seen in Figure 42, particularly for the sample dried at 80 °C. Numerical analysis of crystallite sizes is given in Table 15 and Table 16. A size of 8.0 nm was found for the sample dried at 80 °C and whilst crystallite size was increased by sintering, little variation is seen between sintering temperatures, with sizes of 86.7, 88.6 and 88.1 nm estimated for samples sintered at 800, 1000 and 1200 °C, respectively. This indicates that the crystallite size of the produced Whitlockite is independent of the sintering temperature for this range.

## 5.3.3.3 DTA-TGA

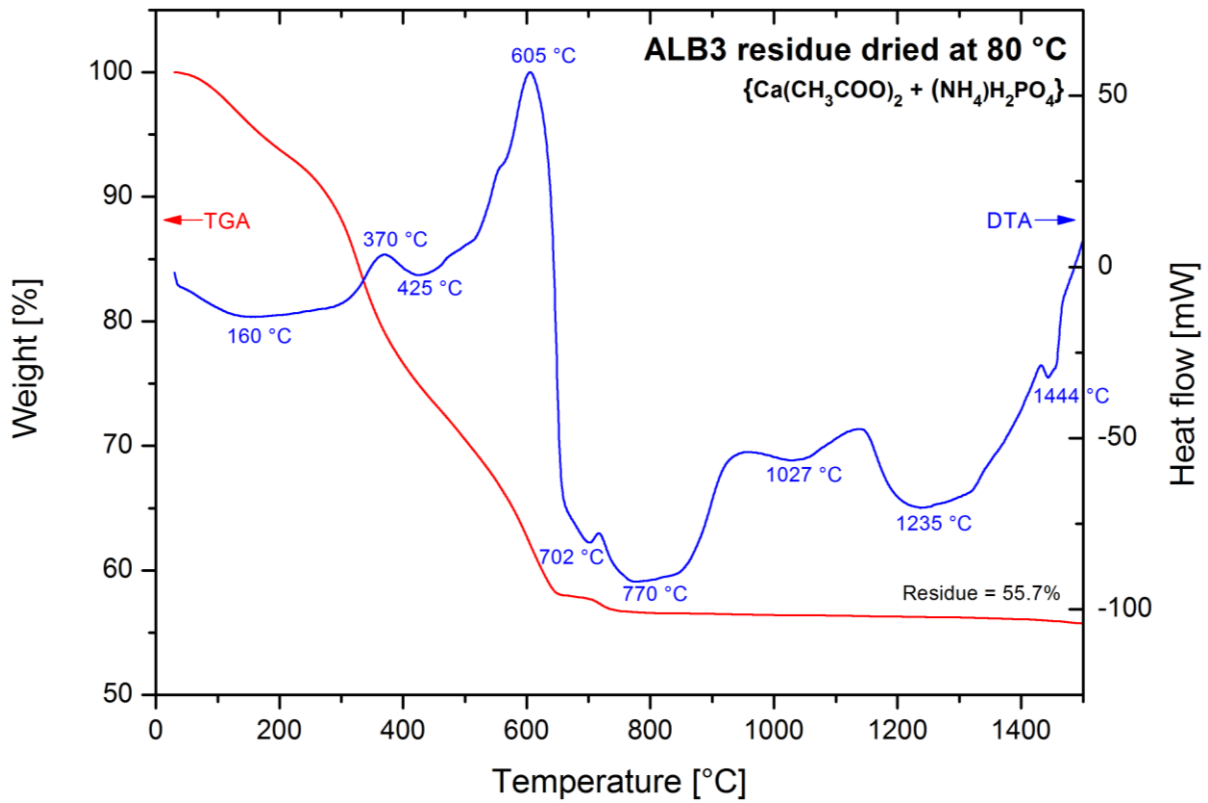


Figure 43: DTA-TGA curves for the filtration residue of ALB3 dried at 80 °C

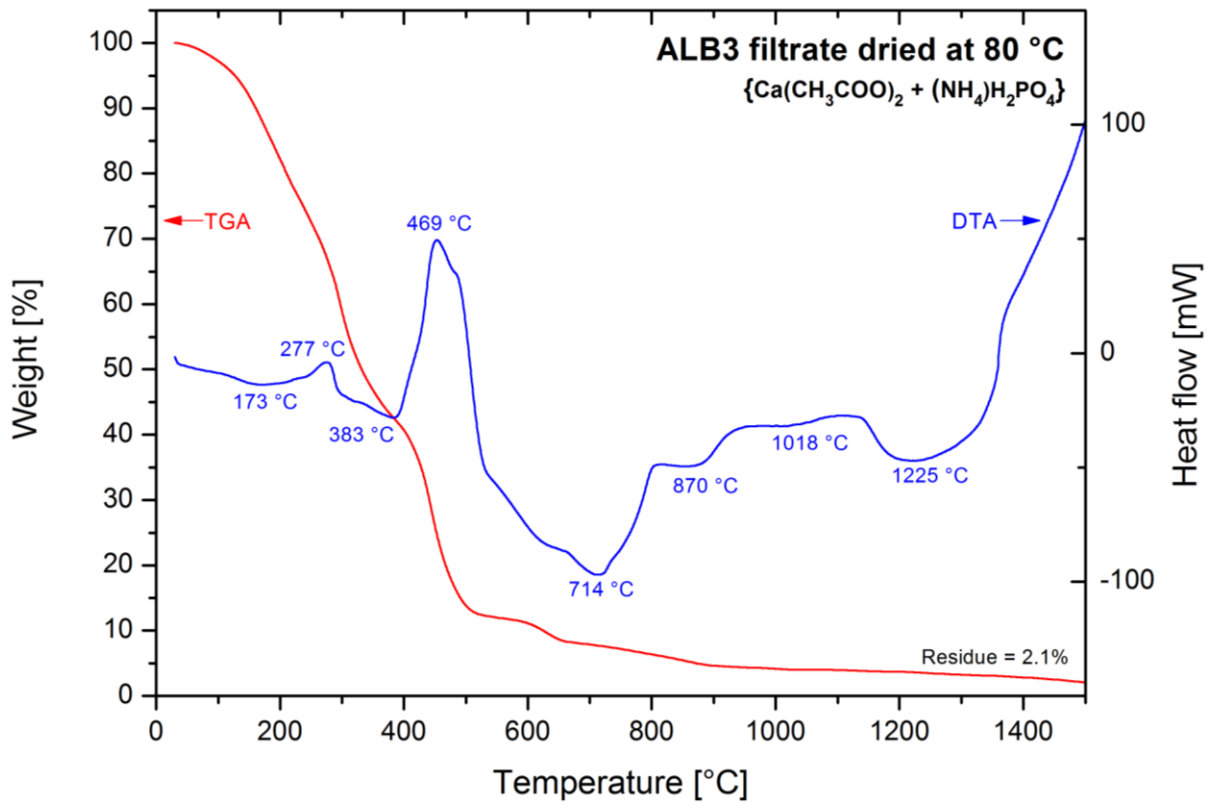


Figure 44: DTA-TGA curves for the filtrate of ALB3 dried at 80 °C

The endothermic peaks at 160 °C and 173 °C in the residue and filtrate, respectively, relate to polymeric softening of the dried albumen. The mass loss in this region indicates that there is small amount of combustion occurring at these temperatures. Small exotherms can be seen at 370 °C in Figure 43 and 277 °C in Figure 44, indicating combustion of the protein in the samples.

Endothermic peaks at 425 °C and 383 °C in the residue and filtrate, respectively, are believed to relate to the decomposition of HAp into Whitlockite, although this is not certain and further XRD analysis of samples heated to temperatures in this range would be necessary to confirm this belief.

Comparison of the DTA-TGA curves for the residue and filtrate shows that the exotherm corresponding to the combustion of the remaining carbonaceous material occurs at substantially different temperatures for each sample: 605 °C for the residue and 469 °C for the filtrate. This demonstrates that the combustion of the water-soluble proteins occurs at a lower temperature than the combustion of the insoluble proteins and possibly denatured proteins found in the residue.

For the residue, a very small endotherm can be seen at 702 °C and relates to the calcination of calcium carbonate into calcium oxide. The shape of the DTA curve in this region, with the very steep drop after the exotherm at 605 °C and a slight rise after the endotherm at 702 °C is believed to indicate that combustion may not have finished before 702 °C, and so the two enthalpy changes were concurrent.

For the filtrate, an endotherm accompanied by small mass loss can be seen at 714 °C and is expected to relate to the calcination of calcium carbonate into calcium oxide, indicating the presence of a very small impurity which was not indicated in the XRD spectra presented in §5.3.3.2 (Figure 42). Another endotherm at 870 °C relates to the calcination of magnesium carbonate. For the residue however, the peak relating to the calcination of magnesium carbonate appears as a broad peak at 770 °C, suggesting that it calcined at a lower temperature.

The DTA-TGA curves for the residue and filtrate of ALB3 are broadly similar for temperatures greater than 900 °C. This suggests that there is a small amount of the produced apatite in the filtrate and that this underwent the same phase changes, although the residue for the filtrate was only 2.1%, a portion of which is expected to be the ash content of the albumen.

The endothermic peak at 1027 °C in the residue and 1018 °C in the filtration is most likely due to the conversion of HAp into Whitlockite as this is consistent with the change observed in the XRD spectra shown in Figure 42. The endotherm at 1235 °C in the residue and 1225 °C in the filtration is expected to be another phase change, perhaps the conversion of the remaining HAp into Whitlockite, although the exact change cannot be determined without further XRD study of samples sintered at

temperatures greater than this expected decomposition temperature. Another possibility is a phase change to Mg-substituted  $\alpha$ -TCP, however this is not expected as Mg-Whitlockite has been shown to be stable at temperatures up to 1450 °C [24].

#### 5.3.3.4 FTIR

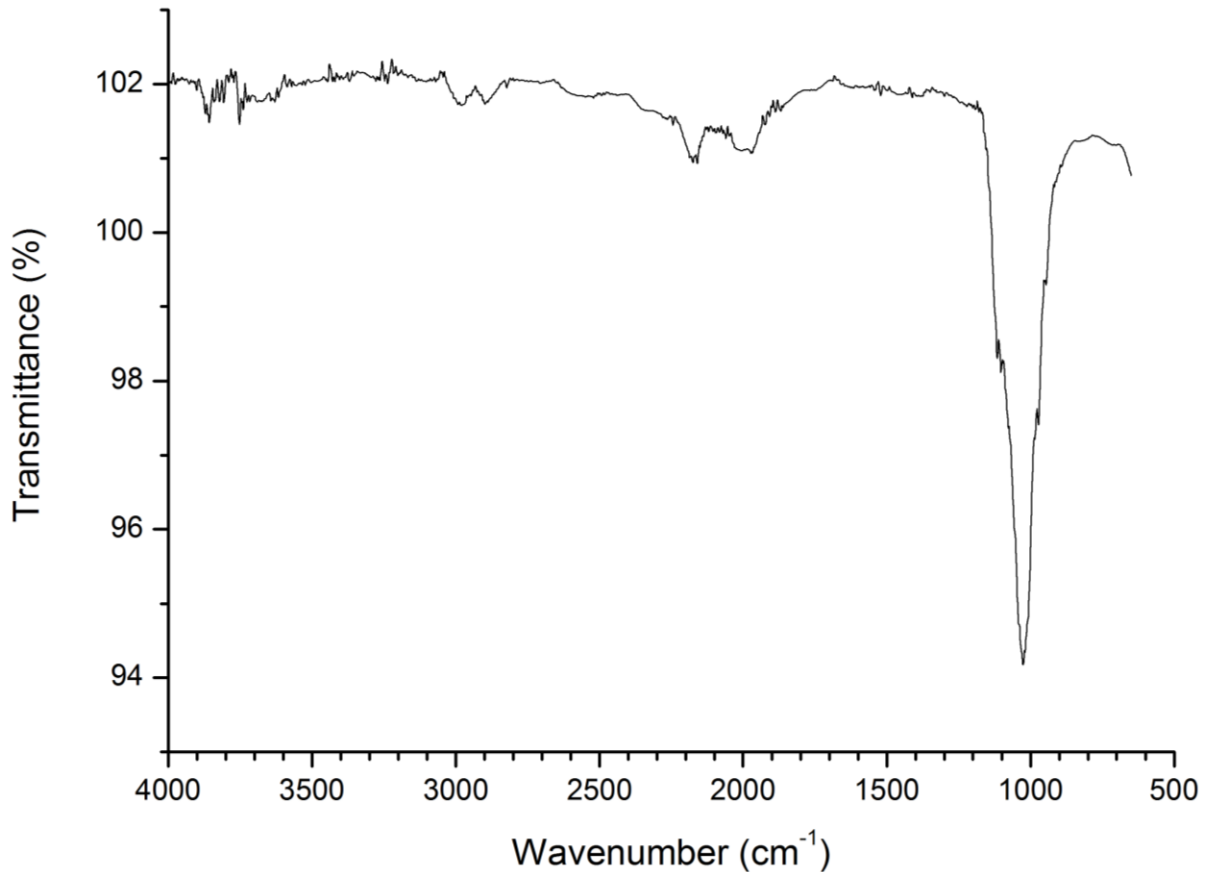


Figure 45: FTIR spectrum for ALB3 sintered at 800 °C

The FTIR spectrum for ALB3 sintered at 800 °C is given in Figure 45; a large peak indicating the presence of  $\text{PO}_4^{3-}$  can be seen at  $1026 \text{ cm}^{-1}$ .

A small peak at  $1116 \text{ cm}^{-1}$  indicates the presence of  $\text{CO}_3^{2-}$ , but a lack of significant peaks in the region of  $1400\text{-}1480 \text{ cm}^{-1}$  demonstrates that there is very little carbonate in the samples, and as previously discussed in §5.3.1.4, the presence of carbonate can be the result of calcium oxide impurities which have become carbonated.

Peaks corresponding to harmonic overtones are visible at  $1992, 2175, 2185, 2906$  and  $2979 \text{ cm}^{-1}$ , and the presence of absorbed water is indicated by a peak at  $3753 \text{ cm}^{-1}$ .

# Chapter 6: Discussion

*Chapter 6 presents a discussion of the results presented in Chapter 5, and builds upon this by comparing the results of each experiment. Differences in the results are noted and the potential mechanisms discussed.*

## 6.1 Microwave-assisted Synthesis

The XRD of MIC 2 showed that there was a partial decomposition of the produced HAp into  $\beta$ -TCP when the sample was heated to between 600 and 800 °C. However, MIC1 was shown to be thermally stable and not undergo this same decomposition until 1169 °C. This represents a very large difference in thermal stability, without any difference in crystallinity. MIC1 was synthesised from a phosphoric acid precursor, whilst diammonium hydrogen phosphate was used to synthesise MIC2. The only difference between these experiments was the choice of phosphate precursor, therefore this suggests that thermal stability may be affected by the choice of precursor, with phosphoric acid producing more thermally stable HAp than diammonium phosphate. Thermal stability is expected to rely upon the degree of substitution as well as the Ca/P ratio, since both of these affect the crystal lattice structure, and so the choice of precursor may affect the Ca/P ratio and/or degree of substitution, although further study would be necessary to confirm this.

Both MIC1 and MIC2 were shown to produce amorphous HAp, with the samples typically having crystallite sizes 20 nm for temperatures from 80 to 600 °C, only increasing slightly to 30 nm after heating to 800 °C. The similarity of crystallite sizes shows that there was little to no difference in the crystallinity produced based upon the choice of phosphate precursor, for those investigated. It should be noted however, that crystallite sizes were seen to be consistently, although not significantly, higher for MIC2 than for MIC1; this may indicate that there is a relationship that is not fully shown at such small sizes, but no conclusion can be drawn from the data presented in this report.

## 6.2 Albumen-mediated Synthesis

ALB1 demonstrated that calcium hydroxide can cause albumen to gel. The fact that the same gelling did not occur for ALB2 suggests that this gelling behaviour may be pH dependent, as the addition of phosphoric acid causes a drop in pH. Another possible mechanism for this behaviour is the albumen-water ratio, which is reduced by the addition of the aqueous phosphoric acid.

A difference was demonstrated between HAp synthesised from calcium acetate and that synthesised from calcium hydroxide. It is important to note however, that the phosphate precursor was also varied, with calcium hydroxide being matched with phosphoric acid and calcium acetate being matched with ammonium dihydrogen phosphate. The HAp which was synthesised from a calcium acetate precursor (ALB3) partially decomposed to Whitlockite at a lower temperature than either ALB1 or ALB2, whilst still undergoing similar HAp-to-Whitlockite phase changes at higher temperatures. The highly amorphous nature of the as dried sample of ALB3 indicates that calcium acetate may produce smaller crystallite sizes; however, a large inclusion of magnesium into the structure may distort the lattice sufficiently to cause peak broadening through the presence of lattice imperfections. A high degree of substitution and a large number of lattice imperfections could lead to reduced thermal stability, promoting a major conversion of HAp to Whitlockite at substantially lower temperatures. If the choice of precursor affects the degree of ionic substitution, then this could account for both the highly amorphous nature of ALB3, and the lower temperature conversion of HAp to Whitlockite. Nonetheless, it cannot be concluded from these experiments whether the effect is due to the calcium precursor, the phosphate precursor or a combination of the two.

ALB1 produced showed a significant variation in particle size and morphology, which was indicative of the uncontrolled nature of the synthesis method used. Both rod-like and near-spherical morphologies were seen, which are consistent with a high pH. ALB2 produced a rod-like morphology whilst ALB3 produced a near-spherical morphology. Variation of particle morphology was most likely due to variation of the initial pH of the reaction. In the case of ALB2, the pH was determined to be highly basic, but due to the lack of a quantitative measure, it is not known whether the pH was slightly lower than the intended pH of 12. However, for ALB3, a large quantity of ammonium hydroxide was added, and so the pH was likely significantly higher than the intended value of 12. Due to the strong dependence of morphology on pH, it is expected that this is the reason for the observed morphological variation.

Crystallite sizes were consistently higher for ALB2 compared to ALB3, indicating that the synthesis from calcium acetate and ammonium dihydrogen phosphate produced more amorphous HAp than the synthesis from calcium hydroxide and phosphoric acid. For the as produced samples crystallite sizes were estimated to be 23 nm and 8 nm for ALB2 and ALB3, respectively. It was also demonstrated that the crystallite size for ALB3 was approximately 90 nm after heating to 800 °C and that the size was stable up to 1200 °C. However, for ALB2, the crystallite size was approximately 90 nm after heating to 800 °C and continued to increase to 130 nm and 185 nm after heating to 1000 °C and 1200 °C, respectively. This effect may be the result of the predominantly Whitlockite composition of ALB3, compared to the purely HAp composition of ALB3.

The difference in as dried crystallite sizes may be the result of the different way in which the albumen responded during the synthesis experiments. In ALB2, the albumen appeared to thicken slightly, but there was visible change to the protein other than the colour change due to the added reagents and subsequent precipitate. However, in ALB3, very fine protein structures were formed which are believed to have encapsulated the synthesised HAp. These may have significantly limited crystallite growth, leading to the production of a more amorphous apatite.

### 6.3 Comparison of Synthesis Methods

Microwave-assisted synthesis produced crystallite sizes of 20 nm for as dried samples and 30 nm after heating to 800 °C. The as dried crystallite sizes of MIC1 and MIC2 were comparable to those of ALB2 (25 nm), but higher than that of ALB3 (8 nm). This indicates that both methods are capable of producing HAp with small crystallite sizes, although heating of ALB2 and ALB3 substantially increased crystallite sizes beyond that of MIC1 and MIC2, producing crystallites of 90 nm and 100 nm for ALB2 and ALB3, respectively. This difference may be the result of the synthesis route, or it may be the result of the longer heat treatment times used in the synthesis of ALB2 and ALB3.

# Chapter 7: Conclusions

*This Chapter summarises the conclusions which can be drawn from the work presented in this report.*

## 7.1 Microwave-assisted Synthesis

The ability of microwave-assisted synthesis methods to rapidly produce nanocrystalline HAp was demonstrated.

Nanocrystalline HAp was synthesised from eggshell-derived calcium hydroxide and phosphoric acid using a microwave-assisted method. The produced apatite was demonstrated to be thermally stable up to 800 °C with DTA-TGA suggesting thermal stability up to 1169 °C. No increase of crystallite size was observed for temperatures up to 600 °C, but heating to 800 °C showed an increase from less than 20 nm to approximately 30 nm.

Similarly nanocrystalline HAp was synthesised from diammonium hydrogen phosphate using the same methodology. The apatite was shown to be thermally stable up to 600 °C, but partially decomposed to a biphasic mixture of 29%  $\beta$ -TCP and 71% HAp, excluding impurities, when heated to 800 °C. Crystallite sizes were shown to be independent of temperature up to 600 °C, but increased from less than 20 nm to less than 30 nm when heated to 800 °C.

A potential dependence of thermal stability on the choice of phosphate precursor was indicated. HAp synthesised from  $(\text{NH}_4)_2\text{HPO}_4$  was shown to undergo decomposition to  $\beta$ -TCP at a much lower temperature (600-800 °C) than HAp synthesised from  $\text{H}_3\text{PO}_4$  (1169 °C).

## 7.2 Albumen-mediated Synthesis

Albumen-mediated synthesis has been shown to be an effective method for the synthesis of nanocrystalline Mg-substituted apatites. The production of nano-sized particles has also been demonstrated.

For the first time, a novel hydroxyapatite synthesis method was demonstrated, in which gelled albumen, containing evenly dispersed calcium hydroxide, was burnt in the presence of phosphoric acid. Two particle morphologies were produced with near-spherical morphologies having diameters less than 2.5  $\mu\text{m}$  and short rod-like morphologies having lengths less than 6  $\mu\text{m}$  and diameters less than 2  $\mu\text{m}$ . The thermal stability of the hydroxyapatite up to 1000 °C was demonstrated and a conversion to Whitlockite was indicated at 1094 °C, with a 12% conversion to Whitlockite for samples sintered at 1200 °C.

Hydroxyapatite nanorods were produced from eggshell-derived calcium hydroxide and phosphoric acid via an albumen-mediated reaction. The nanorods were shown to have a length less than 2  $\mu\text{m}$  with diameters in the range of 100-300 nm. Crystallite sizes were estimated to be 23 nm in the sample dried at 80  $^{\circ}\text{C}$ , and were increased to 101, 132 and 185 nm upon sintering at 800, 1000 and 1200  $^{\circ}\text{C}$ , respectively. Thermal stability was demonstrated up to 1000  $^{\circ}\text{C}$ , with a conversion to 2.5% Whitlockite in the sample sintered at 1200  $^{\circ}\text{C}$ ; DTA-TGA suggested that the decomposition occurred at 1029  $^{\circ}\text{C}$ .

Highly amorphous Mg-substituted hydroxyapatite, with an estimated crystallite size of 8nm, was successfully produced via a novel albumen-mediated reaction between eggshell-derived calcium acetate and ammonium dihydrogen phosphate. This hydroxyapatite was shown to convert almost completely to Mg-containing Whitlockite with a content of approximately 10% HAp after sintering at 800  $^{\circ}\text{C}$  and just 2.7% after sintering at 1200  $^{\circ}\text{C}$ . The Whitlockite phase was found to be thermally stable for temperatures up to 1500  $^{\circ}\text{C}$ . Crystallite sizes were shown to be independent of sintering temperature for temperatures between 800  $^{\circ}\text{C}$  and 1200  $^{\circ}\text{C}$ , remaining constant at 85-90 nm. A near-spherical morphology was demonstrated, with typical diameters in the range of 100-250 nm; these were seen to have been sintered into nanoporous structures in a sample heated to 800  $^{\circ}\text{C}$ . FTIR confirmed the lack of carbonation.

# Chapter 8: Recommendations for Further Work

*Limitations and uncertainties identified in the current work are discussed, highlighting the areas on which future research should be focused in order to enhance the results achievable by the methods presented here.*

## 8.1 Reduction of Crystallite Size

Further work should focus on the reduction of crystal sizes. This should be achievable mainly through the reduction of aging times. High pH should also be maintained in order to ensure that spherical nanoparticles are produced, although if different morphologies are desirable for particular purposes, variation of the pH would be required.

## 8.2 Removal of Protein

An alternative method of separating the HAp from the protein should be found, as the high temperatures used to burn the protein off caused increased crystallite sizes and sintered the particles, fusing them into larger structures. It is possible that nanocrystals may have also been fused during the high temperature processing and so low temperature methods may produce particles which are much smaller than those produced by the current methodology. Alternative methods may include the use of centrifugation, enzymatic activity or the use of solvents, although the use of organic solvents has been contraindicated by cell studies. Filtration may also prove a useful method of separating the protein from the apatite in cases where there is no gelling or denaturing of the protein.

## 8.3 Properties of Albumen

The relationship between the albumen-water ratio and the produced particle size and morphology should be investigated, as variation is expected. The gelling behaviour of albumen should also be investigated, as control over the gelling behaviour may allow for greater control over particle size. Albumen has been shown to respond in three different ways and very little is known about what caused these varied responses. Understanding how albumen will respond would allow for far greater control over experimental conditions.

## 8.4 Effect of Precursor Choice

Comparison of MIC1 and MIC2 suggested that the thermal stability of produced HAp may be dependent upon the choice of phosphate precursor. Therefore, a range of phosphate precursors should be used with the same calcium precursor and synthesis methodology to see whether such a relationship exists.

Comparison of ALB2 and ALB3 further suggested that precursor choice may affect thermal stability, as well as the degree of substitution into the lattice. It would be necessary to compare apatites produced from both pure and eggshell-derived calcium precursors in order to determine whether the thermal stability of the apatites is dependent upon the choice of precursor, or upon the degree of substitution, as well as indicating whether the choice of precursor influences the degree of substitution. Elemental analysis using a method such as nuclear magnetic resonance spectroscopy (NMR) would allow for the extent of magnesium incorporation to be quantitatively determined.

The choice of precursor could influence many factors, including thermal stability, Ca/P ratio, cationic substitution, carbonation, crystallinity and particle size. Most of these factors are interdependent; for example, ionic substitutions change the Ca/P ratio and distort the lattice, leading to possible changes in crystallinity and thermal stability. If precursor dependence does exist, the knowledge gained from investigation of this would be highly valuable and would allow for the selection of precursors to be based upon the properties desired for the apatite to be produced. A standard methodology would need to be selected for this type of investigation and a large number of precursors should be analysed in multiple combinations, as well as with variation of the presence of substitutional ions.

## 8.5 Removal of Calcium Oxide Impurities

Significant amounts of calcium oxide were detected in the produced samples, which could impact the biocompatibility of the apatites. Therefore, methods should be found to remove excess calcium oxide from the samples, possibly by reacting it into a more soluble form. It is important however, to ensure that the reaction product is removed from the sample, and that the apatite is not altered by the extraction process. Dilute acids could be used to wash the sample after filtration.

## 8.6 Cell Studies and Biological Data

Cell studies should be conducted in order to determine the level of bioactivity of the produced samples as well as for similar samples produced from non-eggshell derived calcium precursors. This would demonstrate the benefit, and confirm the rationale, of using eggshell-derived precursors for the production of apatites for biomedical purposes.

Differences in cell response may be observed for variation in degree of substitution and crystallinity, as well as for differences in produced particle size and morphology. The method by which the apatite is separated from the protein may also have an effect, as it has previously been demonstrated that the use of organic solvents affects the reaction of a biological system.

## 8.7 Other Potential Synthesis Methods

### 8.7.1 Membrane templated

There is also the potential to use the eggshell membrane as a template on which to grow HAp crystals. This could be achieved by separating the two precursor solutions with the membrane and allowing diffusion to occur, with the reaction products remaining on the membrane.

### 8.7.2 Yolk templated

Another potential synthesis route is the use of egg yolk as a medium in which to conduct the reaction. This would be similar to microemulsion techniques currently in use but would avoid the need for the use of potentially harmful hydrocarbons such as octane, and would provide a renewable source. Due to the positive effects of yolk water-soluble protein (YSP), discussed in §2.4.3.2, there may also be a biological benefit to this method if the YSP can be retained within the produced apatites.

## Chapter 9: Project Costing

*The costs involved with conducting a project of this nature are highlighted and an approximation is made of the likely cost if this were to be undertaken by industry, assuming that the majority of the equipment was pre-existing.*

Costs for this project have been calculated using a rate of £50.00 per hour for academic or research staff, £20.00 per hour for support from technicians and £15.00 for the author's time. The cost of consumables has been recorded as incurred. Academic and research staff include Dr Kajal Mallick, Dr Ben Douglas, Dr Darren Hughes, James Winnet and Sophie Cox, whilst technical staff include John Pillier and Martin Davis.

The total cost of the project, shown in Table 17, is not unreasonable for a research project of this type, with publishable results and a worldwide influence on research into apatite synthesis and potentially the synthesis of other inorganic materials. The large time requirement for research and experiments means that the author's time is the main source of cost in this project, with two-thirds of the total cost being in this category. Collaboration with the University of Warwick and Warwick Manufacturing Group minimised equipment and software costs, as the majority of this was already available; equipment costs would have been overwhelming if these facilities had not been available, as equipment was often worth upwards of £10,000 due to the highly technical nature.

Table 17: Project cost

Description	Cost per unit	Number of units	Total Cost
Student time	£15 /h	300	£4500
Supervisor time	£50 /h	35	£1750
Other academic time	£50 /h	6	£300
Technician time	£20 /h	2	£40
Laboratory glassware	£130	-	£130
Chemical reagents	£30	-	£30
<b>TOTAL</b>			<b>£6750</b>

# References

1. Otsuka M, Nakahigashi Y, Matsuda Y, Fox JL, Higuchi WI, Sugiyama Y. A novel skeletal drug delivery system using self-setting calcium phosphate cement VIII: the relationship between in vitro and in vivo drug release from indomethacin-containing cement. *Journal of Controlled Release*. 1997; 43(2–3):115–122. doi:10.1016/S0168-3659(96)01493-9.
2. Baradari H, Damia C, Dutreih-Colas M, Laborde E, Pécout N, Champion E, et al. Calcium phosphate porous pellets as drug delivery systems: Effect of drug carrier composition on drug loading and in vitro release. *Journal of the European Ceramic Society*. 2012; 32(11):2679–2690. doi:10.1016/j.jeurceramsoc.2012.01.018.
3. Bose S, Tarafder S. Calcium phosphate ceramic systems in growth factor and drug delivery for bone tissue engineering: A review. *Acta Biomaterialia*. 2012; 8(4):1401–1421. doi:10.1016/j.actbio.2011.11.017.
4. Ginebra M-P, Canal C, Espanol M, Pastorino D, Montufar EB. Calcium phosphate cements as drug delivery materials. *Advanced Drug Delivery Reviews*. 2012; 64(12):1090–1110. doi:10.1016/j.addr.2012.01.008.
5. Riman RE, Suchanek WL, Byrappa K, Chen C-W, Shuk P, Oakes CS. Solution synthesis of hydroxyapatite designer particulates. *Solid State Ionics*. 2002; 151(1–4):393–402. doi:10.1016/S0167-2738(02)00545-3.
6. *Handbook of intelligent scaffolds for tissue engineering and regenerative medicine*. Singapore: Pan Stanford Publ; 2012.
7. Monteiro MM, da Rocha NCC, Rossi AM, de Almeida Soares G. Dissolution properties of calcium phosphate granules with different compositions in simulated body fluid. *Journal of Biomedical Materials Research Part A*. 2003; 65A(2):299–305. doi:10.1002/jbm.a.10479.
8. Park JB. *Biomaterials: An Introduction*. 3rd ed. New York, NY: Springer; 2007.
9. *An Introduction to bioceramics*. Singapore ; New Jersey: World Scientific; 1993.
10. Wang X-Y, Zuo Y, Huang D, Hou X-D, Li Y-B. Comparative Study on Inorganic Composition and Crystallographic Properties of Cortical and Cancellous Bone. *Biomedical and Environmental Sciences*. 2010; 23(6):473–480. doi:10.1016/S0895-3988(11)60010-X.
11. Narasaraju TSB, Phebe DE. Some physico-chemical aspects of hydroxylapatite. *JOURNAL OF MATERIALS SCIENCE*. 1996; 31(1):1–21. doi:10.1007/BF00355120.
12. Tucker KL, Hannan MT, Chen HL, Cupples LA, Wilson PWF, Kiel DP. Potassium, magnesium, and fruit and vegetable intakes are associated with greater bone mineral density in elderly men and women. *Am. J. Clin. Nutr*. 1999; 69(4):727–736.
13. Hynes RO. Integrins: Versatility, Modulation, and Signaling in Cell Adhesion. *Cell*. 1992; 69(1):11–25.
14. Vallet-Regí M. *Biomimetic nanoceramics in clinical use: from materials to applications*. Cambridge: Royal Society of Chemistry; 2008.

15. Hui P, Meena SL, Singh G, Agarawal RD, Prakash S. Synthesis of Hydroxyapatite Bio-Ceramic Powder by Hydrothermal Method. *Journal of Minerals & Materials Characterization & Engineering*. 2010; 9(8):683–692.
16. Witton T. Characterization of calcium oxide derived from waste eggshell and its application as CO<sub>2</sub> sorbent. *Ceramics International*. 2011; 37(8):3291–3298. doi:10.1016/j.ceramint.2011.05.125.
17. Siddharthan A, Sampath Kumar TS, Seshadri SK. Synthesis and characterization of nanocrystalline apatites from eggshells at different Ca/P ratios. *Biomedical Materials*. 2009; 4(4):045010. doi:10.1088/1748-6041/4/4/045010.
18. Noshi T, Yoshikawa T, Ikeuchi M, Dohi Y, Ohgushi H, Horiuchi K, et al. Enhancement of the in vivo osteogenic potential of marrow/hydroxyapatite composites by bovine bone morphogenetic protein. *Journal of Biomedical Materials Research*. 2000; 52(4):621–630. doi:10.1002/1097-4636(20001215)52:4<621::AID-JBM6>3.0.CO;2-A.
19. Gilbert RP, Liu Y, Groby J-P, Ogam E, Wirgin A, Xu Y. Computing porosity of cancellous bone using ultrasonic waves, II: The muscle, cortical, cancellous bone system. *Mathematical and Computer Modelling*. 2009; 50(3–4):421–429. doi:10.1016/j.mcm.2008.06.021.
20. Raven PH, Johnson GB. *Biology*. Boston: McGraw-Hill, Higher Education; 2005.
21. Legeros RZ, Trautz OR, Legeros JP, Klein E, Shirra WP. Apatite Crystallites: Effects of Carbonate on Morphology. *Science*. 1967; 155(3768):1409–1411. doi:10.1126/science.155.3768.1409.
22. Kim S-S, Sun Park M, Jeon O, Yong Choi C, Kim B-S. Poly(lactide-co-glycolide)/hydroxyapatite composite scaffolds for bone tissue engineering. *Biomaterials*. 2006; 27(8):1399–1409. doi:10.1016/j.biomaterials.2005.08.016.
23. Mann S. *Biomineralization : principles and concepts in bioinorganic materials chemistry*. New York: Oxford University Press; 2001.
24. Ando J. Tricalcium Phosphate and its Variation. *Bulletin of the Chemical Society of Japan*. 1958; 31(2):196–201.
25. Schroeder LW, Dickens B, Brown WE. Crystallographic studies of the role of Mg as a stabilizing impurity in  $\beta$ -Ca<sub>3</sub>(PO<sub>4</sub>)<sub>2</sub>. II. Refinement of Mg-containing  $\beta$ -Ca<sub>3</sub>(PO<sub>4</sub>)<sub>2</sub>. *Journal of Solid State Chemistry*. 1977; 22(3):253–262. doi:10.1016/0022-4596(77)90002-0.
26. Hughes JM, Cameron M, Crowley KD. Structural variations in natural F, OH, and Cl apatites. *American Mineralogist*. 1989; 74:870–876.
27. Lane JM, Tomin E, Bostrom MPG. Biosynthetic Bone Grafting. *Clinical Orthopaedics & Related Research* October 1999 [Internet]. 1999 [cited 2013 Feb 12]; Available from: <http://ovidsp.ovid.com/ovidweb.cgi?T=JS&CSC=Y&NEWS=N&PAGE=fulltext&D=ovftd&AN=00003086-199910001-00011>.
28. Zimmermann G, Moghaddam A. Allograft bone matrix versus synthetic bone graft substitutes. *Injury*. 2011; 42, Supplement 2:S16–S21. doi:10.1016/j.injury.2011.06.199.
29. Bauer TW, Muschler GF. Bone graft materials - An overview of the basic science. *Clin. Orthop. Rel. Res*. 2000; (371):10–27.

30. Thompson NS, Swain WD, Thompson NW, Davis R, Dilworth GR. Non-union in ankle and hindfoot arthrodeses using xenograft. *Foot and Ankle Surgery*. 2002; 8(4):239–244. doi:10.1046/j.1460-9584.2002.00331.x.
31. Nich C, Hamadouche M. 1.120 - Synthetic Bone Grafts: Clinical Use [Internet]. In: Paul Ducheyne, editor. *Comprehensive Biomaterials*. Oxford: Elsevier; 2011 [cited 2013 Feb 12]. p. 335–347. Available from: <http://www.sciencedirect.com/science/article/pii/B9780080552941002142>.
32. Mine Y, Zhang H. Chapter 5 - Egg Components in Food Systems [Internet]. In: *Biochemistry of Foods (Third Edition)*. San Diego: Academic Press; 2013 [cited 2013 Mar 5]. p. 215–241. Available from: <http://www.sciencedirect.com/science/article/pii/B9780080918099000054>.
33. Tullett S. The porosity of avian eggshells. *Comparative Biochemistry and Physiology Part A: Physiology*. 1984; 78(1):5–13. doi:10.1016/0300-9629(84)90083-5.
34. Board RG, Scott VD. Porosity of the Avian Eggshell. *Amer. Zool*. 1980; 20(2):339–349. doi:10.1093/icb/20.2.339.
35. Santos VR. Propolis: Alternative Medicine for the Treatment of Oral Microbial Diseases [Internet]. In: Sakagami H, editor. *Alternative Medicine*. InTech; 2012 [cited 2013 Feb 10]. Available from: <http://www.intechopen.com/books/alternative-medicine/antifungal-activity-of-propolis-oral-clinical-studies-in-humans>.
36. Mine Y, Zhang JW. The allergenicity of ovomucoid and the effect of its elimination from hen's egg white. *Journal of the Science of Food and Agriculture*. 2001; 81(15):1540–1546. doi:10.1002/jsfa.974.
37. Leem K-H, Kim M-G, Kim H-M, Kim M, Lee Y-J, Kim HK. Effects of Egg Yolk Proteins on the Longitudinal Bone Growth of Adolescent Male Rats. *Bioscience, Biotechnology, and Biochemistry*. 2004; 68(11):2388–2390.
38. Viswanath B, Ravishankar N. Controlled synthesis of plate-shaped hydroxyapatite and implications for the morphology of the apatite phase in bone. *Biomaterials*. 2008; 29(36):4855–4863. doi:10.1016/j.biomaterials.2008.09.001.
39. Bouyer E, Gitzhofer F, Boulos MI. Morphological study of hydroxyapatite nanocrystal suspension. *Journal of Materials Science: Materials in Medicine*. 2000; 11(8):523–531. doi:10.1023/A:1008918110156.
40. Cengiz B, Gokce Y, Yildiz N, Aktas Z, Calimli A. Synthesis and characterization of hydroxyapatite nanoparticles. *Colloids and Surfaces A: Physicochemical and Engineering Aspects*. 2008; 322(1–3):29–33. doi:10.1016/j.colsurfa.2008.02.011.
41. Wang P, Li C, Gong H, Jiang X, Wang H, Li K. Effects of synthesis conditions on the morphology of hydroxyapatite nanoparticles produced by wet chemical process. *Powder Technology*. 2010; 203(2):315–321. doi:10.1016/j.powtec.2010.05.023.
42. Swain SK, Sarkar D. A comparative study: Hydroxyapatite spherical nanopowders and elongated nanorods. *Ceramics International*. 2011; 37(7):2927–2930. doi:10.1016/j.ceramint.2011.03.077.

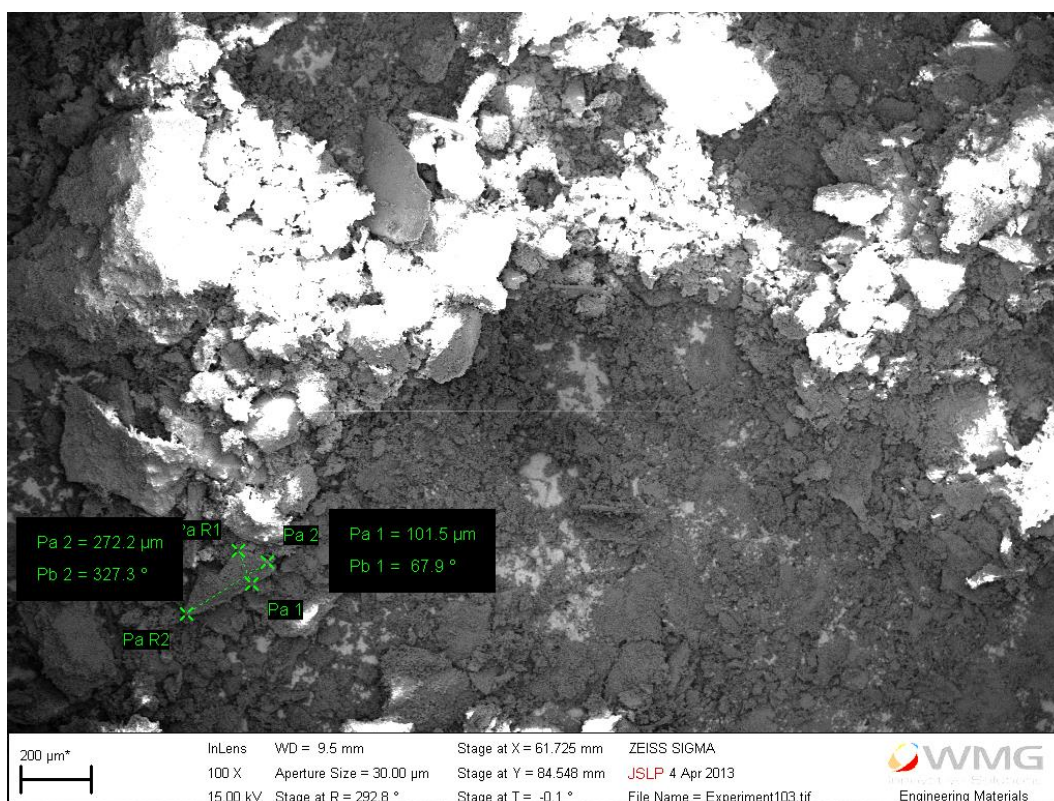
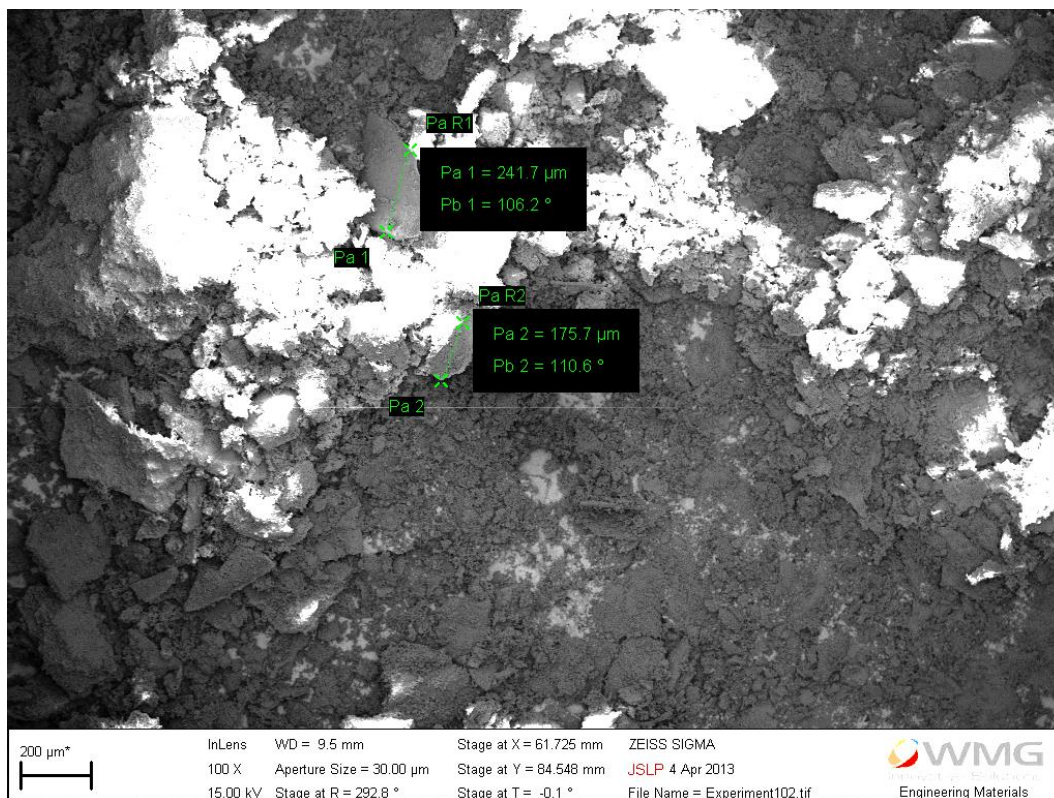
43. Landi E, Celotti G, Logroscino G, Tampieri A. Carbonated hydroxyapatite as bone substitute. *Journal of the European Ceramic Society*. 2003; 23(15):2931–2937. doi:10.1016/S0955-2219(03)00304-2.
44. Zhang H, Darvell BW. Synthesis and characterization of hydroxyapatite whiskers by hydrothermal homogeneous precipitation using acetamide. *Acta Biomaterialia*. 2010; 6(8):3216–3222. doi:10.1016/j.actbio.2010.02.011.
45. Zhang X, Vecchio KS. Hydrothermal synthesis of hydroxyapatite rods. *Journal of Crystal Growth*. 2007; 308(1):133–140. doi:10.1016/j.jcrysgro.2007.07.059.
46. Zhang C, Yang J, Quan Z, Yang P, Li C, Hou Z, et al. Hydroxyapatite Nano- and Microcrystals with Multiform Morphologies: Controllable Synthesis and Luminescence Properties. *Crystal Growth & Design*. 2009; 9(6):2725–2733. doi:10.1021/cg801353n.
47. Han J-K, Song H-Y, Saito F, Lee B-T. Synthesis of high purity nano-sized hydroxyapatite powder by microwave-hydrothermal method. *Materials Chemistry and Physics*. 2006; 99(2–3):235–239. doi:10.1016/j.matchemphys.2005.10.017.
48. Liu J, Li K, Wang H, Zhu M, Yan H. Rapid formation of hydroxyapatite nanostructures by microwave irradiation. *Chemical Physics Letters*. 2004; 396(4–6):429–432. doi:10.1016/j.cplett.2004.08.094.
49. Kumar GS, Thamizhavel A, Girija EK. Microwave conversion of eggshells into flower-like hydroxyapatite nanostructure for biomedical applications. *Materials Letters*. 2012; 76:198–200. doi:10.1016/j.matlet.2012.02.106.
50. Sarig S, Kahana F. Rapid formation of nanocrystalline apatite. *Journal of Crystal Growth*. 2002; 237–239, Part 1:55–59. doi:10.1016/S0022-0248(01)01850-4.
51. Poinern GE, Brundavanam RK, Mondinos N, Jiang Z-T. Synthesis and characterisation of nanohydroxyapatite using an ultrasound assisted method. *Ultrasonics Sonochemistry*. 2009; 16(4):469–474. doi:10.1016/j.ultsonch.2009.01.007.
52. Brundavanam RK, Jiang Z-T, Chapman P, Le X-T, Mondinos N, Fawcett D, et al. Effect of dilute gelatine on the ultrasonic thermally assisted synthesis of nano hydroxyapatite. *Ultrasonics Sonochemistry*. 2011; 18(3):697–703. doi:10.1016/j.ultsonch.2010.11.007.
53. Zou Z, Lin K, Chen L, Chang J. Ultrafast synthesis and characterization of carbonated hydroxyapatite nanopowders via sonochemistry-assisted microwave process. *Ultrasonics Sonochemistry*. 2012; 19(6):1174–1179. doi:10.1016/j.ultsonch.2012.04.002.
54. Haddow DB, James PF, Noort RV. Characterization of sol-gel surfaces for biomedical applications. *J Mater Sci: Mater Med*. 1996; 7(5):255–260. doi:10.1007/BF00058562.
55. Vijayalakshmi U, Rajeswari S. Preparation and Characterization of Microcrystalline Hydroxyapatite Using Sol Gel Method. *Trends in Biomaterials and Artificial Organs*. 2006; 19(2):57–62.
56. Fathi MH, Hanifi A. Evaluation and characterization of nanostructure hydroxyapatite powder prepared by simple sol-gel method. *Materials Letters*. 2007; 61(18):3978–3983. doi:10.1016/j.matlet.2007.01.028.

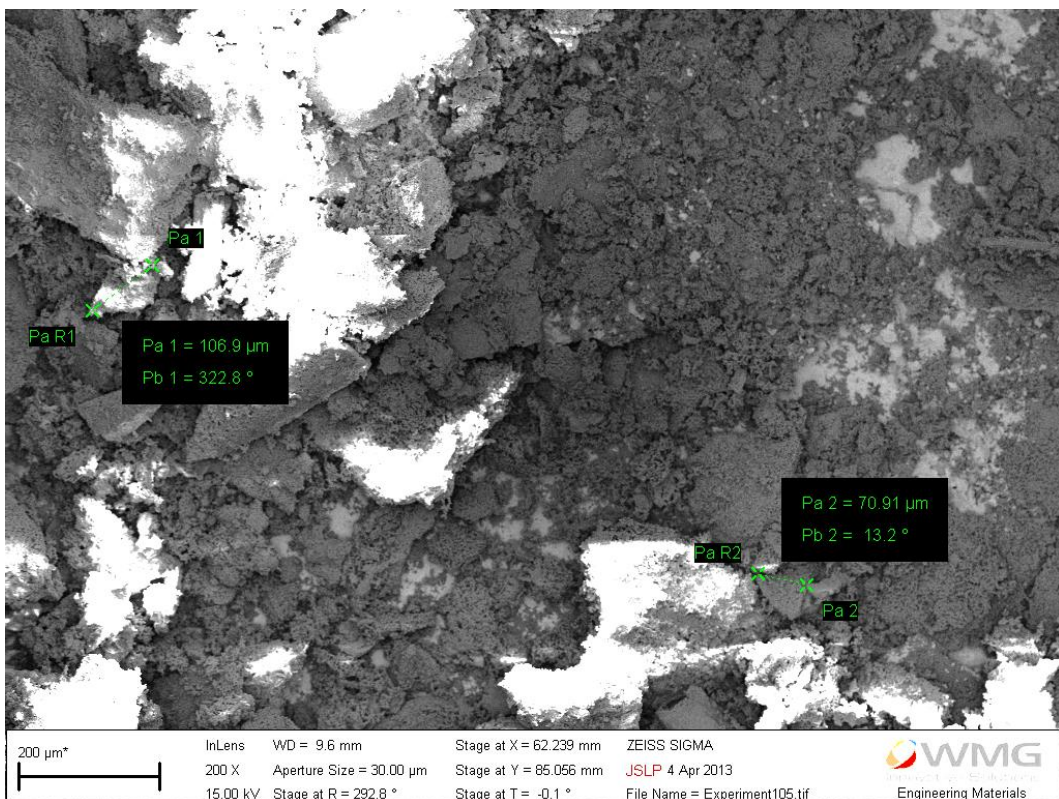
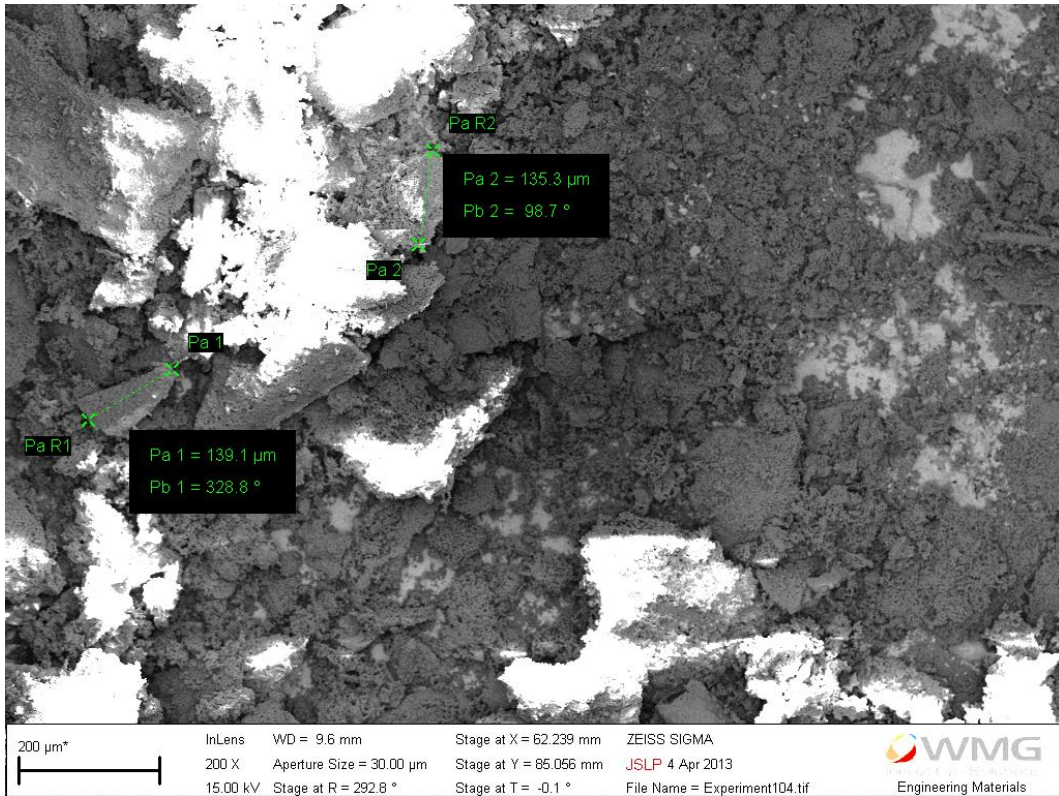
57. Bose S, Saha SK. Synthesis and Characterization of Hydroxyapatite Nanopowders by Emulsion Technique. *Chem. Mater.* 2003; 15(23):4464–4469. doi:10.1021/cm0303437.
58. Guo G, Sun Y, Wang Z, Guo H. Preparation of hydroxyapatite nanoparticles by reverse microemulsion. *Ceramics International.* 2005; 31(6):869–872. doi:10.1016/j.ceramint.2004.10.003.
59. Koumoulidis GC, Katsoulidis AP, Ladavos AK, Pomonis PJ, Trapalis CC, Sdoukos AT, et al. Preparation of hydroxyapatite via microemulsion route. *Journal of Colloid and Interface Science.* 2003; 259(2):254–260. doi:10.1016/S0021-9797(02)00233-3.
60. Ye F, Guo H, Zhang H, He X. Polymeric micelle-templated synthesis of hydroxyapatite hollow nanoparticles for a drug delivery system. *Acta Biomaterialia.* 2010; 6(6):2212–2218. doi:10.1016/j.actbio.2009.12.014.
61. Han Y, Li S, Wang X, Jia L, He J. Preparation of hydroxyapatite rod-like crystals by protein precursor method. *Materials Research Bulletin.* 2007; 42(6):1169–1177. doi:10.1016/j.materresbull.2006.09.003.
62. Neelakandeswari N, Sangami G, Dharmaraj N. Preparation and Characterization of Nanostructured Hydroxyapatite Using a Biomaterial. *Synthesis and Reactivity in Inorganic, Metal-Organic, and Nano-Metal Chemistry.* 2011; 41(5):513–516. doi:10.1080/15533174.2011.568434.
63. Santos MH, Oliveira M, Souza LPF, Mansur HS, Vasconcelos WL. Synthesis control and characterization of hydroxyapatite prepared by wet precipitation process. *Materials Research.* 2004; 7(4):625–630.
64. Nayak AK. Hydroxyapatite synthesis methodologies: An overview. *Int. J. ChemTechRes.* 2010; 2:903–907.
65. Bang JH, Suslick KS. Applications of Ultrasound to the Synthesis of Nanostructured Materials. *Advanced Materials.* 2010; 22(10):1039–1059. doi:10.1002/adma.200904093.
66. Suslick KS. Sonochemistry. *Science.* 1990; 247(4949):1439–1445. doi:10.1126/science.247.4949.1439.
67. Virone C, Kramer HJM, van Rosmalen GM, Stoop AH, Bakker TW. Primary nucleation induced by ultrasonic cavitation. *Journal of Crystal Growth.* 2006; 294(1):9–15. doi:10.1016/j.jcrysgr.2006.05.025.
68. Takiguchi M, Igarashi K, Azuma M, Ooshima H. Flowerlike agglomerates of calcium carbonate crystals formed on an eggshell membrane. *Crystal growth & design.* 2006; 6(12):2754–2757.
69. Dong Q, Su H, Xu J, Zhang D, Wang R. Synthesis of biomorphic ZnO interwoven microfibers using eggshell membrane as the biotemplate. *Materials Letters.* 2007; 61(13):2714–2717. doi:10.1016/j.matlet.2006.06.091.
70. Su H, Han J, Wang N, Dong Q, Zhang D, Zhang C. In situ synthesis of lead sulfide nanoclusters on eggshell membrane fibers by an ambient bio-inspired technique. *Smart Materials and Structures.* 2008; 17(1):015045.

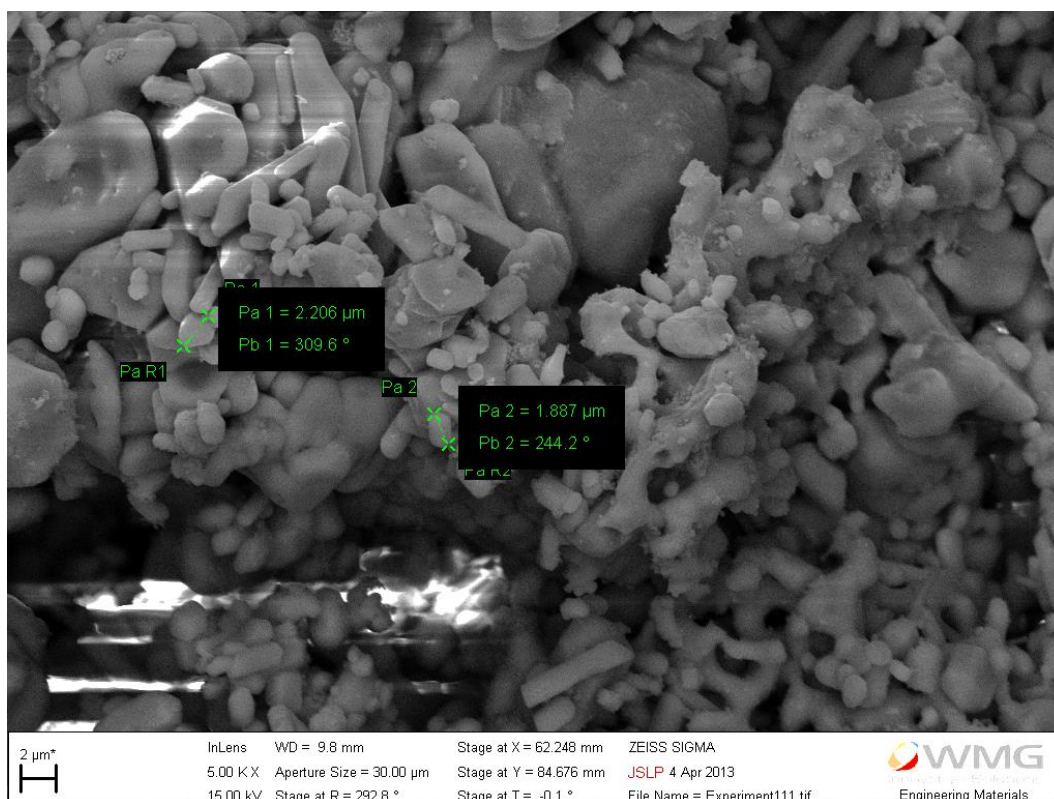
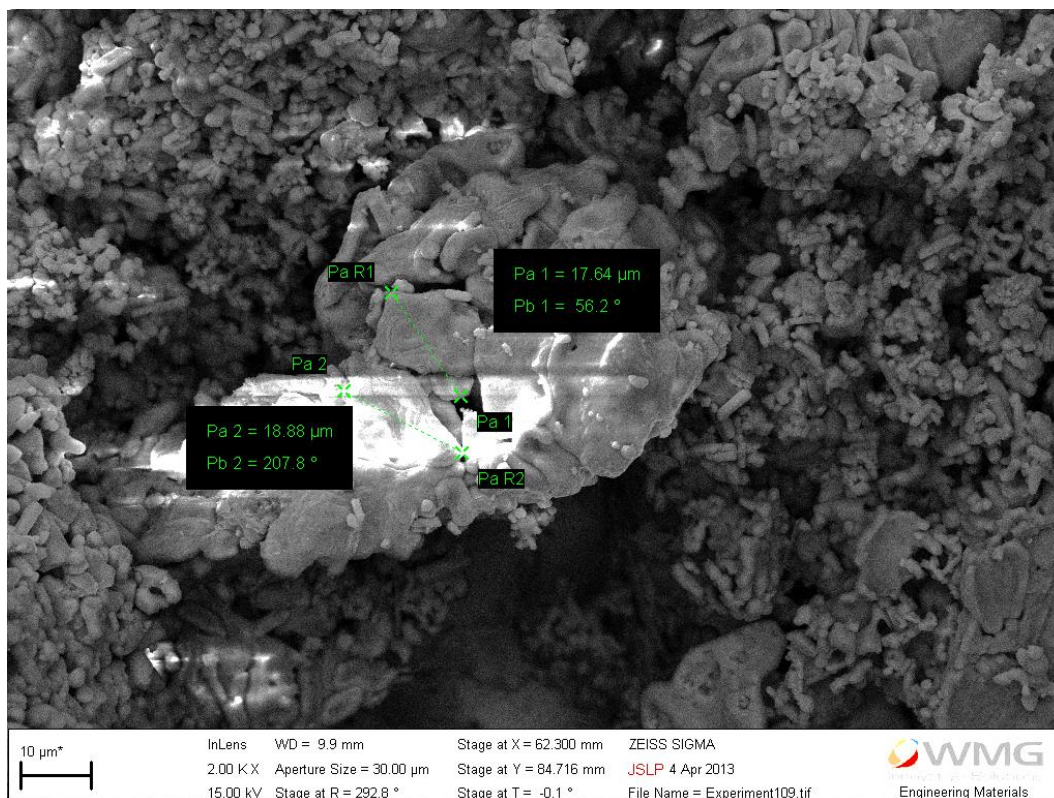
71. Nouroozi F, Farzaneh F. Synthesis and characterization of brush-like ZnO nanorods using albumen as biotemplate. *Journal of the Brazilian Chemical Society*. 2011; 22(3):484–488. doi:10.1590/S0103-50532011000300011.
72. Kaufmann R, Müller P, Hildenbrand G, Hausmann M, Cremer C. Analysis of Her2/neu membrane protein clusters in different types of breast cancer cells using localization microscopy. *Journal of Microscopy*. 2011; 242(1):46–54. doi:10.1111/j.1365-2818.2010.03436.x.
73. Flewitt PEJ. *Physical Methods for Materials Characterisation*. 2nd ed. Bristol ; Philadelphia: Institute of Physics Pub; 2003.
74. Watt IM. *The principles and practice of electron microscopy*. 2nd ed. Cambridge: Cambridge University Press; 1997.
75. Jacobs JA. *Engineering Materials Technology: Structures, Processing, Properties & Selection*. 4th ed. New Jersey: Prentice-Hall; 2001.
76. Callister WD. *Materials Science and Engineering*. 8th ed. Hoboken, N.J.: Wiley; 2011.
77. Eberhart JP. *Structural and Chemical Analysis of Materials: X-Ray, Electron and Neutron Diffraction X-Ray, Electron and Ion Spectrometry Electron Microscopy*. Chichester: Wiley; 1991.
78. Goodhew PJ. *Electron Microscopy and Analysis*. 3rd ed. London: Taylor & Francis; 2001.
79. Shackelford JF. *Introduction to Materials Science for Engineers*. 7th ed. Upper Saddle River, NJ: Pearson Prentice Hall; 2009.
80. Brown ME. *Introduction to thermal analysis: techniques and applications*. London: Chapman and Hall; 1988.
81. Hatakeyama T. *Thermal analysis: fundamentals and applications to polymer science*. Chichester: Wiley; 1994.
82. Holzwarth U, Gibson N. The Scherrer equation versus the “Debye-Scherrer equation.” *Nat Nano*. 2011; 6(9):534–534. doi:10.1038/nnano.2011.145.
83. McGehee R, Renault J. The use of standard deviation of X-ray diffraction lines as a measure of broadening in the Scherrer equation: a curve fitting method. *Journal of Applied Crystallography*. 1972; 5(5):365–370. doi:10.1107/S002188987200977X.
84. Cross AD. *An introduction to practical infra-red spectroscopy*. 3rd ed. London: Butterworths; 1969.
85. Crooks JE. *The spectrum in chemistry*. London (etc.): Academic Press; 1978.
86. Griffiths PR. *Chemical infrared Fourier transform spectroscopy*. New York ; London (etc.): Wiley-Interscience; 1975.
87. Tao J, Pan H, Zhai H, Wang J, Li L, Wu J, et al. Controls of Tricalcium Phosphate Single-Crystal Formation from Its Amorphous Precursor by Interfacial Energy. *Crystal Growth & Design*. 2009; 9(7):3154–3160. doi:10.1021/cg801130w.

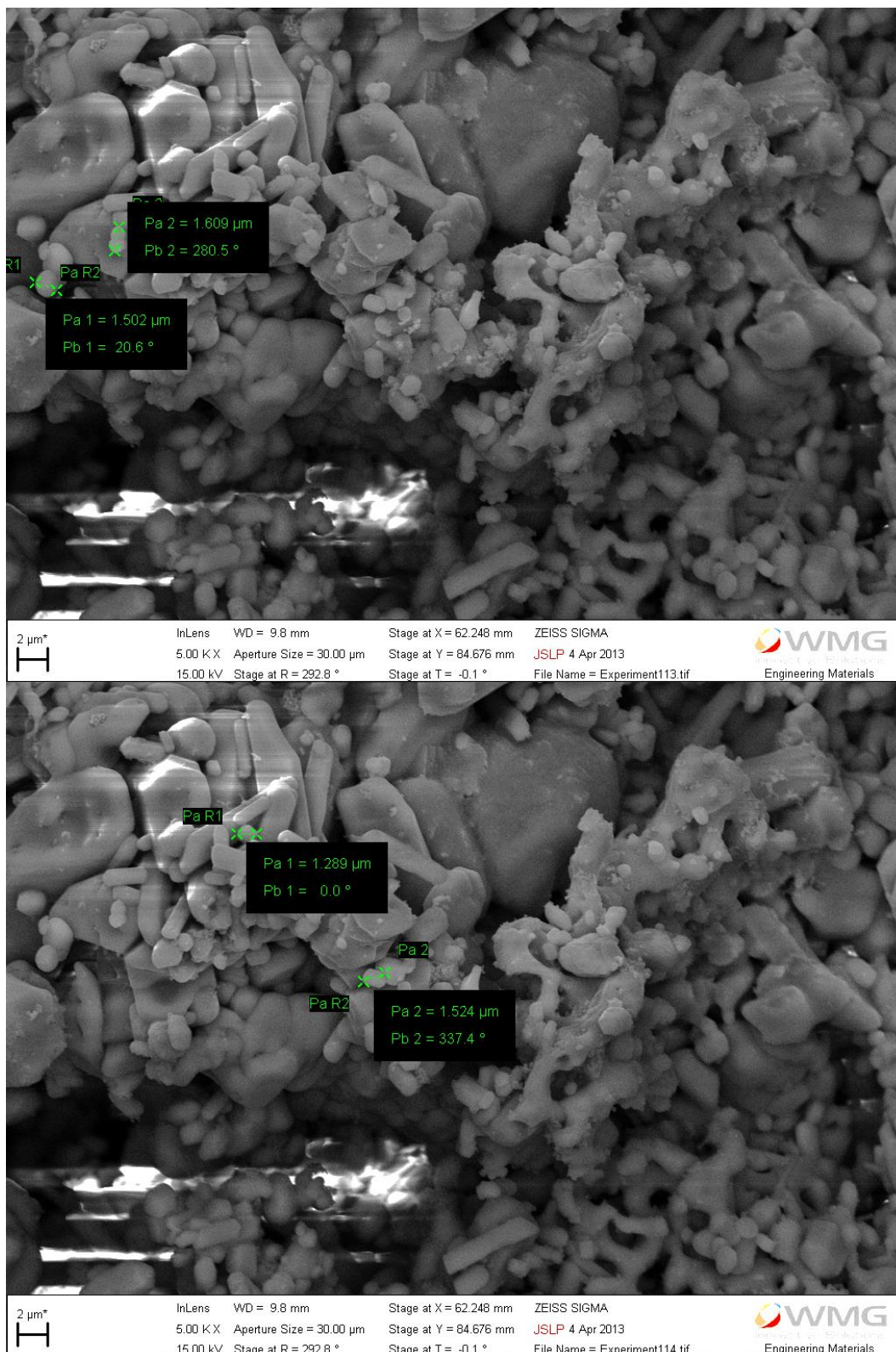
# Appendices

## Appendix 1: Dimensioned SEM of ALB1

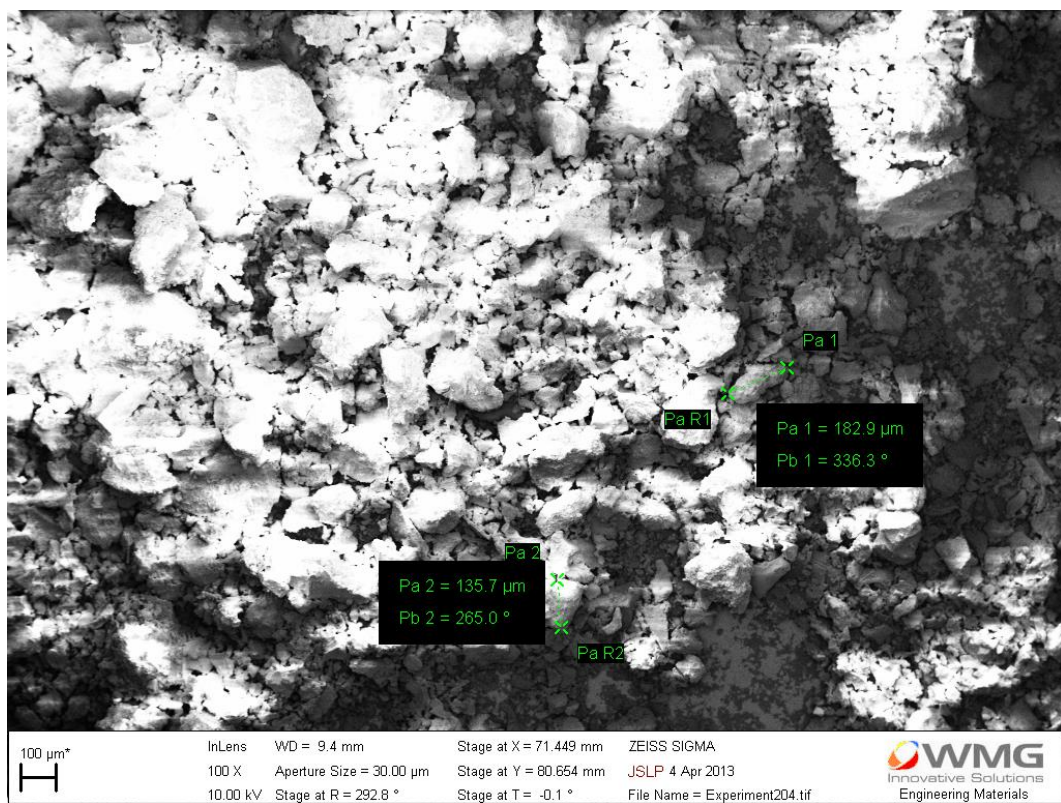
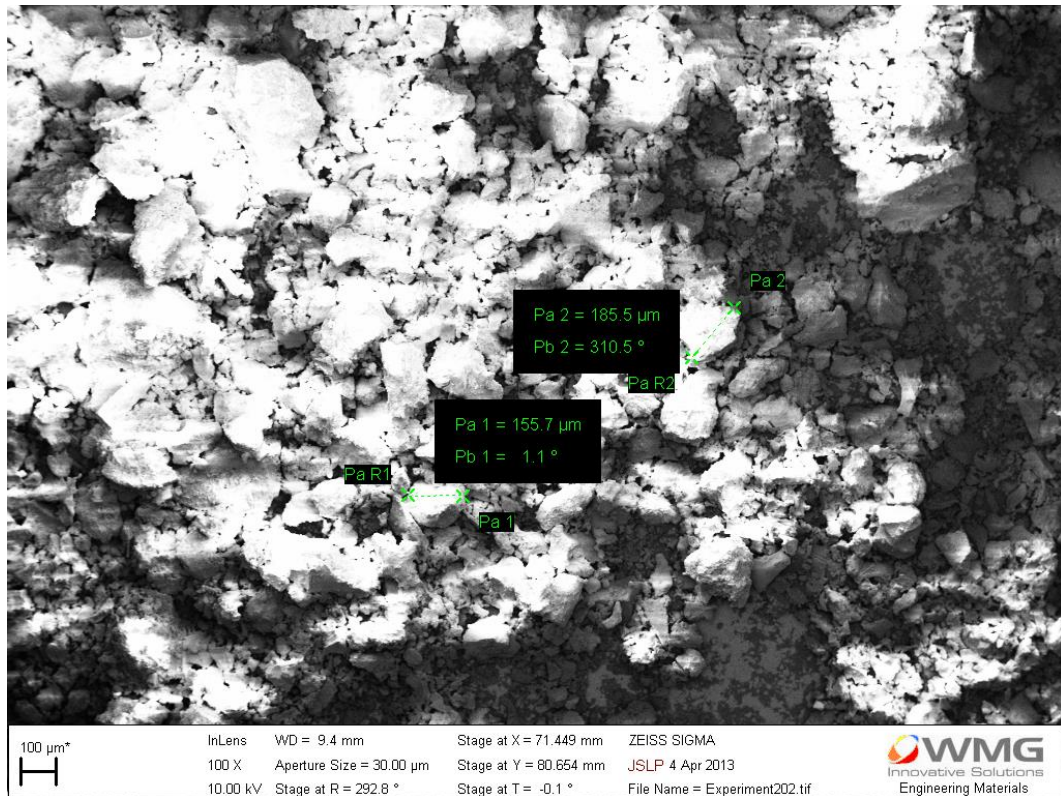


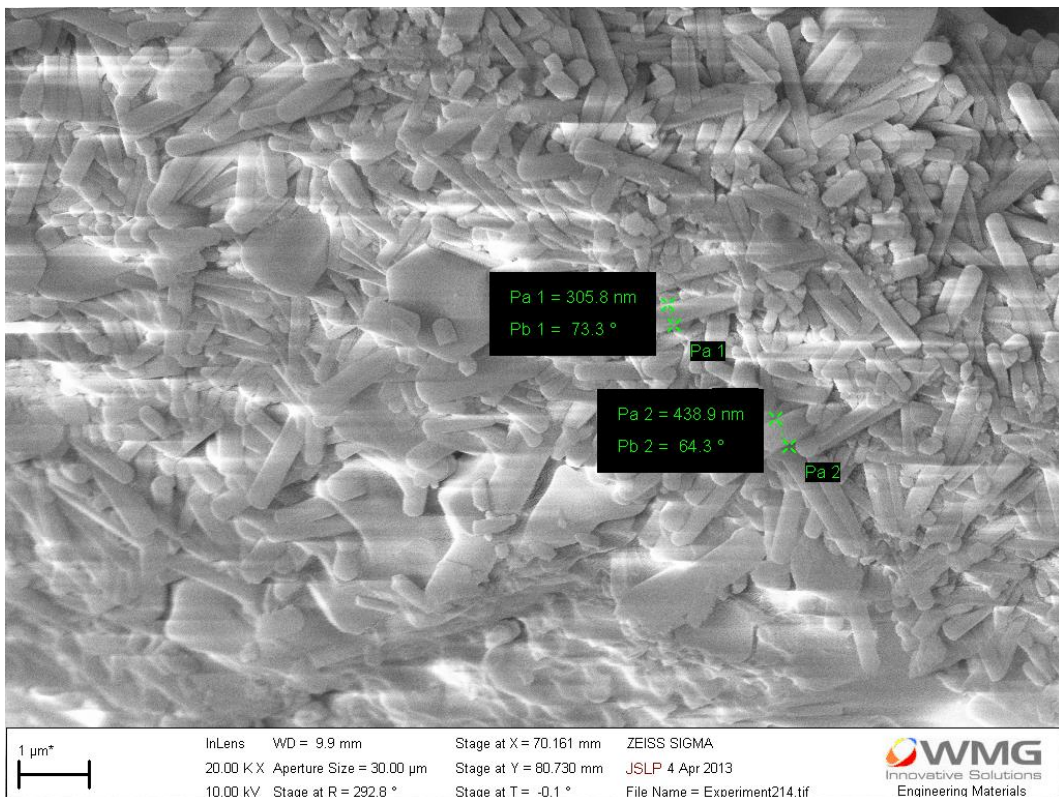
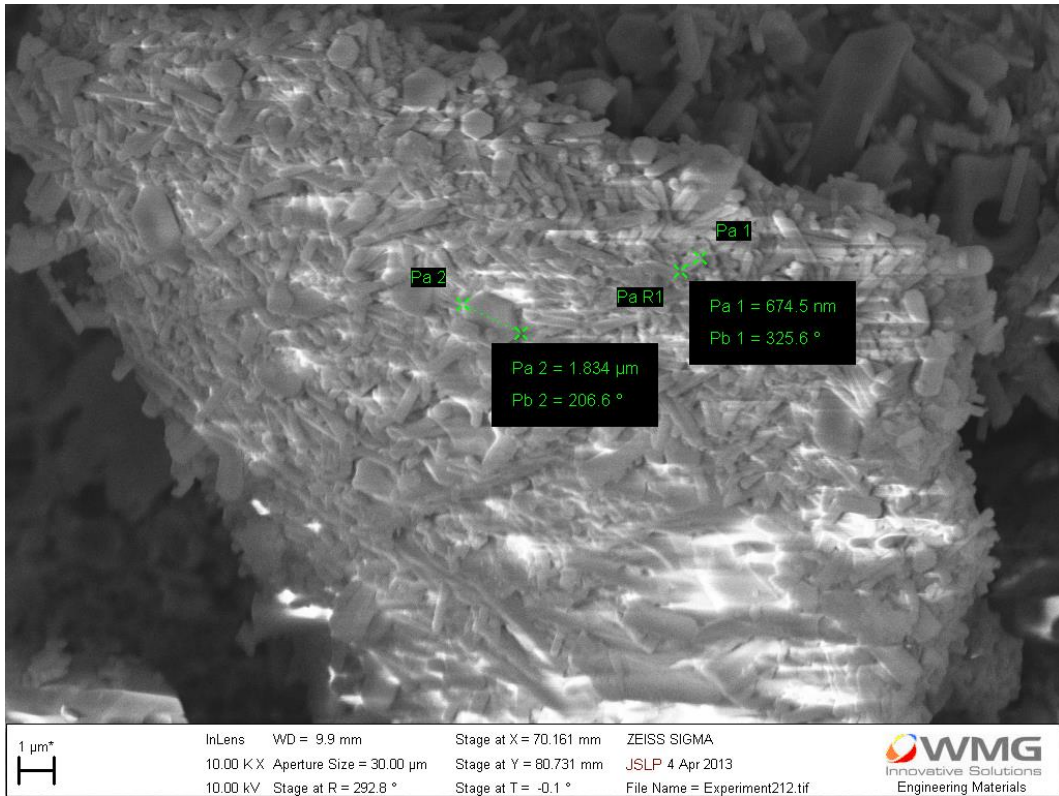


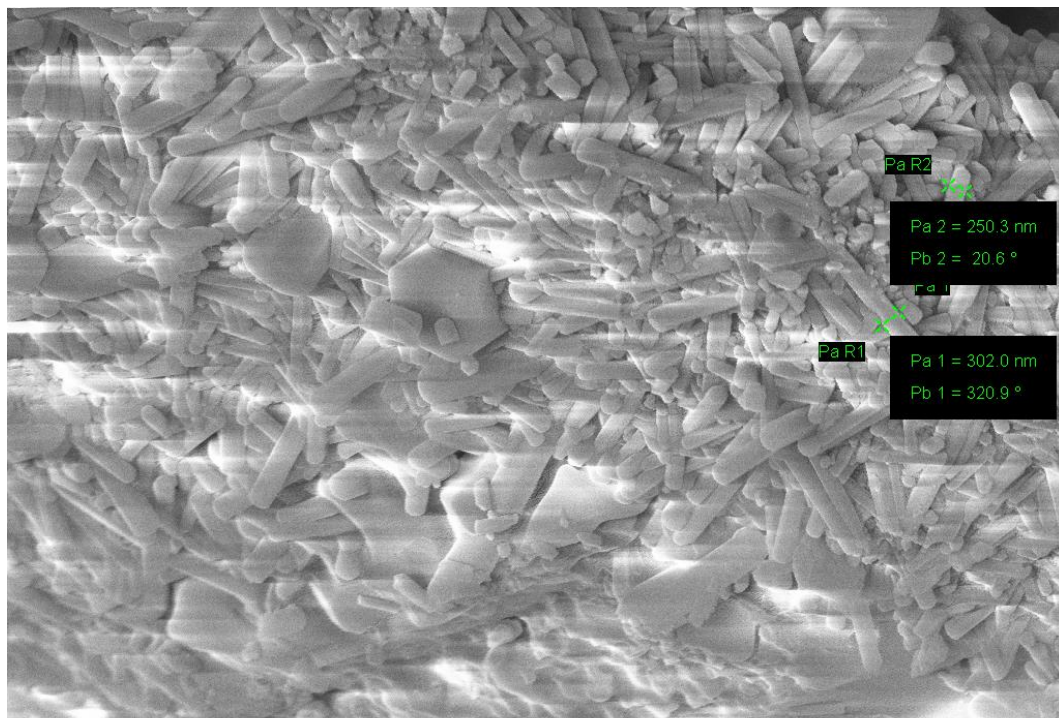




## Appendix 2: Dimensioned SEM of ALB2



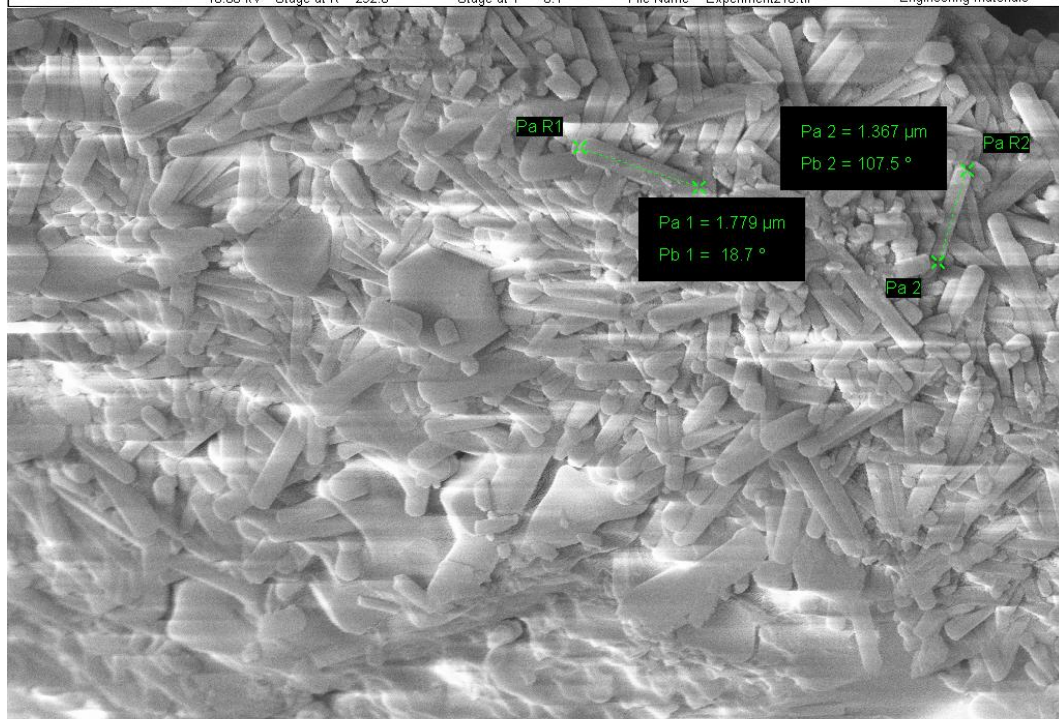




1  $\mu\text{m}^*$

InLens WD = 9.9 mm Stage at X = 70.161 mm ZEISS SIGMA  
 20.00 KX Aperture Size = 30.00  $\mu\text{m}$  Stage at Y = 80.730 mm JSLP 4 Apr 2013  
 10.00 kV Stage at R = 292.8 ° Stage at T = -0.1 ° File Name = Experiment216.tif

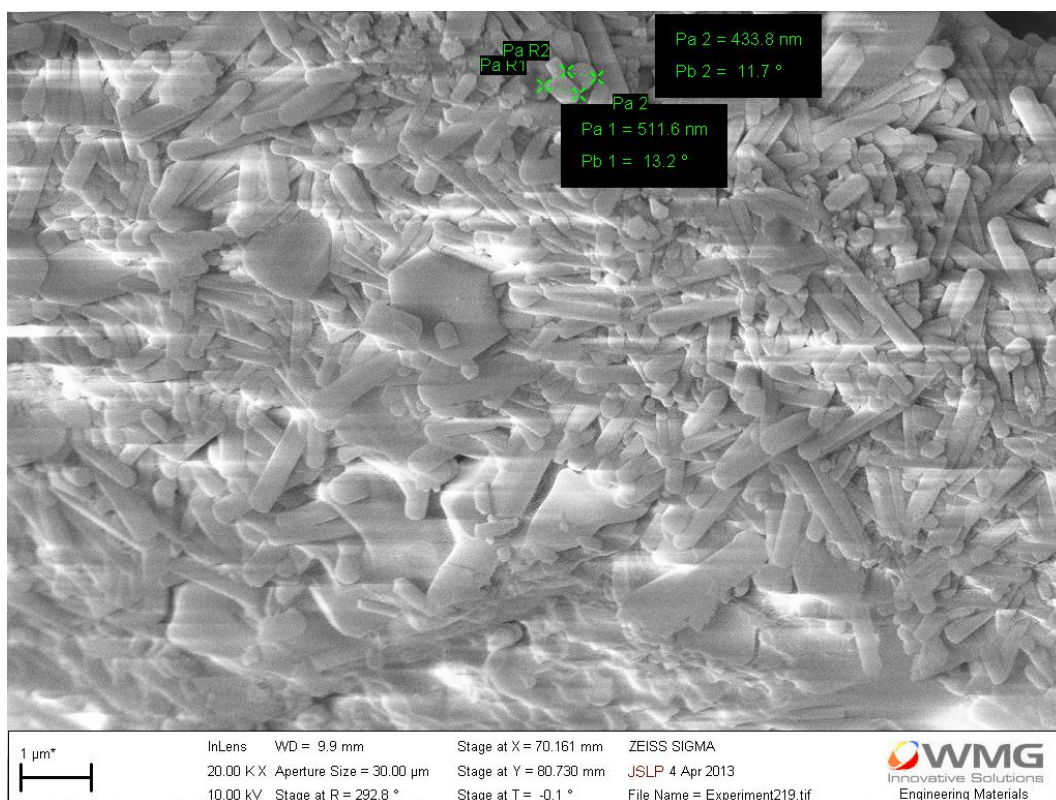
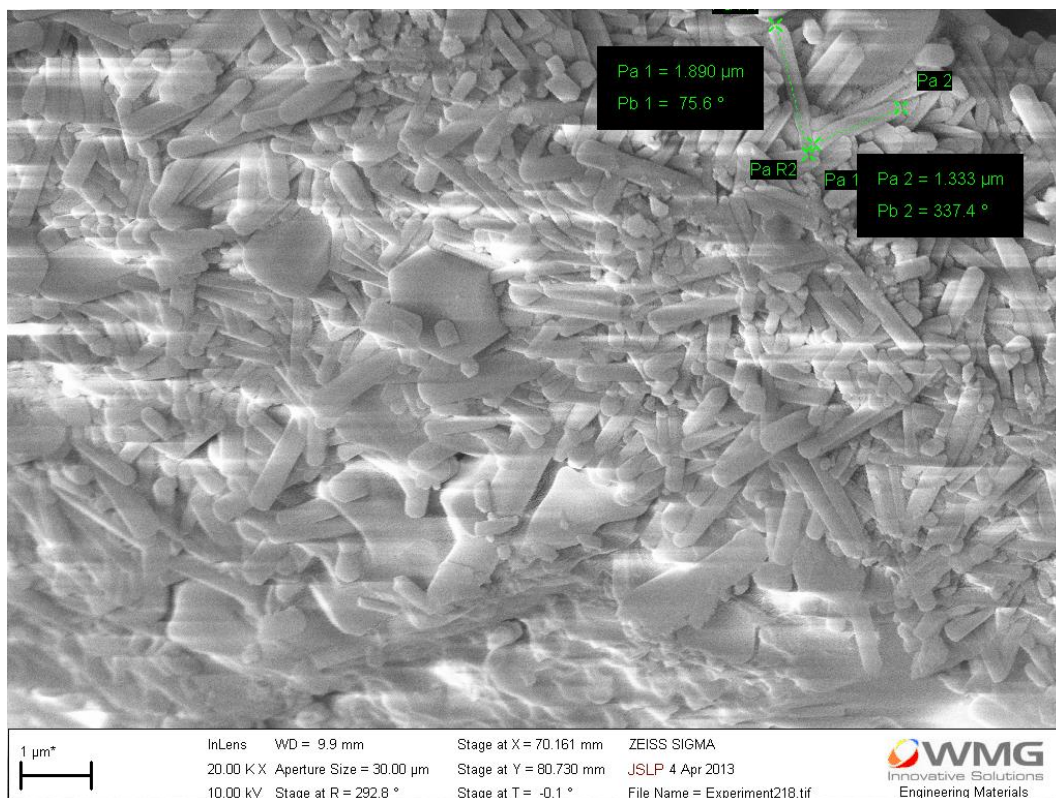
**WMM**  
 Innovative Solutions  
 Engineering Materials



1  $\mu\text{m}^*$

InLens WD = 9.9 mm Stage at X = 70.161 mm ZEISS SIGMA  
 20.00 KX Aperture Size = 30.00  $\mu\text{m}$  Stage at Y = 80.730 mm JSLP 4 Apr 2013  
 10.00 kV Stage at R = 292.8 ° Stage at T = -0.1 ° File Name = Experiment217.tif

**WMM**  
 Innovative Solutions  
 Engineering Materials



## Appendix 3: Dimensioned SEM of ALB3

